APPLIED COMPUTER SCIENCE

The Journal is a peer-reviewed, international, multidisciplinary journal covering a broad spectrum of topics of computer application in production engineering, technology, management and economy.

The main purpose of Applied Computer Science is to publish the results of cutting-edge research advancing the concepts, theories and implementation of novel solutions in computer technology. Papers presenting original research results related to applications of computer technology in production engineering, management, economy and technology are welcomed.

We welcome original papers written in English. The Journal also publishes technical briefs, discussions of previously published papers, book reviews, and editorials. Especially we welcome papers which deals with the problem of computer applications in such areas as:

- manufacturing,
- engineering,
- technology,
- designing,
- organization,
- management,
- economics,
- innovations,
- competitiveness,
- quality and costs.

The Journal is published quarterly and is indexed in: BazTech, Cabell's Directory, Central & Eastern European Academic Source (CEEAS), CNKI Scholar (China National Knowledge Infrastucture), DOAJ (Directory of Open Access Journals), EBSCO, ERIH PLUS, Index Copernicus, J-Gate, Google Scholar, Scope Database, Scopus, TEMA Technik und Management.

Letters to the Editor-in-Chief or Editorial Secretary are highly encouraged.

CONTENTS

APPLIED COMPUTER SCIENCE

Applied Computer Science, vol. 18, no. 3, pp. 5–18
doi: 10.35784/acs-2022-17

Submitted: 2022-07-28 | Revised: 2022-09-13 | Accepted: 2022-09-20

Keywords: FMS, Petri Nets, Performance evaluation

Grzegorz BOCEWICZ [0000-0002-5181-2872]*, *Robert WÓJCIK* [0000-0003-3860-7011]**, *Paweł SITEK* [0000-0001-6108-0241]***, *Zbigniew BANASZAK* [0000-0001-7219-3903]*

TOWARDS DIGITAL TWIN-DRIVEN PERFORMANCE EVALUATION METHODOLOGY OF FMS

Abstract

The paper presents a method of automated modelling and performance evaluation of concurrent production flows carried out in Flexible Manufacturing Systems. The method allows for quick assessment of various variants of such systems, considering their structure and the organization of production flow of possible ways of their implementation. Its essence is the conditions imposed on the designed model, limiting the space of possible variants of the production flow only to deadlock-free variants. The practical usefulness of the model implemented in the proposed method illustrates the example, which describes the simultaneous assessment of alternative variants of the flexible machining module's structure and the planned multi-assortment production. The ability of the method to focus on feasible solutions offers attractive perspectives for guiding the Digital Twin-like scenario in situations caused by the need to change the production flow.

1. INTRODUCTION

Designing Flexible Manufacturing Systems (FMSs) and planning technological processes generate complex multi-criteria optimization problems. These problems are related to decision-making in terms of resource allocation, process scheduling, and resolving resource conflicts of processes competing for access to shared resources.

Decision Support Systems (DSSs), based on online modelling and simulation, play a crucial role in solving the problems under consideration (Vaisi, 2022; Bujari et al., 2021; Makris, Michalos & Chryssolouris, 2012; Sliwa & Patalas-Maliszewska, 2016). The methods used in DSSs design are usually problem-oriented, which limits the range of their possible applications (Bakar, Henry & Ali, 1991; Banaszak, 1992; Banaszak, Skolud & Zaremba, 2003; Viswandham & Narahari, 1992). In particular, this implies the need for modelling and evaluating FMSs functioning based on the digital twin (DT) approach employed in interactive FMSs prototyping (Vaisi, 2022; Makris, Michalos & Chryssolouris, 2012).

* Faculty of Electronics and Computer Science, Koszalin University of Technology, Poland, grzegorz.bocewicz@tu.koszalin.pl, zbigniew.banaszak@tu.koszalin.pl
** Faculty of Information and Communication Technology, Wrocław University of Science and Technology, Poland, robert.wojcik@pwr.edu.pl
*** Department of Information Systems, Kielce University of Technology, Kielce, Poland, sitek@tu.kielce.pl

Since the dominant role in FMSs is played by the interaction of various processes taking place in them, i.e., the flow of workpieces, jigs, and fixtures, tool exchange, and chip removal, data and energy flows, and others, the natural choice of representation to model their behavior is using the formalism of the Petri nets (Reisig, 1982; Reutenauer, 1988).

Models of this type allow both to assess alternative variants of the FMS structure (i.e., the configuration of autonomous production modules that create it) and to choose how to organize the flow of production carried out in it.

The rest of the article is organized as follows: Section 2 elaborates on related works. Section 3 presents the example of a Flexible Machining Module (FMM) and introduces the issues of planning multi-assortment production carried out in it. Section 4 describes the terminology and essential modelling principles of the Petri net representation used in the FMM reference model. Section 5 includes a diagram of the methodology for the construction of methods implementing the digital twin-driven decision support concept (DTDSC), in particular, the method of determining the configuration of the FMS structure and assessing alternative ways of organizing the flow of production carried out in it. Section 6 presents the concluding remarks.

2. CURRENT-STATE

In recent years, there has been a rapid increase in the use of FMS in the automotive, electrical, and electronic industries (Janardhanan et al., 2019). The increase in the variety of FMSs applications is accompanied by new solutions to their structures and ways of functioning.

The concept of FMS that merges the ideology of flow shop and batch shop manufacturing system is based on three major components, i.e., workstations, automated material handling with a storage system, and a central computer. The interaction of these components determines the scope of the flexibility of the FMS, which can be assessed by different tests such as part variety, schedule change, error recovery, and new part test (Jonsson, 2000; Manu et al., 2018; Rachamadugu & Stecke, 1994). To effectively exploit this potential for flexibility, different methods are used. Among the available methods such as analytical methods (using mathematical programming), heuristic methods (employing production sequencing rules), artificial intelligence (using evolutionary and (or) population algorithms), and computer simulation (especially discrete event simulation). The latter is most often used in practice, which is due, among other things, to the fact that mathematical computations are cumbersome (as well as very time-consuming) and evolutionary algorithms are not very precise. It is also worth noting that computer simulation methods make it possible to analyze the transient states associated with the start-up and termination of production processes.

In this context, a digital twin concept referring to a digital replica of physical processes and systems seems to be well suited to model various FMSs solutions regarding their configuration and the organization of production carried out in them. Notice that the digital twin combines a physical object (e.g., FMS) and its digital representation in virtual space (e.g., discrete event system model). Therefore, the FMS simulation model implemented with the aid of it can be used both to plan the processes implemented virtually in it and to correct previously planned and then physically implemented in FMS. Indeed, this approach to FMSs design and control is increasingly common and finds its applications in systems supporting preventive maintenance scheduling and proactive job-shop as well as dynamic scheduling in manufacturing (Coito et al., 2022; David, Lobov & Lanz, 2018; Hatono et al., 1989; Neto et al., 2021; Nielsen, Michna & Do, 2014; Nielsen, Sung & Nielsen, 2019; Patalas-Maliszewska & Kłos, 2019; Zhang, Bai & Yang, 2022; Stączek et al., 2021; Świć & Gola, 2013).

It should be emphasized that methods implementing simulation models following ***IF ... THEN*** rule paradigm do not guarantee acceptable solutions, e.g., scenarios of production processes execution that do not lead to starvation and (or) deadlocks. Therefore the simulation models implemented in digital twin solutions are burdened with a similar deficiency, implying the need to eliminate unnecessary analysis of unacceptable solutions, e.g., leading to deadlocks of modelled processes. This observation is the main inspiration for the research undertaken in this work showing the possibilities of building simulation models limiting the implemented scenarios of system behavior only to acceptable ones.

The multi-criteria nature of production-planning problems, the complexity of these problems, and the need to make decisions online spur the development of techniques and methods for building dedicated DSSs (Banaszak, 1992; Bujari et al., 2012; Jensen, 1987; Laemmle & Gust, 2019). Hence, the relevant computer-aided tools should be designed to allow an integrated online analysis of alternative scenarios for completing production orders and early detection of errors in the order execution method used (Alexopoulos et al., 2022). Similar expectations apply to solutions focused on computer-aided modelling, exploring feasible alternatives, and evaluating the functioning of operational control algorithms implemented in real-time industrial controllers (Heiner et al., 1992).

Due to the variety of production decision-making problems, the large number of decision variables characterizing them, and the multi-criteria nature of the problems solved, computer simulation methods are most often used to solve them. Many papers in the scope of modelling and simulation of production flow especially scheduling and routing, prefer the Petri nets framework usage (Recalde et al., 2022; Zhou & Zain, 2016). Some already proposed approaches, such as colored, inhibitor, fuzzy, timed, predicate-transition, and hierarchical Petri nets representation, have been used to model complex systems with outstanding results (Laemmle & Gust, 2019; Van der Aalst, 1992). Their main advantage is the easy implementation of procedures for flow control of the processes performed in the modeled systems. In other words, the essential advantage of Petri network representation comes down to the possibility of prototyping alternative material flow scenarios modeled as a procedure for the relevant control flows (Bocewicz et al., 2022; He et al., 2022).Control flow procedures usually boil down to the implementation of different priority dispatching rules such as Longest Processing Time, Shortest Processing Time, and First in, First Out, and Last in, First Out, and many others, including Earliest Due Date, Critical Ratio, Dynamic Least Slack Rules, and other (Silva et al., 2012; Zanchettin, 2021).

The main shortcoming of the simulation approach is the considerable amount of time needed to build an appropriate model. In this respect, an approach aimed at an automated generation of the simulation model using domain-oriented data of production systems seems to be the most promising. An example of such a type of approach is presented in this work.

3. EXAMPLE OF HYPOTHETICAL FMM SPECIFICATION

The FMS class under consideration includes systems in which:

– a set of pipeline processes $PP = \{PR_i \mid i = 1 \dots v\}$, such that: $PR_i = ((d_{i_k}, O_{i_k}) \mid k = 1 \dots \mathcal{K})$, where: d_{i_k} – the machine used to process the i_k-th product, O_{i_k}– the th operation of the i-th process carried out on the machine $d_{i_k} \in D$, where D – is the set of FMS resources (machines), $\mathcal{K}$ – means number of operations of the PR_i process,

– an inter-operational storage buffer B_i with a capacity of BP_i is assigned to each i-th machine ($d_i \in D$),

– to each operation O_i of the i-th process carried out on the d_i machine, the time of its execution t_i is assigned.

Moreover, it is assumed that each odd operation of the i-process is carried out by an appropriate device(s) moving the workpieces between the buffers of successive machines; each operation of the i-th process is carried out on a machine from the set D.

To illustrate the introduced specification of the processes carried out in the example FMS, let's consider FMM with the configuration as in Fig. 1.

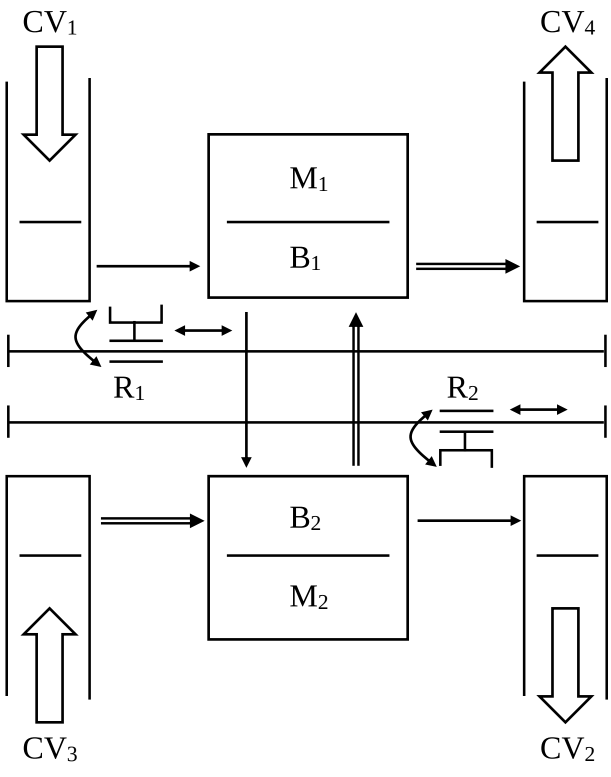

Fig. 1. Diagram of an example FMM

Process sequences specifying processes in the considered FMM are given in the following forms:

$$PR_1 = ((R_1, O_1), (M_1, O_2), (R_1, O_3), (M_2, O_4), (R_2, O_5)), \tag{1}$$
$$PR_2 = ((R_1, O_6), (M_2, O_7), (R_2, O_8), (M_1, O_9), (R_1, O_{10})),$$

(R_i, O_j) denotes the j-th operation of the robot R_i and (M_k, O_j) the j-th operation of the M_k machine.

Machines M_1, M_2 are associated with buffers B_1, B_2 assigned to them with appropriate capacities: $BP_1 = 1$, $BP_2 = 2$. Operation times are given in Table 1.

Tab. 1. Delivery times t_i for transport operations and processing of process specifications (1) calculated in contractual units of time (t.u.)

	O_1	O_2	O_3	O_4	O_5	O_6	O_7	O_8	O_9	O_{10}
t_i [t.u.]	5	20	5	10	5	10	25	5	10	5

According to the PR_1 specification, the items delivered by the CV_1 feeder are first processed on the M_1 machine, then on the M_2. Next, they are stored on the CV_2 feeder. According to the PR_2 specification, the items supplied by the CV_3 feeder are processed first on the M_2 machine, then on the M_1. Finally, the items are transported to the CV_4 feeder.

In other words, the example PR_1 specification refers to a process sequence in which the R_1 robot picks up an object from feeder CV_1 and transfers it to buffer B_1 (from where it is automatically transferred to the M_1 machine). After the workpiece is handed over, it is processed from the B_1 buffer to the M_1 machine. When the operation on machine M_1 is completed, the workpiece is deposited to B_1. The workpiece deposited in B_1 (after processing on M_1) is then picked up by the robot R_1 and deposited into buffer B_2 of M_2. After the workpiece is handed over, it is processed from the B_2 to the M_2 machine. When the operation is completed, the workpiece is deposited in B_2. The workpiece deposited in B_2 (after processing on M_2) is then picked up by R_2 and deposited on the CV_2 receiver.

It is worth noting that the presented method of specification of production processes can be treated as a task-oriented language of communication between the operator (planner, dispatcher) and the DSS he used. In particular, the given specification of the processes can lead to unacceptable variants of production flows. In the case under consideration, this situation occurs when the first process occupying buffer B_1 is waiting for buffer B_2 to be released while the second process occupying buffer B_2 is waiting for buffer B_1 to be released.

4. PETRI NETS MODELING FRAMEWORK

To make the paper self-contained, let's enter a set of basic concepts constituting the Petri nets framework (Reisig, 1982; Reutenauer, 1988) used in the following two sections. A Petri net is formally defined as a six-tuple $PN = (P, T, E, W, K, M_0)$, where:

- $P = \{p_1, \dots, p_n\}$ and $T = \{t_1, \dots, t_m\}$ are the finite non-empty sets of places and transitions, such that $P \cap T = \emptyset$;
- $E \subset (P \times T) \cup (T \times P)$ is a flow relation, such that the following condition holds $\mathrm{dom}(E) \cup \mathrm{cod}(E) = P \cup T$;
- $W: E \to N$ is a weight function; the weight of one is assigned to an arc as a default;
- $K: P \to N$ is a place capacity function;
- $M_0: P \to N_0$ is the initial marking, $\forall p \in P, M_0(p) \le K(p)$.

The Petri net structure is a bipartite graph that comprises a set of places drowned as boxes, a set of transitions drowned as bars, and a set of arcs E. Places usually represent some conditions or resources. When the place represents a resource, it is assumed that a token in it means the machine's readiness to operate. Places may contain tokens that are drowned as black dots. Transitions represent events. Transitions transfer tokens from one place to another. During this process, called firing *t* transition, the tokens removed from their input places are stored in their output places.

An example of a reference Petri net model determined by the specifications of the production routes of the form (1) is shown in Fig. 2. Places $p_1 - p_8$ model the current locations of the moving elements – for example, $p_1(p_2)$ corresponds to the location of the element waiting in buffer B_1 for machining in the M_1 machine. Places p_9 and p_{10} map buffer states B_1 and B_2, respectively. The $p_{11} - p_{14}$ sites correspond to the FMM resource states (robots and machines). In particular, the p_{13} and p_{14} sites model the machine standby, M_1 and M_2, respectively, and the p_{11} and p_{12} robot standby, R_1 and R_2, respectively.

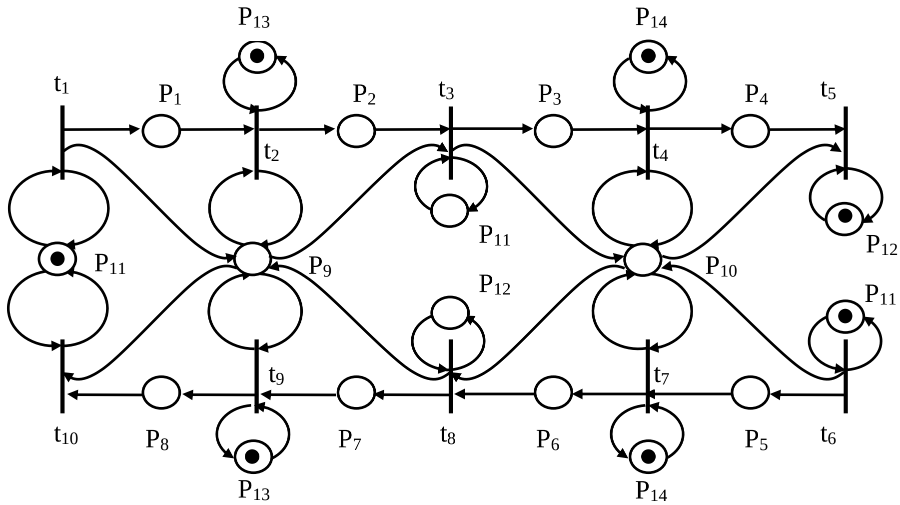

Fig. 2. Petri net-based reference model of FMM from Fig.1

Transitions t_1, t_3, t_6, and t_{10} correspond to the element movement operations carried out by the R_1 robot, while the t_5 and t_8 transitions are associated with the R_2 robot operations. The t_2 and t_9 transitions model the machining operations performed on the M_1 machine, and the t_4 and t_5 transitions correspond to the machining operations carried out on the M_2 machine.

The state of the Petri net usually called its marking, is defined by the number of tokens in each place and is denoted by vector $M = (M(p_1), \dots, M(p_i), \dots, M(p_n))$, where $n = ||P||$, is the cardinality of the set P. The number and position of tokens may change during the execution of a Petri net by firing transitions according to the following rules:

1. **Enabling Rule**: A transition t is said to be enabled when the following conditions hold:

– $M(p_n) \geq W(p,t)$, $\forall p \in \cdot\, t$,

– $M(p) \leq K(p) - W(p,t) + W(t,p)$, $\forall p \in \cdot\, t \cup (\cdot\, t \cap t\, \cdot)$, where $\cdot\, t = \{p | (p,t) \in E\}$,

– $t \cdot = \{p | (t,p) \in E\}$.

2. **Firing Rule**: An enabled transition t can fire, thus removing $W(p,t)$ tokens from each input place $p \in \cdot t$ and placing $W(t,p) - W(p,t)$ tokens in each output place $p \in t \cdot$.

The so-called reachability graph is used for the analysis of Petri net models. The graph's vertices (modelling states) represent a set $R(M_0)$ of states reachable in this network. For example, in Petri net from Fig. 3, the initial state is:

$$\begin{array}{ccccccccccccccccc} & & p_1 & p_2 & p_3 & p_4 & p_5 & p_6 & p_7 & p_8 & p_9 & p_{10} & p_{11} & p_{12} & p_{13} & p_{14} & \\ M_0 & =(& 0 & 0 & 0 & 0 & 0 & 0 & 0 & 0 & 0 & 0 & 1 & 1 & 1 & 1 &) \end{array}$$

because $(\forall i = 1 \ldots 10)$ $(M_0(R_i) = 0)$ and $((\forall i = 11 \ldots 14)$ $(M_0(R_i) = 1)$. In this state, two transitions t_1 and t_6 are simultaneously enabled. The firing of transitions is random, and transitions that do not have common places may fire but not simultaneously. This limitation results from the principle of non-simultaneity of events adopted in physics.

The nodes (or states) of a Petri net's reachability graph represent the net's reachable markings. The set of states reachable in the Petri net from its initial marking M_0 is denoted as $R(M_0)$. Figure 3 shows the reachability graph of Petri net from Fig. 2.

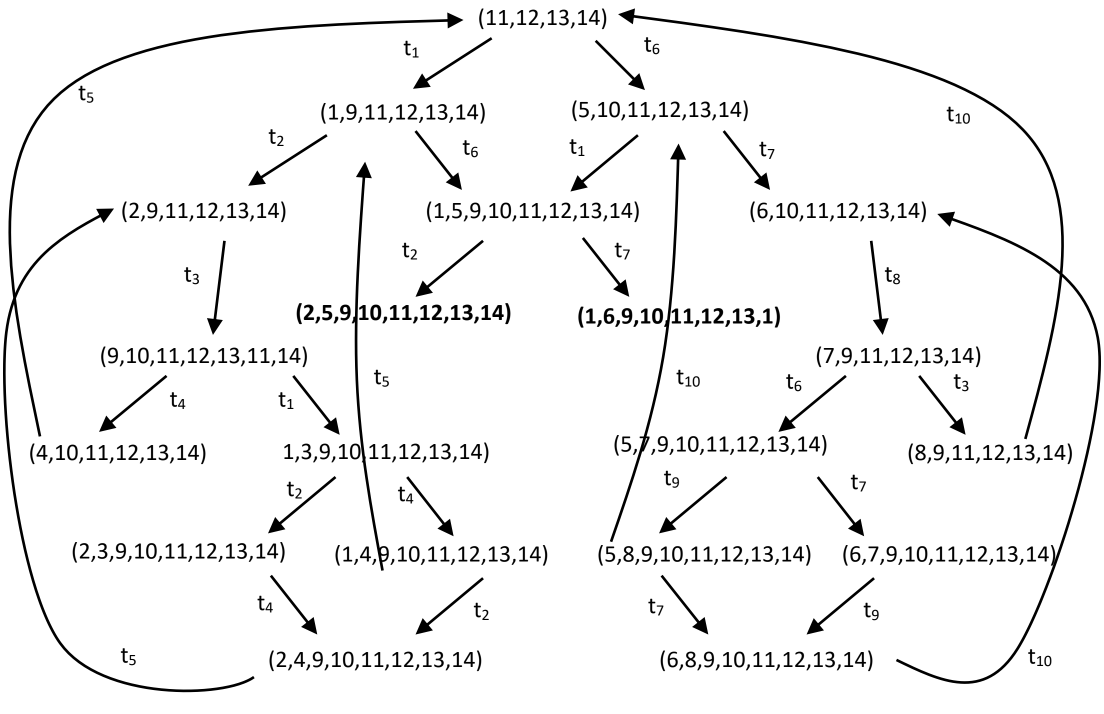

Fig. 3. The reachability graph of Petri net from Fig. 2. States in bold, i.e. (2,5,9,10,11,12,13,14) and (1,6,9,10,11,12,13,14) are states that illustrate deadlocks.

A simplified notation of states can increase the readability of the graph. In the adopted notation, we omit the positions taking the value "0" in the sequences specifying the states, and the corresponding coordinates are entered in place of the positions taking the value "1". In the adopted notation, the state $M_0 = (0,0,0,0,0,0,0,0,0,0,1,1,1,1)$ takes the form: $\boldsymbol{M_0} = (11,12,13,14)$.

Besides a reachability graph, the Petri net reachability analysis can be conducted through the state equation:

$$M' = M + e(i)C,$$

where:

- $e(i)$ – is a unit row-vector of size $1 \times m$, which is zero everywhere, except the i-th component corresponding to the transition t_i enabled at the marking M,
- $C = C^+ - C^-$ – is the Petri net incidence matrix defined as $n \times m$ matrix of c_{ij}'s, where $m = ||T||$ and $n = ||P||$, and

$$C^+ = (c_{ij})_{n\times m}, c_{ij} = \begin{cases} W(t_i, p_j) \text{ for } (t_i, p_j) \in E \\ 0 \text{ otherwise} \end{cases}$$

$$C^- = (c_{ij})_{n\times m}, c_{ij} = \begin{cases} W(p_j, t_i) \text{ for } (p_j, t_i) \in E \\ 0 \text{ otherwise} \end{cases}$$

The incidence matrix (i.e., an algebraic representation) provides a well-suited helpful form for the simulation of a net execution. In the case of the C matrix, it is easy to determine the same space of reachable states, as shown in Fig. 3.

C^+

	R_1	R_2	R_3	P_1	P_2
$O1_1$	1			1	
$O1_2$		1		1	
$O2_3$			1		1
$O3_1$	1				
$O3_3$			1		

$C = C^+ - C^-$

C^-

	R_1	R_2	R_3	P_1	P_2
$O1_1$	1				
$O1_2$		1			
$O2_3$			1	1	
$O3_1$	1				1
$O3_3$			1		1

The subject of the analysis of the created Petri net models is decision properties commonly addressed in the modelling of manufacturing systems, such as liveness, reachability, conservativeness, persistency, and boundedness. Their detailed description can be found in (Reisig, 1982; Reutenauer, 1988). The evaluation of prototype model variants carried out in this context aims to search for answers, among others, to questions such as: Whether the modelled system can reach a specific state as a result of required functional behavior? And: Whether a given transition t is live? To answer the first question formulated, we must find a transition firing sequence that would transform a marking M_0 to M_i, where M_i represents the specific state, and the firing sequence represents the required functional behavior. In this context, the paper is devoted to the problem of liveness-enforcing supervision in manufacturing systems where deadlocks arising from poor settlements of resource conflicts may arise.

Due to the problem NP-completeness of avoiding deadlocks in systems of concurrently executed processes competing in access to shared resources, the existing effective deadlock avoidance algorithms are based on sufficient conditions. These algorithms may lead to control strategies such that some of the allowable allocations of resources (which do not lead to a blockage of the processes using them) are omitted. In other words, using sufficient conditions to prevent the formation of blockages does not guarantee the maximum permissiveness of the considered class of processes. Therefore, in addition to differing in the number of accepted states of resource distribution, algorithms that implement different prevention conditions also differ in computational complexity. To sum up, taking into account additional information about the structure of concurrently executed processes allows one to use alternative methods of resolving resource conflicts dedicated to selected criteria for assessing the performance evaluation of the currently considered system. Among the most commonly relevant evaluation criteria are the following: degree of resource utilization, waiting time of processes for access to resources, flow time, inventory and manufacturing costs, makespan, unbalance, tardiness, and others.

The problem of deadlocks occurrence means that it becomes necessary adopting appropriate dispatching priority rules to prevent the deadlocks. In turn, the algorithms implementing such an approach are not maximally permissive, however, at the cost of low computational complexity (Yang & Hu, 2021). One such "deadlocks prevention" rule follows from the observation that the production flows follow the ordered lists of resources, indicating the sequences in which resources must be allocated to complete order execution. This assumption enables decomposing each production route into zones, where each zone is a sequence of sections consisting of shared resources followed by those consisting of unshared resources. Shared resources are used by more than one process, while other (unshared) resources are used by only one process.

The adoption of a rule prohibiting the simultaneous use of resources in individual sections of shared resources and a rule prohibiting the complete occupation of a zone of resources not shared by processes occurring in the subsequent busy section of repeating resources prevents the fulfillment of one of the four conditions necessary for the occurrence of a deadlock, i.e., the condition of a closed loop of resource requests. These rules guarantee that only resources in non-shared resource zones are used, i.e., states allowing all tasks to be completed. It is easy to see that leaving resources waiting for processes in such zones avoids deadlocks associated with situations in which all resources of all zones are used simultaneously (Banaszak, 1992; Claes & Tuyls, 2018; Reutenauer, 1988).

5. THE METHODOLOGY IMPLEMENTING THE DTDSC CONCEPT

Assuming that the execution times of individual machining operations and inter-station transport operations are known (as in Table 1) and remain unchanged for subsequent variants, it is possible to choose the solution that best meets the accepted expectations. In the experiments carried out, repeated for different priority selection rules, the same size of production batches was adopted. The experiments included planning serial (pipeline) production of two products carried out following two priority selection rules: Longest Processing Time (LPT) and Shortest Processing Time (SPT). The LPT (SPT) rule organizes tasks in the order of reducing (increasing) processing time. This approach means that each time a machine is released, the next task started on it is the longest (shortest) of the others ready. The LPT rule is most commonly used to determine the minimum cycle of a production process, and the SPT rule is used to determine the weighted time of production completion.

An illustration of the variants of the production flow corresponding to the above rules is presented in Fig. 4. The implementation of the LPT rule, compared to the SPT rule, allowed to shorten the production tact by 5 t.u. and consequently shorten the production cycle time by 20 t.u. It is also easy to see that using the LPT rule reduces the buffer capacity B_2 to $PB_2 = 1$.

Examples of computer-aided systems solutions enabling a comprehensive approach to modeling and assessing the effectiveness of FMS functioning, including flexible assembly systems, are presented in the papers (Viswandham & Narahari, 1992). The systems discussed there can support the user in the following tasks:

– design of FMS configuration (layout arrangement, selection, and placement of workstations, conveyors, buffers, and others),
– planning of production carried out in FMS (in terms of both tact and production cycle, as well as efficiency, effectiveness, and productivity).

Of course, the abovementioned issues do not exhaust all possible applications of similar tools based on Petri net models.

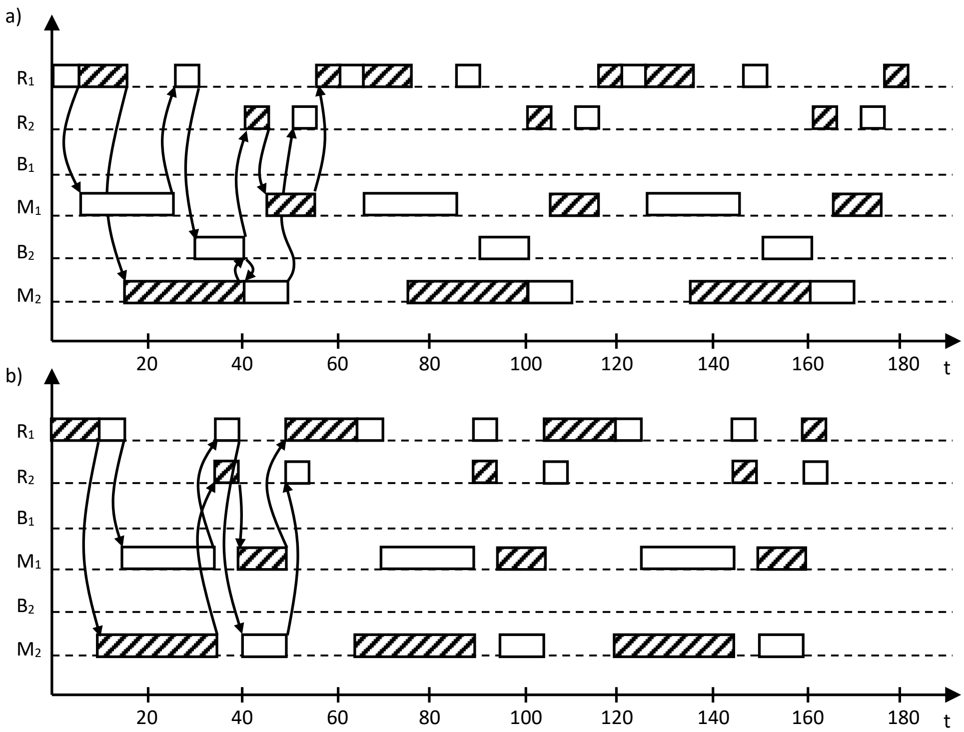

, ( ) – operations of the process set by PR1 (PR2)

Fig. 4. Gantt diagrams of the given production flow in the accepted production route specification (1) carried out according to the rule of the shortest processing time (a) and according to the rule of the longest processing time b).

In the presented context, we notice that any attempt at a more comprehensive approach to FMS modeling, allowing for simultaneous analysis of different variants of the arrangement of its elements and acceptable scenarios of the flow of production processes implemented in them, leads to complex, non-linear problems of multi-criteria optimization. The proposed approach overcomes this limitation. Focusing on the resources of the system and the processes implemented with their help makes it possible to consider their various options but is limited only to feasible solutions. The guarantee that only admissible variants of the production flow can be evaluated shortens searching for a solution that meets the set expectations. A diagram of the iterative process of alternating data specification and evaluation of their results-oriented toward the search for a variant that meets the required evaluation criteria is presented in Fig. 5.

The idea of the methodology presented in Fig.5, implementing the DTDSC concept, boils down to iteratively run stages: planning the FMS configuration and planning the production carried out in it, as well as the correction of the production plan implemented. In short, it can be reduced to stages: automatic determination of the Petri net model of the considered class of processes set in the adopted notation, modification of the model, which boils down to the implementation of the mechanism of synchronization of modeled processes (guaranteeing their deadlock-free execution), implementation of an arbitrarily chosen method of resolving resource conflicts and assessment of the quality indicators implied by it. Consequently, the presented methodology provides a robust framework for simultaneous optimization of the production facility layout and the production flow scenarios.

At the first of these stages (elements highlighted in Fig. 5 with a solid line), the layout design of the system (in particular, the material handling system) and the order execution plan (in particular: the input sequencing the order in which parts of various types are released into the system, tact and cycle time, makespan, and production flow schedule) are determined.

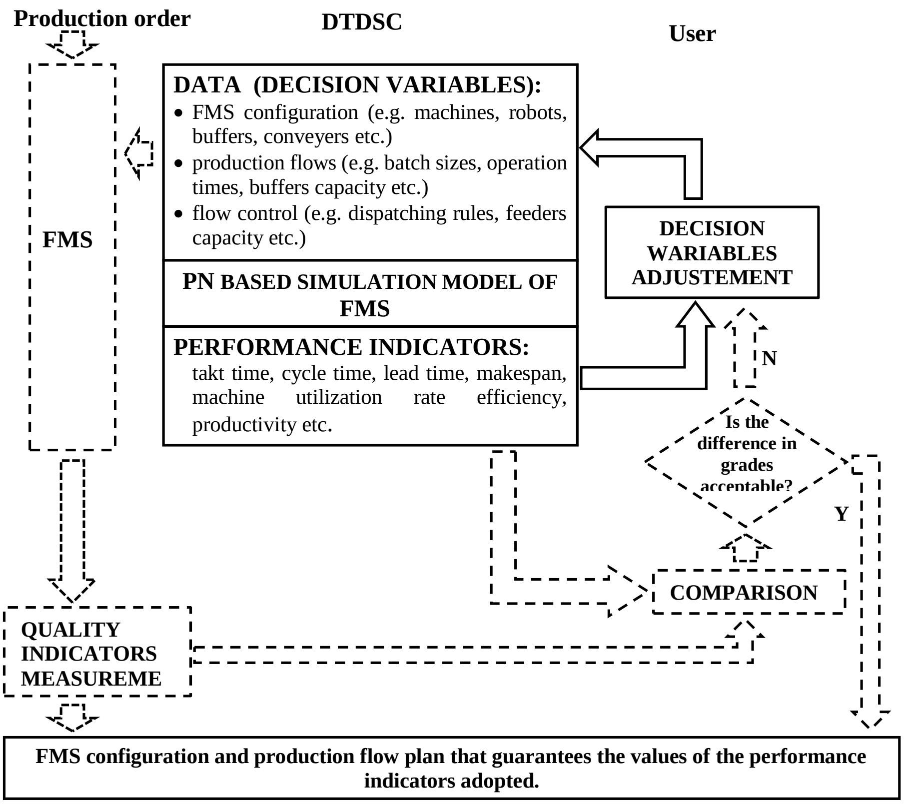

Fig. 5. Conceptual framework of the iterative searching process aimed at solution following the assumed criteria

At the next stage (including elements highlighted by a dashed line), based on the assessment of the adopted quality indicators of the implemented production course, or not the correction of the previously adopted plan is made.

It is worth noting that in the proposed search process, besides modelling control procedures coordinating cooperation of workstations, transport and storage equipment as well as robots and whole production processes, can also be determined schedules of workspaces, tools, waste, and auxiliary fastening devices flows as well as the functioning of modelled robots and auxiliary devices used in these processes.

6. CONCLUSIONS

Most of the methods used to model systems and the course of production processes carried out in them are based on techniques that implement Petri net formalisms. The advantage of this model type is the possibility of using computer simulation techniques to assess alternative scenarios of the modeled processes. Unfortunately, a significant shortage of such solutions, occurring in most studies of interactions of asynchronously occurring events, is associated with the suspension of simulation programs. The approach proposed in our paper fills this gap by offering the method of automatic synthesis of network models implementing mechanisms that prevent the deadlocks occurrence and consequently prevent the suspension of simulation programs. To sum up, our proposal significantly increases the effectiveness of appropriate decision support systems used in designing FMS class systems.

The presented methodology makes it possible to comprehensively cover various tasks of design and operation (control and management) of FMS. The proposed approach provides a robust framework for simultaneous optimization of the layout of machining centers, conveyors, robots, buffers, and the production flow scenario.

In the general case, it can be implemented in DSSs supporting the operational planning of production orders. It can also be used in online batching and routing production orders, resource allocation, and task scheduling, among many other applications.

However, among its more essential shortcomings, one should mention the lack of possibility to analyze manufacturing processes, in which flows of workpieces form the structure of a partially ordered graph (occurring, for example, in car assembly processes) and the lack of possibility to analyze the influence of stochastic disturbances. These issues can be addressed in future studies.

REFERENCES

Alexopoulos, K., Anagiannis, I., Nikolakis, N., & Chryssolouris, G. (2022). A quantitative approach to resilience in manufacturing systems. *International Journal of Production Research*, *60*(13), 4342–4360.

Bakar, B. A., Henry, R. M., & Ali, M. (1991). An alternative approach in batch process control implementation using hierarchical Petri nets, World Scientific. *Proc. of the International Conference on Computer Integrated Manufacturing* (pp. 171–174).

Banaszak, Z. (1992). Synchronisation of robots in flexible assembly systems. *Archiwum Budowy Maszyn*, *39*(1–2), 117–133.

Banaszak, Z., Skolud, B., & Zaremba, M. B. (2003). Computer-aided prototyping of production flows for virtual enterprise. *Journal of Intelligent Manufacturing*, *14*, 83–106.

Bocewicz, G., Wójcik, R., Witczak, M., & Banaszak, Z. (2022). Petri Net Approach to Automated Modelling and Performance Evaluation for Robotic Assembly Systems. *2022 26th International Conference on Methods and Models in Automation and Robotics (MMAR)* (pp. 306–311). IEEE. https://doi.org/10.1109/MMAR55195.2022.9874291

Bujari, A., Calvio, A., Foschini, L., Sabbioni, A., & Corradi, A. (2021). A Digital Twin Decision Support System for the Urban Facility Management Process. *Sensors*, *21*(24), 8460. https://doi.org/10.3390/s21248460

Claes, D., & Tuyls, K. (2018). Multi robot collision avoidance in a shared workspace. *Autonomous Robots, 42*, 1749–1770. https://doi.org/10.1007/s10514-018-9726-5

Coito, T., Faria, P., Martins, M. S. E., Firme, B., Vieira, S. M., Figueiredo, J., & Sousa, J. M. C. (2022). Digital Twin of a Flexible Manufacturing System for Solutions Preparation. *Automation*, *3*(1), 153–175. https://doi.org/10.3390/automation3010008

David, J., Lobov, A., & Lanz, M. (2018). Leveraging Digital Twins for Assisted Learning of Flexible Manufacturing Systems. *2018 IEEE 16th International Conference on Industrial Informatics (INDIN)* (pp. 529-535). IEEE. https://doi.org/10.1109/INDIN.2018.8472083

Hatono, I., Katoh, N., Yamagata, K., & Tamura, H. (1989). Modelling of FMS under uncertainty using stochastic Petri Nets. *Proc. of the 3rd International Workshop on Petri nets and performance models* (pp. 122–130).

He, Z., Zhang, R., Ran, N., & Gu, C. (2022). Path Planning of Multi-Type Robot Systems with Time Windows Based on Timed Colored Petri Nets. *Applied Science*, *12*(14), 6878. https://doi.org/10.3390/app12146878

Heiner, M. (1992). *Petri net based software validation (prospects and limits), Technical report No. TR-92-022.* International Computer Science Institute.

Janardhanan, M. N., Li, Z., Bocewicz, G., Banaszak, Z., & Nielsen, P. (2019). Metaheuristic Algorithms for balancing robotic assembly lines with sequence-dependent robot setup times. *Applied Mathematical Modelling*, *65*, 256–270.

Jensen, K. (1987). Computer tools for construction, modification and analysis of Petri nets. *Lecture Notes on Computer Science* (No. 255). Springer Verlag.

Jonsson, P. (2000). An empirical taxonomy of advanced manufacturing technology. *International Journal of Operations & Production Management*, *20*(12), 1446–1474.

Laemmle, A., & Gust, S. (2019). Automatic layout generation of robotic production cells in a 3D manufacturing simulation environment. *Procedia CIRP*, *84*, 316–321.

Makris, S., Michalos, G., & Chryssolouris, G. (2012). Virtual Commissioning of an Assembly Cell with Cooperating Robots. *Advances in Decision Sciences*, *2012*, 428060. https://doi.org/10.1155/2012/428060

Manu, G., Kumar, V. M., Nagesh, H., Jagadeesh, D., & Gowtham, M. B. (2018). Flexible Manufacturing Systems (FMS): A Review. *International Journal of Mechanical and Production Engineering Research and Development*, *8*(2), 323–336.

Neto, A. A., Carrijoa B. S., Brock, J. G. R, Deschamps, F., & Lima, E. P. (2021). Digital twin-driven decision support system for opportunistic preventive maintenance scheduling in manufacturing. *Procedia Manufacturing*, *55*, 439–446.

Nielsen, L. D., Sung, I., & Nielsen, P. (2019). Convex Decomposition for a Coverage Path Planning for Autonomous Vehicles: Interior Extension of Edges. *Sensors*, *19*(19), 4165. https://doi.org/10.3390/s19194165

Nielsen, P., Michna, Z., & Do, N. A. D. (2014). An Empirical Investigation of Lead Time Distributions. *Advances in Production Management Systems. Innovative and Knowledge-Based Production Management in a Global-Local World. APMS 2014. IFIP Advances in Information and Communication Technology* (vol. 438). Springer. https://doi.org/10.1007/978-3-662-44739-0_53

Patalas-Maliszewska, J., & Kłos, S. (2019). An Approach to Supporting the Selection of Maintenance Experts in the Context of Industry 4.0. *Applied Sciences*, *9*(9), 1848. https://doi.org/10.3390/app9091848

Rachamadugu, R., & Stecke, K. E. (1994). Classification and review of FMS scheduling procedures. *Production Planning & Control*, *5*(1), 2–20. https://doi.org/10.1080/09537289408919468

Recalde, L., Silva, M., Ezpeleta, J., & Teruel, E. (2022). Petri Nets and Manufacturing Systems: An Examples-Driven Tour. *ACPN 2003. Lecture Notes in Computer Science* (vol. 3098). Springer. https://doi.org/10.1007/978-3-540-27755-2_21

Reisig, W. (1982). *Petri nets*. Springer Verlag.

Reutenauer, Ch. (1988). *The mathematics of Petri nets*. Englewood Cliffs.

Silva, E. B., Costa, M. G., Silva, M. F., & Pereira, F. H. (2012). Evaluation of Production Sequencing Rules in Job Shop and Flow Shop Environment through Computer Simulation. *ICIEOM 2012* (no. 257).

Sliwa, M., & Patalas-Maliszewska, J. (2016). A Strategic Knowledge Map for the Research and Development Department in a Manufacturing Company. *Foundations of Management*, *8*(1), 151–166.

Stączek, P., Pizoń, J., Danilczuk, W., & Gola, A. (2021). A digital twin approach for the improvement of an autonomous mobile robots (AMR's) operating environment – a case study. *Sensors*, *21*(23), 7830. https://doi.org/10.3390/s21237830

Świć, A., & Gola, A. (2013). Economic Analysis of Casing Parts Production in a Flexible Manufacturing System. *Actual Problems of Economics*, *141*(3), 526–533.

Vaisi, B. (2022). A review of optimization models and applications in robotic manufacturing systems: Industry 4.0 and beyond. *Decision Analytics Journal*, *2*, 100031. https://doi.org/10.1016/j.dajour.2022.100031

Van der Aalst, W. M. (1992). *Timed coloured Petri nets and their application to logistics*. Technische Universiteit Eindhoven.

Viswandham, N., & Narahari, Y. (1992). *Performance modelling of automated manufacturing systems*. Prentice-Hall.

Yang, B., & Hu, H. (2022). Maximally Permissive Deadlock and Livelock Avoidance for Automated Manufacturing Systems via Critical Distance. In *IEEE Transactions on Automation Science and Engineering*. IEEE. https://doi.org/10.1109/TASE.2021.3138169

Zanchettin, A. M. (2021). Robust scheduling and dispatching rules for high-mix collaborative manufacturing systems. *Flexible Services and Manufacturing Journal*, *34*, 293–316. https://doi.org/10.1007/s10696-021-09406-x

Zhang, F., Bai, J., & Yang, D. (2022). Digital twin data-driven proactive job-shop scheduling strategy towards asymmetric manufacturing execution decision. *Scientific Reports*, *12*, 1546. https://doi.org/10.1038/s41598-022-05304-w

Zhou, K. Q., & Zain, A. M. (2016). Fuzzy Petri nets, and industrial applications: a review. *Artificial Intelligence Review*, *45*(4), 405–446. https://doi.org/10.1007/s10462-015-9451-9

Applied Computer Science, vol. 18, no. 3, pp. 19–30
doi: 10.35784/acs-2022-18

Submitted: 2022-07-15 | Revised: 2022-09-20 | Accepted: 2022-09-23

Keywords: ECG signal, Wavelet transforms, WDFR algorithm, R peak determination, Adaptive threshold

Thanh-Nghia NGUYEN [0000-0001-7366-2257]*, *Thanh-Hai NGUYEN* [0000-0003-3270-6975]*, *Ba-Viet NGO* [0000-0002-8379-957X]*

R PEAK DETERMINATION USING A WDFR ALGORITHM AND ADAPTIVE THRESHOLD

Abstract

The determination of the R peak position in the ECG signal helps physicians not only to know the heart rate per minute, but also to monitor the patient's health related to heart disease. This paper proposes a system to accurately determine the R peak position in the ECG signal. The system consists of a pre-processing block for filtering out noise using a WDFR algorithm and highlighting the amplitude of the R peak and a threshold value is calculated for determining the R peak. In this research, the MIT-BIH ECG dataset with 48 records are used for evaluation of the system. The results of the SEN, +P, DER and ACC parameters related to the system quality are 99.70%, 99.59%, 0.70% and 99.31%, respectively. The obtained performance of the proposed R peak position determination system is very high and can be applied to determine the R peak of the ECG signal measuring devices in practice.

1. INTRODUCTION

Information of ECG signal is very important for monitoring and diagnosing patient heart diseases (Chen et al., 2021; Rahman & Jambek, 2019; Ribeiro et al., 2020). In particular, the R peak of the QRS complex in the ECG signal is an important information which can allow a physician to determine the beat-per-minute parameter of patient. Therefore, the R peak determination may be applied in heart disease classification systems to produce more accurate results (Darmawahyuni et al., 2021; Mohebbanaaz, Sai & Kumari, 2021; Olanrewaju et al., 2021; Wu et al., 2021). In which one can determine heartbeats in one ECG signal based on the position of the R peak in the QRS complex. With the determined heartbeats or heart rhythms, heart disease categories may be classified using deep learning networks (Alhussainy & Jasim, 2021; Aziz, Ahmed & Alouini, 2021; Dang et al., 2019; Meqdad, Abdali-Mohammadi & Kadry, 2022; Nguyen & Nguyen, 2021). For classifying the heart disease categories, each heartbeat based on the R peak needs to be labelled by heart disease imaging experts. Therefore, the accurate position of the R peak in the signal is determined plays an important role in classifying the heart diseases using the deep learning network. This paper proposes a method to accurately determinate the R peak position of the QRS complex in the ECG signal.

* Department of Industrial Electronics and Biomedical Engineering, HCMC University of Technology and Education, Ho Chi Minh, Vietnam, nghiant@hcmute.edu.vn nthai@hcmute.edu.vn, vietnb@hcmute.edu.vn

Filtering the noise in the ECG signal for accurately determining the R peak positions is a necessary task. ECG signal often has many different noises such as baseline wander (BW), powerline interference (LPI), and artifact, in which noisy filtering in R peak determination systems is always applied (Chen et al., 2020; Lee et al., 2018; Lin et al., 2019; Nguyen, Nguyen & Ngo, 2020; Xiang, Lin & Meng, 2018; Zhang, Li & Li, 2020). Therefore, with best filtering out the noise components in the ECG signal, it is possible to more accurately determine the R peak position in the ECG signal. In (Qin et al., 2017), authors have proposed a wavelet-based multiresolution analysis (WMRA) method for filtering noise in the ECG signal and then the filtered ECG signal was inverted before determining the position of the R peak using an adaptive threshold. For evaluating the effectiveness of the proposed method, MIT-BIH database (MITDB) and the QT database (QTDB) were used in this research, particularly, the accuracies of the R peak determination with MITDB and QTBD databased are 98.89% and 99.73%, respectively.

The artificial neural network method has been applied to determine R-peaks in ECG signals in recent years (Cai & Hu, 2020; Laitala et al., 2020; Zahid et al., 2021). In this method, several data points around the R peak position are used to be input data for training and testing the neural network. Moreover, the R peaks position determination results are often evaluated using a confusion matrix method. In (Zhou et al., 2020), Peishan Zhou et al. proposed to employ an one-dimensional convolution network (1D CNN) with a long short-term memory (LSTM) network for detecting R peaks in ECG signals. In particular, in this paper, the proposed neural network structure includes 13 layers with 6 layers of the convolution, 3 layers of max-pooling, 1 layer of LSTM and 3 layers of full-connected. Three ECG signals including 112, 122, and 117 records were randomly selected from the MIT-BIH database for evaluating the proposed system and the accuracy of an R-peak position determination system is 90.61%.

In order to evaluate the performance of the R-peak position determination system in ECG signals, some parameters such as values of TP, FP and FN are often used. The peak R position determination results from the recognition system are compared with the actual R-peak position for calculating the values of SEN, $+P$, DER and ACC (Park, Lee & Park, 2017). From these values, if the obtained SEN, $+P$, and ACC are large, while DER has a smaller value, the R peak position determination system will produce more accurately. Furthermore, the waveform of the ECG signal with the position of the identified R peak is presented to demonstrate the performance of the R peak position determination system. Another problem is that one ECG signal has a special R peak position with low amplitude, but the system is still determined the R peak position, called the well system.

With the improved noise filter on the ECG signal, a deep learning network or other classification network topologies for peak R position determination in QRS complex can be applied and the accuracy of the peak R position determination using one of these algorithms is high (Al et al., 2021; Jang et al., 2022; Suboh et al., 2020). However, for the ECG signals with huge noise effects, the problem of accurately determining the position of the R peaks in the QRS complex is a challenge (Nguyen et al., 2019). Therefore, the application of the deep learning network algorithm to locate the peak R in the QRS complex can obtain high accuracy. However, some R peak locating systems often have a large processing time, so it is difficult to apply for real-time R peak locators.

In this paper, a method of the R peak position determination system is proposed. In practice, one ECG signal is preprocessed using filters to eliminate noises using a Wavelet Decomposition Filter-Reconstruction (WDFR) algorithm. Hence, the filtered ECG signal is used to calculate the threshold for determining the R peak position. Therefore, the rest of this paper is organized as follows: Section-2 presents related fundamental knowledge and proposed method. The experimental results and discussion are described in Section-3. The conclusion of the article is shown in the final section.

2. METHODOLOGY

This paper proposes a system to determine the R peak position in the QRS complex of one ECG signal. In particular, noise of the ECG signal is eliminated using the WDFR algorithm, in which a wavelet decomposition and filter reconstruction are combined to perform filtering the noise. Therefore, the ECG signal with the filtered noise will be passed through the differential, squared, and convolution blocks to enhance the amplitude of the R peaks. Finally, the threshold value will be calculated to determine the R peak position. The results of determining the R peak position will be combined with the standard R peak position for evaluating the performance of the system.

2.1. Proposed R peak determination

To determine the R peak position in the ECG signal, a system is built as shown in Figure 1. Therefore, a set of ECG signals is used to combine with the input to the system for determining the R peaks. In addition, the ECG signal is preprocessed to remove noise in the ECG signal and then the system can transform the ECG signal for easily detecting the R peak. Thus, the ECG signal after preprocessing will be used to calculate the threshold for determining the R peak position. The result of the R peak position will be evaluated based on the standard R peak position.

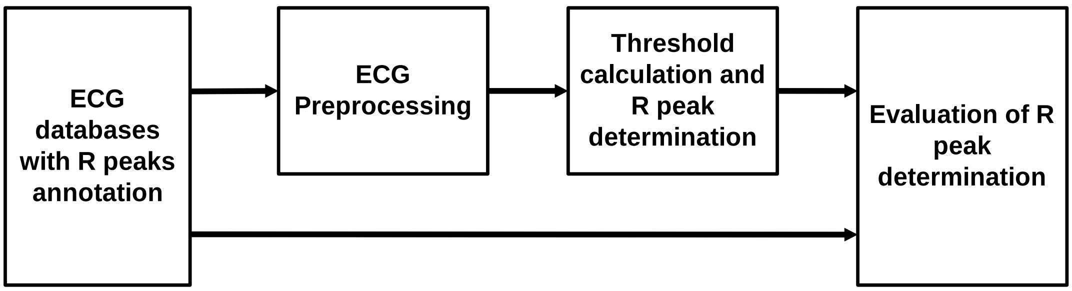

Fig. 1. Block diagram of the R peak determination system

In this paper, the set of ECG signals is obtained from the MIT-BIH database (Moody & Mark, 2001). The set consists of 48 records from 47 patients with R peak positions marked by physicians. Each ECG signal record was acquired with a duration of 30 minutes and has a total of 65,000 points. Moreover, the set of the ECG signals has been used in many research projects and has high reliability.

2.2. ECG signal preprocessing

The ECG signal was filtered using the WDFR algorithm as described in Figure 2 (Nguyen, Nguyen & Ngo, 2020), particularly the ECG signal is decomposed into detailed and approximate components with different frequencies using a wavelet transform at Level-8. Therefore, the approximation and detail components will be used to create threshold for noise filtering. Finally, the signal components after noise filtering based on the threshold will be reconstructed to produce the ECG signal with the least noise.

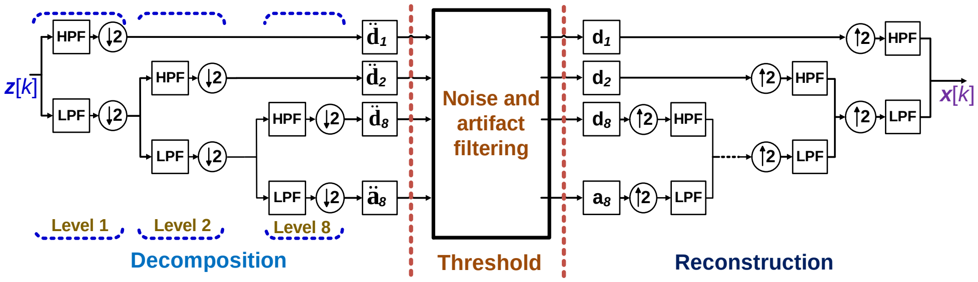

Fig. 2. The representation of the WDFR algorithm for eliminating noise of ECG signal

The approximation and detail components obtained after applying the wavelet transform are presented as follows:

$$\ddot{d}_m = \sum_{k=-\infty}^{\infty} z[k]h[2n-k] \tag{1}$$

$$\ddot{a}_m = \sum_{k=-\infty}^{\infty} z[k]g[2n-k] \tag{2}$$

where: $h[2n-k]$ – the high pass filter,
$g[2n-k]$ – presents the low pass filter,
$\ddot{d}_m$ – the detail component,
$\ddot{a}_m$ – the approximation component,
$z[k]$ – the ECG signal.

The approximation and detail components obtained after applying the threshold to eliminate noise and artifacts are expressed as follows:

$$a_m = \begin{cases} 0 & \text{if } f_{\ddot{a}_m} < f_a \\ \ddot{a}_m & otherwise \end{cases} \tag{3}$$

$$d_m = \begin{cases} 0 & \text{if } f_{\ddot{a}_m} < f_a \\ \ddot{a}_m & otherwise \end{cases} \tag{4}$$

where: f_a – the maximum frequency of the BW noise,
$f_{\ddot{a}_m}$ – the frequency of $\ddot{a}_m$,
f_d – a maximum frequency of ECG information,
$f_{\ddot{d}_m}$ – the frequency of $\ddot{d}_m$.

The filtered ECG signal $x[k]$ obtained from a_m and d_m is determined as follows (Kumar, Kumar & Pandey, 2012):

$$x[k] = a_m + \sum_{i=0}^{m} d_i \tag{5}$$

Therefore, the filtered ECG signal will be passed through the differential block to find the slope peak of the QRS complex. The signal is further fed through the square block to enhance the amplitude of the slope crest. Finally, the signal will be passed through the integration block to merge the adjacent peaks for accurately identifying one R peak. Furthermore, a moving window with 24 data points is used for tradeoff between false and missed detections. The process of differentiation, squaring, and integration is summarized and described as follows (Lu, Pan & Yu, 2018):

$$p(nT) = \frac{1}{8}[-x(nT-2T) - 2x(nT-T) + 2x(nT+T) + x(nT+2T) \tag{6}$$

$$k(nT) = [p(nT)]^2 \tag{7}$$

$$r(nT) = \frac{1}{N}[p(nT-(N-1)T) - p(nT-(N-2)T) + \cdots + p(nT)] \tag{8}$$

where: $y(nT)$ – the outputs of the differentiation stages,
$k(nT)$ – the outputs of the squaring stages,
$r(nT)$ – the outputs of the integration stages,
N – the number of samples in the moving window.

From the ECG signal after preprocessing, the threshold method is applied to determine the position of the peak R. The formula for determining the threshold is presented as follows:

$$\begin{gathered} \mathrm{M_{VAL}} = \max\left(\mathrm{ECG}_{pre}\,(1:300)\right) \\ \mathrm{SPK} = 0.13 * \mathrm{M_{VAL}} \\ \mathrm{NPK} = 0.1 * \mathrm{SPK} \end{gathered} \tag{9}$$

$$\mathrm{THRE} = 0.25 * \mathrm{SPK} + 0.75 * \mathrm{NPK} \tag{10}$$

where: $\mathrm{M_{VAL}}$ – the maximum 300 data points of the ECG signal,
ECG_{pre} – the ECG signal after pre-processing,
SPK – the R peak,
NPK – the noise peak,
THRE – the threshold.

In this system, if no data point is detected after using 400 data points, the SPK value will be updated again using the formula of $\mathrm{SPK} = 0.5 * \mathrm{SPK}$ for adaptive threshold.

2.3. Evaluation of R peak detection

To evaluate the R peak detection performance, the parameters of true positive (TP), false positive (FP), and false negative (FN) are applied. In particular, TP is called the R peak, when it is correctly identified; FP is the R peak, but the system can not detect it; and FN is not the R peak, while the system identifies it as the R peak. In addition, the parameters of accuracy (ACC), sensitivity (SEN), positive predictability ($+P$), detection error rate (DER), are calculated from TP, FN and FP as follows (Park, Lee & Park, 2017; Sharma & Sunkaria, 2016; Zalabarria et al., 2020):

$$ACC = \frac{TP}{TP+FN+FP} \times 100\% \quad (11)$$

$$SEN = \frac{TP}{TP+FN} \times 100\% \quad (12)$$

$$+P = \frac{TP}{TP+FP} \times 100\% \quad (13)$$

$$DER = \frac{FN+FP}{TP} \times 100\% \quad (14)$$

3. RESULTS AND DISCUSSION

To evaluate the performance of the proposed R peak determination system, the MIT-BIH ECG dataset is used in this research. The original ECG signal and the signals after preprocessing are shown in Figure 3, in which the original ECG signal with 2000 data points taken from the record 117 of the MIT-BIH dataset is presented.

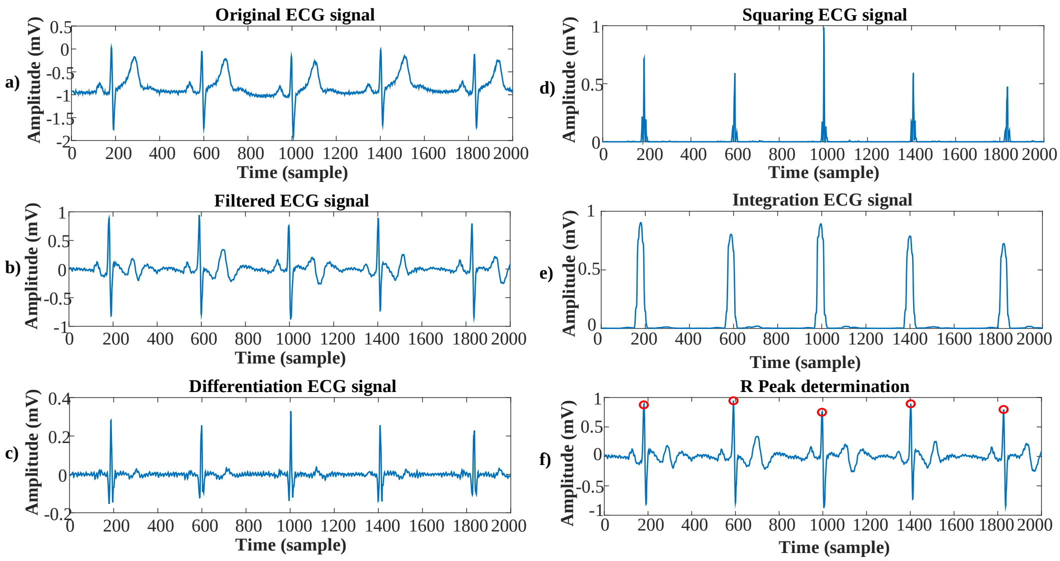

Fig. 3. Results of preprocessing the ECG signal using the MIT-BIH database

Therefore, this signal is filtered to eliminate noise using the WDFR algorithm with the wavelet function “dmey”. In this WDFR algorithm, the detail components d_1, d_2, d_3 and the approximation component a_8 are filtered out of the ECG signal. It is obvious that Figure 3b shows that the ECG signal has been filtered the noise of the BW components and high frequency components compared to the original signal in Figure 3a. Moreover, the R peaks of the QRS complex in the filtered signal are more obviously seen and are easy to determine their R peak positions.

The ECG signal after filtering noise will be differentially calculated to determine the amplitude of the R peaks in the QRS complex as shown in Figure 3c. Thus, this signal is squared to enhance the amplitude of the R peak positions as described in Figure 3d. Finally, the signal is passed through the integration block to arrange all the R peaks together to avoid the wrong detection of 2 R peak positions too close together as shown in Figure 3e. The adaptive threshold value will be calculated and updated to determine the position of the R peak and also we can see that the R peak positions are accurately determined correctly in Figure 3f.

In this paper, the parameters of TP, FN and FP are used for evaluating the performance of the R peak position determination system in the QRS complex as described as shown in Figure 4. In particular, Figure 4a shows the actual R peak position and Figure 4b shows the R peak position determined from the system, in which TP, FN and FP are defined based on the R peak positions. Therefore, FN is the number of the undetected R peaks; FP is the number of the R peaks mistakenly detected by the system; TP is the number of the correctly detected R peaks.

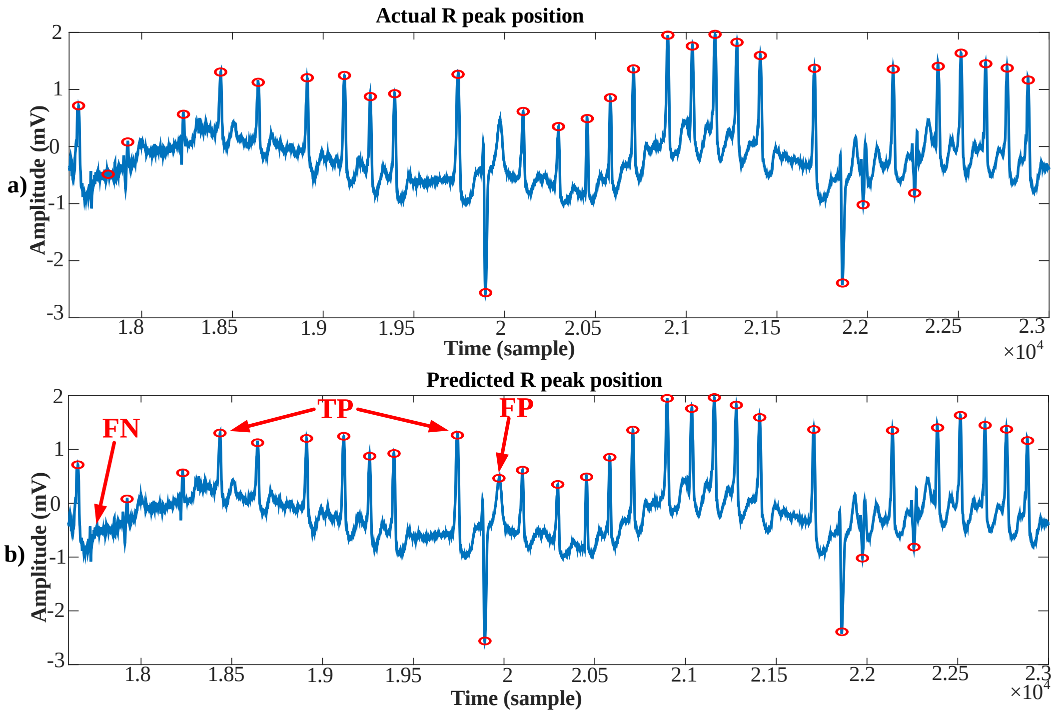

Fig. 4. Representation of TP, FN and FP in the R peak determination result

From the TP, FN and FP parameters, the values of ACC, SEN, $+P$, and DER will be calculated for evaluating the performance of the proposed R peak determination system. In particular, if the obtained ACC, SEN, and $+P$, values are large and the obtained DER value is small, then the proposed system is very good. Table 1 presents the evaluation results about the performance of the R peak position determination system using the MIT-BIH ECG dataset, in which the dataset consists of 48 records and the parameters are calculated for each record. From Table 1, it can be seen that the results of determining the R peak positions using the proposed system are effective, in which the mean values of ACC, SEN, $+P$, and DER are 99.31%, 99.70%, 0.70%, and 99.60%, respectively.

From Table 1, it is obvious that the performance of the proposed R peak position determination system is effective, particularly, most of the ECG signals in the MIT-BIH dataset have the accuracy of over 98%. However, with record 207, the obtained accuracy is only 85.53%. The reason is that record 207 has some signal segments with too much noise as shown in Figure 5.

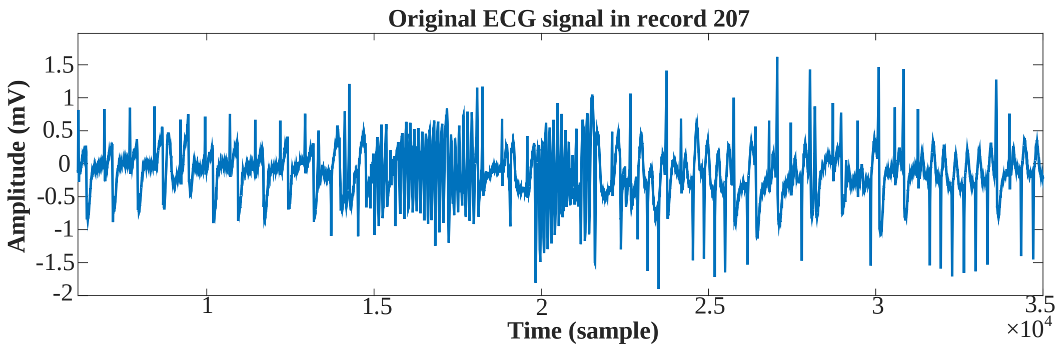

Fig. 5. Representation of original ECG signal in record 207 with huge noise

Tab. 1. The performance of the R peak determination system using the MIT-BIH database

No.	Records	R peaks	TP	FN	FP	SEN	$+P$	DER	ACC
1	100	2273	2273	0	0	100.00	100.00	0.00	100.00
2	101	1865	1865	1	0	99.95	100.00	0.05	99.95
3	102	2187	2187	0	0	100.00	100.00	0.00	100.00
4	103	2084	2084	0	0	100.00	100.00	0.00	100.00
5	104	2229	2220	8	9	99.64	99.60	0.77	99.24
6	105	2572	2545	12	27	99.53	98.95	1.53	98.49
7	106	2027	2017	7	10	99.65	99.51	0.84	99.16
8	107	2137	2136	4	1	99.81	99.95	0.23	99.77
9	108	1763	1761	0	2	100.00	99.89	0.11	99.89
10	109	2532	2528	2	4	99.92	99.84	0.24	99.76
11	111	2124	2124	1	0	99.95	100.00	0.05	99.95
12	112	2539	2539	0	0	100.00	100.00	0.00	100.00
13	113	1795	1795	0	0	100.00	100.00	0.00	100.00
14	114	1879	1841	23	38	98.77	97.98	3.31	96.79
15	115	1953	1953	0	0	100.00	100.00	0.00	100.00
16	116	2412	2405	4	7	99.83	99.71	0.46	99.54
17	117	1535	1519	14	16	99.09	98.96	1.97	98.06
18	118	2278	2278	0	0	100.00	100.00	0.00	100.00
19	119	1987	1987	1	0	99.95	100.00	0.05	99.95
20	121	1863	1863	0	0	100.00	100.00	0.00	100.00
21	122	2476	2475	0	1	100.00	99.96	0.04	99.96
22	123	1518	1518	0	0	100.00	100.00	0.00	100.00
23	124	1619	1619	0	0	100.00	100.00	0.00	100.00
24	200	2601	2601	2	0	99.92	100.00	0.08	99.92
25	201	1963	1936	8	27	99.59	98.62	1.81	98.22
26	202	2136	2130	10	6	99.53	99.72	0.75	99.25
27	203	2980	2955	37	25	98.76	99.16	2.10	97.94
28	205	2656	2651	17	5	99.36	99.81	0.83	99.18
29	207	2332	2116	142	216	93.71	90.74	16.92	85.53
30	208	2955	2954	4	1	99.86	99.97	0.17	99.83
31	209	3005	3005	0	0	100.00	100.00	0.00	100.00
32	210	2650	2650	0	0	100.00	100.00	0.00	100.00
33	212	2748	2748	3	0	99.89	100.00	0.11	99.89
34	213	3251	3251	1	0	99.97	100.00	0.03	99.97
35	214	2262	2262	0	0	100.00	100.00	0.00	100.00
36	215	3363	3363	0	0	100.00	100.00	0.00	100.00
37	217	2208	2200	5	8	99.77	99.64	0.59	99.41
38	219	2154	2154	0	0	100.00	100.00	0.00	100.00
39	220	2048	2048	0	0	100.00	100.00	0.00	100.00
40	221	2427	2426	3	1	99.88	99.96	0.16	99.84
41	222	2483	2483	0	0	100.00	100.00	0.00	100.00
42	223	2605	2605	4	0	99.85	100.00	0.15	99.85
43	228	2053	2024	13	29	99.36	98.59	2.08	97.97
44	230	2256	2256	0	0	100.00	100.00	0.00	100.00
45	231	1571	1571	0	0	100.00	100.00	0.00	100.00
46	232	1780	1777	0	3	100.00	99.83	0.17	99.83
47	233	3079	3079	2	0	99.94	100.00	0.06	99.94
48	243	2753	2753	0	0	100.00	100.00	0.00	100.00
Total/Average		**109966**	**109530**	**328**	**436**	**99.70**	**99.60**	**0.70**	**99.31**

Tab. 2. Comparison of R peak determination with other methods

Authors	R peaks	TP	FN	FP	SEN	$+P$	DER	ACC
Unai Zalabarria *et al.* (Zalabarria et al., 2020)	106,581	106,096	485	431	99.54	99.60	0.86	99.14
Qin Qin *et al.* (Qin et al., 2017)	109,966	109,298	668	561	99.39	99.49	1.12	98.89
Lakhan Dev Sharma *et al.* (Sharma & Sunkaria, 2016)	109,488	108,979	509	428	99.50	99.56	0.93	99.08
Proposed method, 2022	109966	109530	328	436	99.70	99.59	0.70	99.31

The results of determining the R peak position are compared with previous works for evaluating the performance of the proposed system as shown in Table 2. In particular, Unai Zalabarria et al. (Zalabarria et al., 2020) proposed a system for determining the peak R position, including preprocessing, detecting the region containing the R peak and iterative smart processing to accurately determine the R peak. In the preprocessing block, the signal was filtered the BW noise applying moving median filtering and a cubic interpolation. The accuracy and DER obtained using the MIT-BIH dataset are 99.14% and 0.86%, respectively. Another research is that Qui Qui et al. (Qin et al., 2017) et al. proposed a Wavelet-based Multiresolution Analysis (WMRA) method for filtering the noise on the ECG signal for determining the R peak position. The obtained accuracy is 98.9% and DER is 1.12% using the MIT-BIH dataset.

In (Sharma & Sunkaria, 2016), Lakhan Dev Sharma et al. applied filters of two-stage median and Savitzky–Golay smoothing for pre-processing to remove noise on ECG signals. Moreover, the root-mean-square method was employed for determining the region containing the QRS complex for detecting of the R peak. The MIT-BIH dataset was used to evaluate the system quality based on the obtained results, in which the accuracy and DER are 99.08% and 0.93%, respectively. In this research, we proposed an ECG signal preprocessing system by applying the WDFR algorithm for filtering noise, in which differentiation, squaring, and integration methods were employed to highlight the QRS complex. Therefore, a threshold was applied for determining the R peak position and the obtained accuracy and DER using the MIT-BIH dataset are 99.31% and 0.70%, respectively.

4. CONCLUSIONS

This paper proposed a system for determining the R peak position in the QRS complex of the ECG signal based on the signal processing method. In particular, the ECG dataset was filtered to remove noise components using the WDFR algorithm. The ECG after filtering the noise was processed to enhance the amplitude of the R peak for determining the R peaks more accurately using the differentiation, squaring, and integration algorithm. Therefore, the threshold value was calculated based on the determined R peak positions. For evaluation of the systemquality, the MIT-BIH ECG dataset was employed and the obtained accuracy result of the proposed R peak position system is 99.31%. However, for ECG signals with a large amount of noise such as the signal 207, the accuracy of the R peak position determination still needs to be improved. With the R peak positions accurately determined, a deep learning network applied for classifying heart diseases may make a highly increasing performance. In future work, we will apply the proposed R peak position determination algorithm to locate R peak and then calculate the beat-per-minute ratio for the measured ECG wearable device.

Acknowledgments

This work is supported by Ho Chi Minh City University of Technology and Education (HCMUTE) under Grant No. T2021-52TĐ.

Conflicts of Interest

The authors declare that we don't have any conflict of interest regarding this article.

REFERENCES

Al, Z. M. A., Thapa, K., & Yang, S.-H. (2021). Improving R Peak Detection in ECG Signal Using Dynamic Mode Selected Energy and Adaptive Window Sizing Algorithm with Decision Tree Algorithm. *Sensors*, *21*(19), 6682–6699. https://doi.org/10.3390/s21196682

Alhussainy, A. M. H., & Jasim, A. D. (2021). Training feedforward neural network using genetic algorithm to diagnose left ventricular hypertrophy. *TELKOMNIKA Telecommunication, Computing, Electronics and Control*, *18*(3), 1285–1291. https://doi.org/10.12928/TELKOMNIKA.v18i3.15225

Aziz, S., Ahmed, S., & Alouini, M.-S. (2021). ECG-based machine-learning algorithms for heartbeat classification. *Scientific Reports*, *11*(1), 18738-18752. https://doi.org/10.1038/s41598-021-97118-5

Cai, W., & Hu, D. (2020). QRS Complex Detection Using Novel Deep Learning Neural Networks. *IEEE Access*, *8*, 97082–97089. https://doi.org/10.1109/ACCESS.2020.2997473

Chen, A., Zhang, Y., Zhang, M., Liu, W., Chang, S., Wang, H., He, J., & Huang, Q. (2020). A Real Time QRS Detection Algorithm Based on ET and PD Controlled Threshold Strategy. *Sensors (Basel)*, *20*(14), 4003–4018. https://doi.org/10.3390/s20144003

Chen, L., Yu, H., Huang, Y., & Jin, H. (2021). ECG Signal-Enabled Automatic Diagnosis Technology of Heart Failure. *J Healthc Eng*, *2021*, 5802722–5802730. https://doi.org/10.1155/2021/5802722

Dang, H., Sun, M., Zhang, G., Qi, X., Zhou, X., & Chang, Q. (2019). A Novel Deep Arrhythmia-Diagnosis Network for Atrial Fibrillation Classification Using Electrocardiogram Signals. *IEEE Access*, *7*, 75577–75590. https://doi.org/10.1109/ACCESS.2019.2918792

Darmawahyuni, A., Nurmaini, S., Rachmatullah, M. N., Firdaus, F., & Tutuko, B. (2021). Unidirectional-bidirectional recurrent networks for cardiac disorders classification. *TELKOMNIKA Telecommunication, Computing, Electronics and Control*, *19*(3), 902–910. https://doi.org/10.12928/TELKOMNIKA.v19i3.18876

Jang, J., Park, S., Kim, J.-K., An, J., & Jung, S. (2022). CNN-based Two Step R Peak Detection Method: Combining Segmentation and Regression. In *2022 44th Annual International Conference of the IEEE Engineering in Medicine & Biology Society (EMBC)* (pp. 1910–1914). IEEE.

Kumar, A., Kumar, R., & Pandey, R. K. (2012). ECG Signal Compression using Optimum Wavelet Filter Bank Based on Kaiser Window. *Procedia Engineering*, *38*(1), 2889–2902. https://doi.org/https://doi.org/10.1016/j.proeng.2012.06.338

Laitala, J., Jiang, M., Syrjälä, E., Naeini, E. K., Airola, A., Rahmani, A. M., Dutt, N. K. & Liljeberg, P. (2020). Robust ECG R-peak detection using LSTM. In SAC '20: Proceedings of the 35th Annual ACM Symposium on Applied Computing (pp. 1104–1111). ACM Digital Library.

Lee, M., Park, D., Dong, S.-Y., & Youn, I. (2018). A Novel R Peak Detection Method for Mobile Environments. *IEEE Access*, *6*, 51227–51237. https://doi.org/10.1109/ACCESS.2018.2867329

Lin, C.-C., Chang, H.-Y., Huang, Y.-H., & Yeh, C.-Y. (2019). A Novel Wavelet-Based Algorithm for Detection of QRS Complex. *Applied Sciences*, *9*(10), 2142–2161. https://doi.org/10.3390/app9102142

Lu, X., Pan, M., & Yu, Y. (2018). QRS Detection Based on Improved Adaptive Threshold. *J Healthc Eng*, *2018*, 5694595–5694604. https://doi.org/10.1155/2018/5694595

Meqdad, M. N., Abdali-Mohammadi, F., & Kadry, S. (2022). Meta Structural Learning Algorithm with Interpretable Convolutional Neural Networks for Arrhythmia Detection of Multi-Session ECG. *IEEE Access*, *10*, 61410–61425. https://doi.org/10.1109/ACCESS.2022.3181727

Mohebbanaaz, M., Sai, Y. P., & Kumari, L. V. R. (2021). Detection of cardiac arrhythmia using deep CNN and optimized SVM. *Indonesian Journal of Electrical Engineering and Computer Science*, *24*(2), 217–225. https://doi.org/10.11591/ijeecs.v24.i1

Moody, G. B., & Mark, R. G. (2001). The impact of the MIT-BIH Arrhythmia Database. *IEEE Engineering in Medicine and Biology Magazine*, *20*(3), 45–50. https://doi.org/10.1109/51.932724

Nguyen, T.-N., Nguyen, T.-H., & Ngo, V.-T. (2020). Artifact elimination in ECG signal using wavelet transform. *TELKOMNIKA Telecommunication, Computing, Electronics and Control*, *18*(2), 936–944. https://doi.org/10.12928/telkomnika.v18i2.14403

Nguyen, T.-N., & Nguyen, T.-H. (2021). Deep Learning Framework with ECG Feature-Based Kernels for Heart Disease Classification. *Elektronika ir Elektrotechnika*, *27*(1), 48–59. https://doi.org/10.5755/j02.eie.27642

Nguyen, T., Qin, X., Dinh, A., & Bui, F. (2019). Low Resource Complexity R-peak Detection Based on Triangle Template Matching and Moving Average Filter. *Sensors*, *19*(18), 3997–4014. https://doi.org/10.3390/s19183997

Olanrewaju, R. F., Ibrahim, S. N., Asnawi, A. L., & Altaf, H. (2021). Classification of ECG signals for detection of arrhythmia and congestive heart failure based on continuous wavelet transform and deep neural networks. *Indonesian Journal of Electrical Engineering and Computer Science*, *22*(3), 1520–1528. https://doi.org/10.11591/ijeecs.v22.i3.pp1520-1528

Park, J.-S., Lee, S.-W., & Park, U. (2017). R Peak Detection Method Using Wavelet Transform and Modified Shannon Energy Envelope. *J Healthc Eng*, *2017*, 4901017–4901032. https://doi.org/10.1155/2017/4901017

Qin, Q., Li, J., Yue, Y., & Liu, C. (2017). An Adaptive and Time-Efficient ECG R-Peak Detection Algorithm. *J Healthc Eng*, *2017*, 1–14. https://doi.org/10.1155/2017/5980541

Rahman, N. A. A., & Jambek, A. B. (2019). Biomedical health monitoring system design and analysis. *Indonesian Journal of Electrical Engineering and Computer Science*, *13*(3), 1056–1064. https://doi.org/10.11591/ijeecs.v13.i3.pp1056-1064

Ribeiro, A. H., Ribeiro, M. H., Paixão, G. M. M., Oliveira, D. M., Gomes, P. R., Canazart, J. A., Ferreira, M. P. S., Andersson, C. R., Macfarlane, P. W., Meira, W. Jr., Schön, T. B., & Ribeiro, A. L. P. (2020). Automatic diagnosis of the 12-lead ECG using a deep neural network. *Nature Communications*, *11*(1), 1760–1769. https://doi.org/10.1038/s41467-020-15432-4

Sharma, L. D., & Sunkaria, R. K. (2016). A robust QRS detection using novel pre-processing techniques and kurtosis based enhanced efficiency. *Measurement*, *87*, 194–204. https://doi.org/10.1016/j.measurement.2016.03.015

Suboh, M. Z., Jaafar, R., Nayan, N. A., & Harun, N. H. (2020). Shannon Energy Application for Detection of ECG R-peak using Bandpass Filter and Stockwell Transform Methods. *Advances in Electrical and Computer Engineering*, *20*(3), 41–48. https://doi.org/10.4316/AECE.2020.03005

Wu, M., Lu, Y., Yang, W., & Wong, S. Y. (2021). A Study on Arrhythmia via ECG Signal Classification Using the Convolutional Neural Network [Original Research]. *Frontiers in Computational Neuroscience*, *14*, 1–10. https://doi.org/10.3389/fncom.2020.564015

Xiang, Y., Lin, Z., & Meng, J. (2018). Automatic QRS complex detection using two-level convolutional neural network. *BioMedical Engineering OnLine*, *17*(1), 13. https://doi.org/10.1186/s12938-018-0441-4

Zahid, M. U., Kiranyaz, S., Ince, T., Devecioglu, O. C., Chowdhury, M. E. H., Khandakar, A., Tahir, A., & Gabbouj, M. (2021). Robust R-Peak Detection in Low-Quality Holter ECGs using 1D Convolutional Neural Network. *IEEE Transactions on Biomedical Engineering*, *69*(1), 119–128. https://doi.org/10.1109/TBME.2021.3088218

Zalabarria, U., Irigoyen, E., Martinez, R., & Lowe, A. (2020). Online robust R-peaks detection in noisy electrocardiograms using a novel iterative smart processing algorithm. *Applied Mathematics and Computation*, *369*, 124839–124852. https://doi.org/10.1016/j.amc.2019.124839

Zhang, Z., Li, Z., & Li, Z. (2020). An Improved Real-Time R-Wave Detection Efficient Algorithm in Exercise ECG Signal Analysis. *J Healthc Eng*, *2020*, 8868685. https://doi.org/10.1155/2020/8868685

Zhou, P., Schwerin, B., Lauder, B., & So, S. (2020). Deep Learning for Real-time ECG R-peak Prediction. *2020 14th International Conference on Signal Processing and Communication Systems (ICSPCS)*. IEEE.

Applied Computer Science, vol. 18, no. 3, pp. 31–41
doi: 10.35784/acs-2022-19

Submitted: 2022-07-22 | Revised: 2022-09-01 | Accepted: 2022-09-23

Keywords: cavitation, CFD, fluid flow, hydrodynamics, orifice, simulation

Konrad PIETRYKOWSKI [0000-0001-6497-7572]*,
Paweł KARPIŃSKI [0000-0001-5786-1248]*

SIMULATION STUDY OF HYDRODYNAMIC CAVITATION IN THE ORIFICE FLOW

Abstract

Hydrodynamic cavitation is a phenomenon that can be used in the water treatment process. For this purpose, venturis or orifices varying in geometry are used. Studying this phenomenon under experimental conditions is challenging due to its high dynamics and difficulties in measuring and observing the phase transition of the liquid. For this reason, the CFD method was used to study the phenomenon of hydrodynamic cavitation occurring in water flow through the orifice and then analyze flow parameters for different boundary conditions. The research was performed for four different orifice geometries and two defined fluid pressure values at the inlet, based on a computational 2D model of the research object created in Ansys Fluent software. As a result of the numerical simulation, the distribution of fluid velocity and pressure and volume fraction of the gas phase were obtained. A qualitative and quantitative analysis of the phenomenon of hydrodynamic cavitation under the considered flow conditions was conducted for the defined orifice geometries. The largest cavitation zone and thus the largest volume fraction of the gas phase was obtained for the orifice diameter of 2 mm with a sharp increase in diameter. However, the geometry with a linear change in diameter provided the largest volume fraction of the gas phase per power unit.

1. INTRODUCTION

The phenomenon of cavitation is a rapid phase transition of the fluid from the liquid to gaseous phase due to a decrease in pressure. According to the principle of energy conservation in hydrodynamics (Bernoulli's law), if the velocity of the fluid increases, then the static pressure decreases. Cavitation occurs if the static pressure of the fluid below the saturated vapor pressure is reduced and then increased above this limit. Then the evaporation and formation of gas bubbles will occur, followed by their implosion. Bubble behavior formed during cavitation was studied (Moholkar & Pandit, 1997) and it was observed that the behavior of gas bubbles changes drastically under turbulent flow conditions. Numerical studies (Gogate & Pandit, 2000) showed that bubble dynamics, and thus the pressure created when bubbles collapse, depends on parameters such as the inlet pressure through the orifice system, the initial size of the cavity and the diameter of the orifice which affects the frequency of turbulence in the reactor.

* Lublin University of Technology, Faculty of Mechanical Engineering, Department of Thermodynamics, Fluid Mechanics, and Aircraft Propulsion Systems, Lublin, Poland, wm.ktmp@pollub.pl

Cavitation is a phenomenon that can be used in various industrial applications involving physical or chemical transformations. This phenomenon can form hydrodynamic, acoustic, optical, and particle cavitation (Gogate, Tayal & Pandit, 2006). Cavitation can improve the biological oxidation of natural municipal and industrial wastewater (Gogate, Thanekar & Oke, 2020). Orifices or venturi with different geometries can be used to generate hydrodynamic cavitation. Orifices in the form of a venturi can vary in length and diameter.

Hydrodynamic cavitation finds particular application in industrial water treatment processes. Moreover, their number and distribution on the cavitation inducer disc can vary. This phenomenon makes it possible to remove various chemical pollutants, for example, ammoniacal nitrogen (Patil, Bhandari & Ranade, 2021). Scientific papers on hydrodynamic cavitation for wastewater treatment (Wang, Su & Zhang, 2021) and the oxidation of organic compounds contained in industrial wastewater (Gągol, Przyjazny & Boczkaj, 2018) were reviewed in detail. For the analysis of processes using the phenomenon of cavitation, models linking the dynamics of the bubbles formed to chemical reactions play an essential role (Tao et al., 2016). An example of such a model is the hydrodynamic cavitation model, including radical hydroxyl production (Capocelli et al., 2014).

The cavitation phenomenon in Venturi tubes was studied (Shi et al., 2019). The experimental results were compared with the simulation calculations of venturis with the convergence angles of 19 and 45 degrees, respectively. The results showed that changing the convergence angle significantly affects flow characteristics and cavitation generation. It was shown that a 45-degree convergence angle enhances cavitation compared to the smaller angle tested. The results developed a semi-empirical model to predict cavitation in venturis.

Cavitation flows are associated with phase transitions resulting in significant and rapid density changes in low-pressure regions (Singhal et al., 2002). In addition, this type of flow is sensitive to the formation and transport of vapor bubbles and turbulent velocity and pressure fluctuations. These aspects were included in the cavitation model developed by Singhal. The phase-change rate was considered in terms of rates derived from a reduced form of the Rayleigh-Plesset equation for bubble dynamics. In general, this equation is a differential equation that allows for the calculation of bubble radius as a function of fluid pressure change (Franc, 2006). A cavitation model based on the multi-phase flow equations was developed (Zwart, Gerber & Belamri, 2004) and validated by testing flow through a venturi.

The study of cavitation flow under experimental conditions can be complex due to the high dynamics of accompanying phenomena and the associated difficulties in measuring and observing fluid phase transitions so computational fluid mechanics (CFD) is used to study such issues. This method makes it possible to analyze flow parameters for various boundary conditions. Its great advantage is the low cost of conducting research and performing a series of calculations in a short time compared to empirical studies.

Cavitation is often studied for industrial applications such as injectors, propellers, and water pumps. The simulation study of the cavitation phenomenon in a model water pump (Ding et al., 2011) shows that the predicted pump performance and cavitation characteristics obtained from the CFD method matched well with the experimental results. For CFD calculations, there may be certain difficulties in multi-phase and cavitation models. In the case of a simulation study of cavitation in a positive displacement pump, the calculated evaporation/condensation rate and the fundamental dynamics of the phenomenon may be inconsistent due to an inaccurate calculation of the expansion of non-condensable gas (Iannetti, Stickland & Dempster, 2016). The CFD method was also used to model the flow of submerged bodies subjected to natural and ventilated cavitation (Kunz et al., 1999). The CFD method can also study cavitation resulting from propeller flow (Subhas et al., 2012). Various computational solvers such as RANS, LES, and BEM can be used to study propeller cavitation modeling (Salvatore, Streckwall & Van Terwisga, 2009). Studies showed that mesh resolution in the cavitation flow region and numerical dispersion is essential for predicting the range and dynamics of cavitation.

A dimensionless parameter for evaluating cavitation is the cavitation number. This parameter can be determined for any flow although the cavitation phenomenon does not always have to occur. The value of the cavitation number corresponding to the first occurrence of cavitation at a given inlet pressure is referred to as the cavitation inception number (Brennen, 1994). Cavitation initiation is sensitive to nozzle geometry changes (Omelyanyuk, 2022). As noted, geometric parameters are not included in the cavitation number formula so cavitation initiation can occur differently with the same cavitation number. The analyses performed were based on CFD calculations compared with experimental results.

This work discusses a simulation study of hydrodynamic cavitation in fluid flow through four orifices with varied geometries for two defined fluid pressure values at the inlet. For this purpose, a computational 2D model was developed in Ansys Fluent software and its assumptions are presented in Section 2. As a result of numerical calculations, the distribution of fluid velocity and pressure and volume fraction of the gas phase were obtained and underwent quantitative and qualitative analysis. The results and analysis are presented in Section 3. Finally, Section 4 summarizes the research and considerations on the cavitation phenomenon.

2. METHOD AND RESEARCH OBJECT

The phenomenon of hydrodynamic cavitation resulting from water flow through four orifices with different geometries was analyzed numerically (Fig. 1). The first of the geometries, marked as A, was characterized by a single diameter. The orifice channel of a diameter of 1 mm and a length of 5 mm was straight and its origin was at a distance of 10 mm from the inlet surface. The overall length of the computational domain was 25 mm. The second geometry, designated B, had a larger diameter of 2 mm. The following orifice geometries had a gradually increasing diameter. In geometry C, the initial diameter of 1 mm and a length of 1.5 mm increased to 1.5 mm. In geometry D, the change in diameter was sharp and its value changed from 2 to 2.5 mm. The change occurred at a distance of 1 mm from the edge of the inlet. The overall lengths of the orifices and the computational domain were the same in all cases considered. A 2D model was analyzed due to its axisymmetric design. This approach significantly reduces the time of numerical calculations without affecting the results.

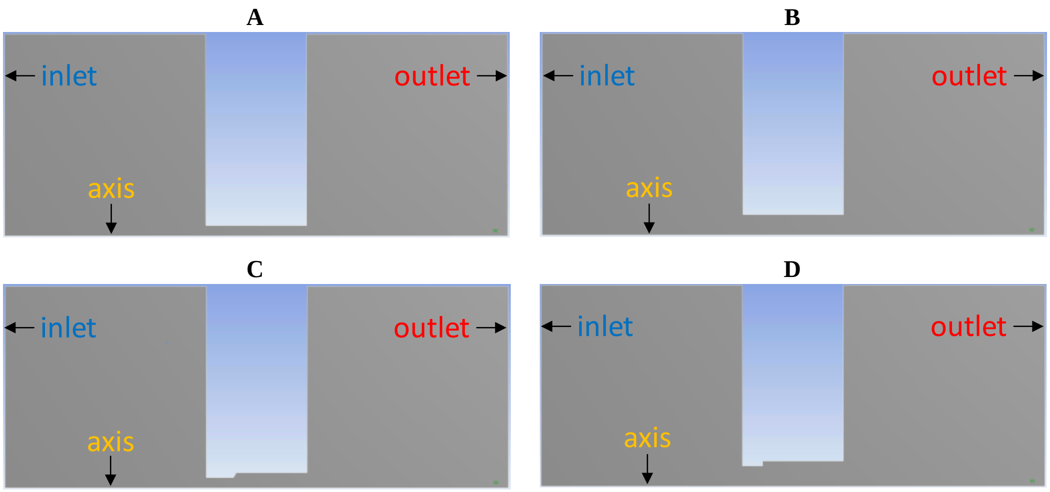

Fig. 1. Geometric models of the studied orifices

The 2D model was developed for the considered orifice geometries to analyze flow parameters in Ansys Fluent software. The computational meshes of 16 095, 17 000, 17 404, and 17 047 cells were generated, respectively. The cells were quadrilateral and triangular and ranged from 0.1 to 0.2 mm. Within a radius of 2.5 mm from the edge of the hole inlet, the cells were concentrated at 0.06 mm. In addition, a wall layer composed of ten 0.5 mm thick layers with a growth rate of 1.2 was created on the wall of the modeled orifice. Fig. 2 shows the generated meshes.

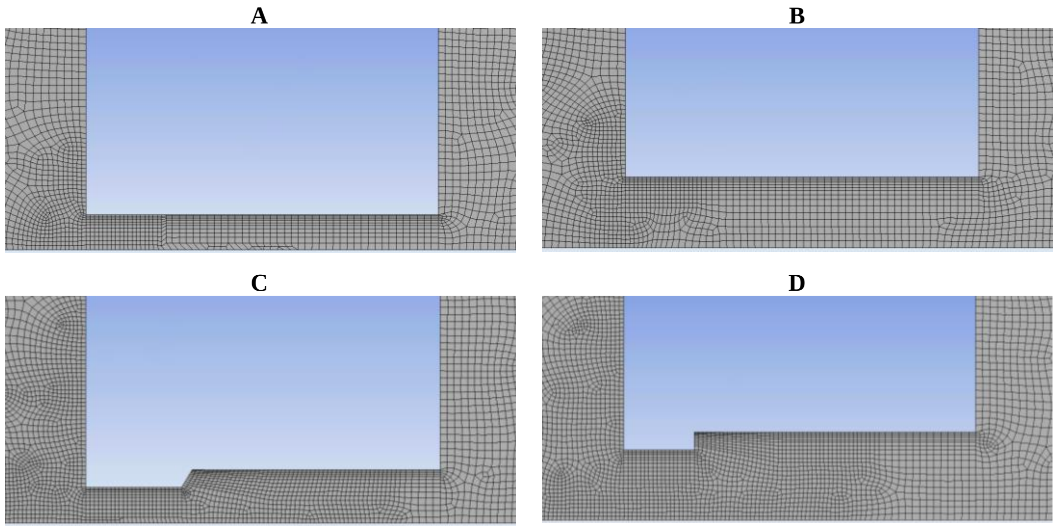

Fig. 2. Generated computational meshes for the tested orifice geometries

A mixture-type multi-phase model was used to simulate the cavitation process and two phases, i.e. liquid water and gaseous water were defined. The Schnerr-Sauer cavitation model was chosen, and a cavitation pressure of 3 540 Pa was set. This pressure value represents the pressure of saturated vapor at 300 K. In addition, the model assumed a constant density of the liquid phase of 998.2 kg/m^3 and the gas phase of 0.8 kg/m^3. This is necessary due to the difficulty of achieving convergence of calculations when compressibility of the gas phase is assumed. The model includes the gas phase, the liquid phase, and the processes of evaporation and condensation of the liquid (Zheng et al., 2018). The model uses the Volume-of-Fluid method (VOF) which is used to predict the growth and collapse of resulting bubble clouds (Sauer & Schnerr, 2001; Schnerr & Sauer, 2001). The k-ω SST model was adopted as the turbulence model. This k-ω model represents the turbulent flow in the near-wall layer well and remains sensitive to the amount of turbulence in the free flow. Therefore, a shear stress transport (SST) model was used, which allows transition to the k-ε model in the free flow while modeling the boundary layer using k-ω. The turbulence model includes kinetic energy k and turbulence-specific dissipation rate ω (Menter, 1993; Menter, 1994). A correct modeling of the near-wall layer is desirable because the cavitation phenomenon occurs exactly in this flow zone. The boundary conditions were inlet pressures of 700 kPa and 1 000 kPa and outlet pressure of 100 kPa. The calculations were performed until convergence equivalent to a maximum residuals level of $1 \cdot 10^{-5}$.

3. RESULTS AND DISCUSSION

Numerical calculations made it possible to obtain velocity, pressure, and volume fraction distributions of the gas phase for four considered orifice geometries for the two defined inlet pressures: 700 kPa and 1 000 kPa. The adopted pressure values result from the conclusions drawn from preliminary tests of the developed water treatment system. On the one hand, the maximum pressure value is limited due to the high energy consumption of the system, but on the other hand, the minimum value stems from the satisfactory treatment results obtained at this pressure value.

The first parameter analyzed was velocity distribution. The results in the form of streamlines for the considered orifice geometries and inlet pressures are shown in Fig. 3 and Fig. 4. The colors of the streamlines show the flow velocity in the model. For the lower pressure value, the maximum velocity value was about 37 m/s, while for the higher pressure value, it was about 45 m/s. In all cases considered, the highest velocity occurred in the core of the flow. Its value decreased gradually as it approached the walls due to fluid viscosity. In the case of the simple orifice geometries (A and B), little turbulence combined with the deceleration of the liquid near the orifice wall was observed. This phenomenon began just behind the orifice inlet which is also the starting point of the essential phase of hydrodynamic cavitation. The lowest velocity results from the formation of the gas phase with the chaotic movement of molecules that, in turn, significantly reduces velocity due to the resulting turbulent flow.

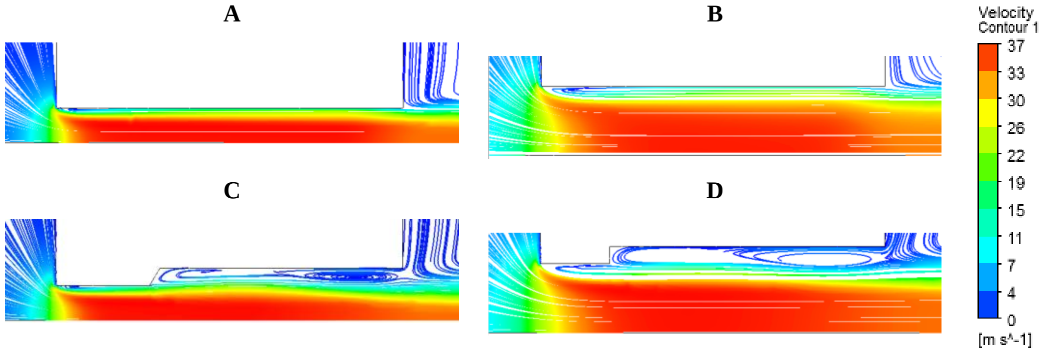

Fig. 3. Distribution of the fluid velocity for the tested orifices for the inlet pressure of 700 kPa

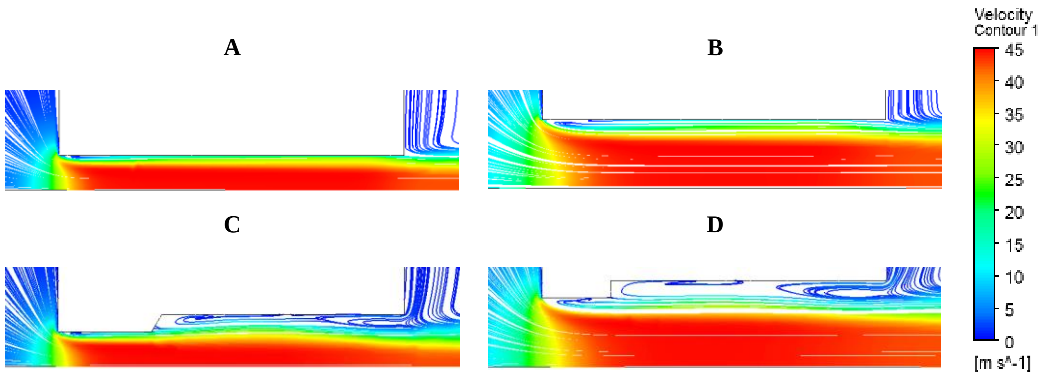

Fig. 4. Distribution of the fluid velocity for the tested orifices for the inlet pressure of 1 000 kPa

The other of the analyzed parameters was pressure distribution. The results for the studied orifices and pressures are shown in Fig. 5 and Fig. 6. According to Bernoulli's law and the continuity equation for fluid flow, the pressure value decreased due to the narrowing of the channel the fluid flows through. The local pressure drop was so significant that the static pressure value fell below the defined saturated vapor pressure, i.e. 3 570 Pa, and the phenomenon of hydrodynamic cavitation occured. For all geometries considered, the lowest pressure value (below the saturated vapor pressure) was obtained just behind the inlet edge in the near-wall layer zone. For geometry C, the area of the lowest pressure also occurred in the near-wall layer near the orifice diameter change. For the higher inlet pressure (1 000 kPa), the area of the lowest pressure was slightly larger than that of the lower inlet pressure (700 kPa). The pressure distribution in the flow core near the orifice inlet was approximately parabolic.

The last distribution analyzed was the volume fraction of the gas phase. The values of this parameter for the inlet pressures of 700 and 1 000 kPa and the tested geometries are shown in Fig. 7 and Fig. 8. In the case of the straight channels (orifice A and B), the zone of occurrence of the gas phase started just behind the inlet edge of the orifice and had the form of a near-wall layer. The diameter of the orifice increased due to the slight increase in the thickness of this layer. The varying cross-section of the orifice significantly increased the size of the zone where the gas phase occurs. The increasing diameter slightly increased its size. A similar effect was caused by the increased inlet pressure value.

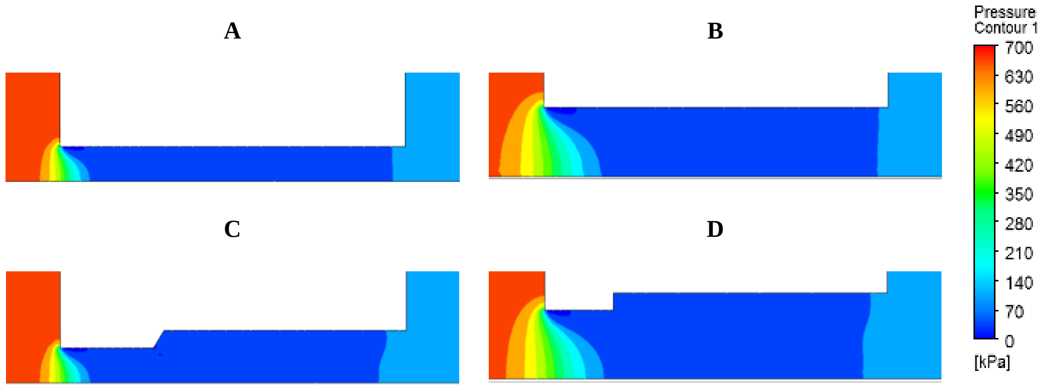

Fig. 5. Distribution of the fluid pressure for the tested orifices for the inlet pressure of 700 kPa

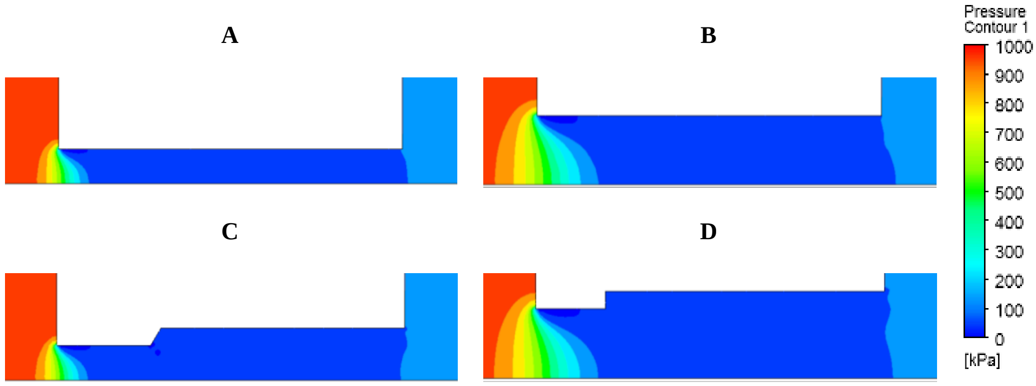

Fig. 6. Distribution of the fluid pressure for the tested orifices for the inlet pressure of 1 000 kPa

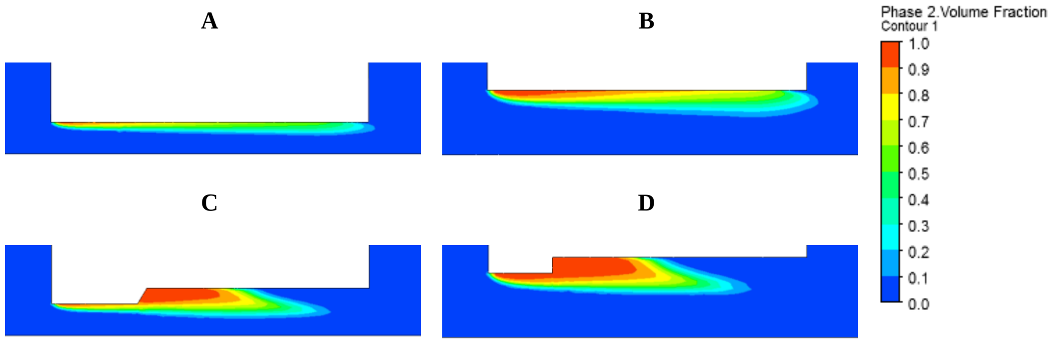

Fig. 7. Distribution of the volume fraction of the gas phase for the tested orifices for the inlet pressure of 700 kPa

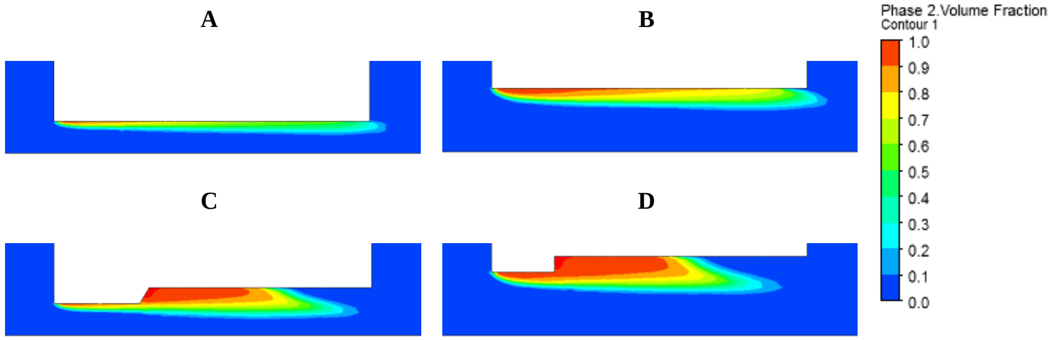

Fig. 8. Distribution of the volume fraction of the gas phase for the tested orifices for the inlet pressure of 1 000 kPa

The total volume fraction of the gas phase was further analyzed for the defined orifice geometries and inlet pressures (Fig. 9). The highest volume fraction was obtained for orifice D with a sharp change in its cross-sectional diameter, while the lowest volume fraction for geometry A with a straight channel of 1 mm diameter. It was also observed that the pressure value slightly affected the analyzed parameter. The most significant difference, i.e. more than 20% was observed for geometry D, while the smallest effect, i.e. 3% difference occurred for geometry A. The results obtained for geometry A may be due to the dominating influence of viscous forces in the fluid, which makes it difficult to change the state. In the case of geometry D, the larger diameter and its sharp increase provide more favorable conditions for cavitation initiation and its further development.

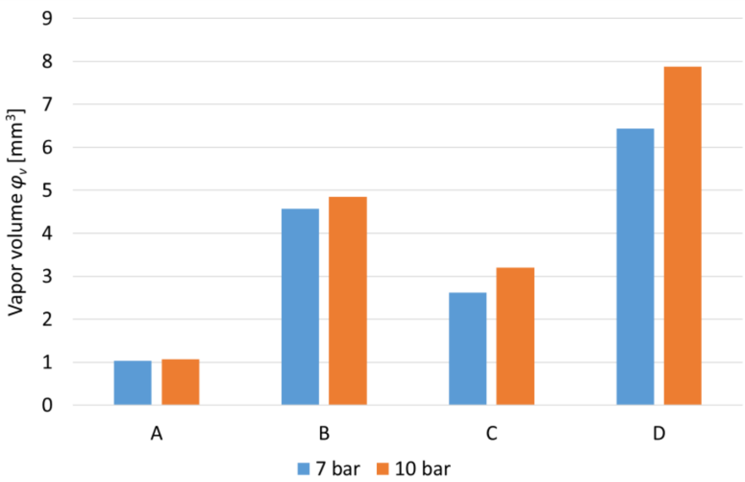

Fig. 9. Vapor volume for the selected orifices and defined inlet pressure values

Eventually, the vapor volume per power unit was calculated for the selected orifices and defined inlet pressure values (Fig. 10). Effective flow power was determined as the product of the vapor volume flow rate and the pressure difference at the inlet and outlet. Although geometry D provides the highest absolute value of vapor volume, considering the energy flow associated with the fluid flow, the highest value of gas phase volume per unit power ($0.24\ mm^3/W$) was obtained for geometry C and the lower pressure value. For the higher pressure, the parameter considered was 32% lower. The least favorable was geometry A, for which the volume fraction of the gas phase per unit power was 63% lower compared to geometry C ($0.09\ mm^3/W$ for 700 kPa).

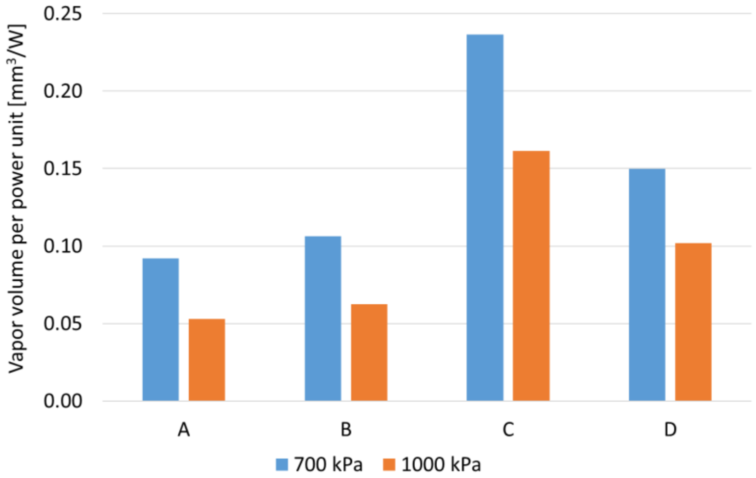

Fig. 10. Vapor volume per power unit for the selected orifices and defined inlet pressure values

4. CONCLUSION

This paper presents the results of a numerical study of the hydrodynamic cavitation phenomenon occurring as water flows through an orifice. Four orifice geometries were studied for two inlet pressure values, and the velocity, pressure, and volume fraction distributions obtained from the CFD simulations were analyzed.

The research made it possible to determine the location and size of the cavitation zone in the orifice cross-section. It was noted that cavitation initiation occurs just behind the inlet edge near the wall. The gas phase then develops as a stream located in the wall layer. This may result from the simultaneous influence of viscosity and turbulence associated with the rapid phase change of the fluid from liquid to gas.

For all geometries considered, the chaotic movement of particles in the wall layer zone generated by the phase transition resulted in a significant reduction in velocity to a value close to zero. For a higher inlet pressure value (1 000 kPa), a higher maximum flow velocity through the orifice was obtained (an increase of 8 m/s). This value occurred in the flow core at the axis of symmetry.

The lowest pressure value below the saturated vapor pressure occurred just behind the inlet edge in the near-wall layer zone for all the orifice geometries considered. This shows that the cavitation phenomenon (phase transition) started at the same spot regardless of the geometry. In the case of geometry C, the additional area with the lowest pressure occurred in the near-wall layer zone where the diameter changes, which means that the pressure drops due to flow acceleration resulting from the local change in geometry were large enough to exceed the saturated vapor pressure.

Using geometries with variable orifice diameters (C and D) resulted in a larger gas phase area. The most significant volume fraction of the gas phase in the considered computational domain was obtained for geometry D – a larger diameter orifice with its sharp increase. The smallest fraction was obtained for the straight orifice with a diameter of 1 mm (geometry A). The value of inlet pressure did not significantly affect the velocity near the cavitation zone. For the analyzed orifice geometries, a slightly higher volume fraction of the gas phase was obtained for the higher inlet pressure, with the largest difference (more than 20%) observed for geometry D. The largest value of the volume fraction of the gas phase per unit power was obtained for geometry C and the lower pressure value. This parameter was equal to 0.24 mm^3/W. The least favorable was geometry A for which this parameter was by 63% smaller than for geometry C.

The study allowed for a quantitative and qualitative evaluation of hydrodynamic cavitation in the tested orifice geometries. The orifice geometry with a diameter of 2 mm with a sharp increase in diameter (type D) generates the largest cavitation zone, and thus the largest volume fraction of the gas phase. This fact may result in a proportional increase in free radicals which will further react with substances in contaminated water. The results obtained enable further experimental studies to evaluate the efficiency of the wastewater treatment process.

Funding

The publication was financed by the Polish National Centre for Research and Development (grant agreement no. POIR.04.01.04-00-0057/20).

Acknowledgments

The work was performed within the framework of a project financed by the Polish National Centre for Research and Development (grant agreement no. POIR.04.01.04-00-0057/20).

Conflicts of Interest

The authors declare no conflict of interest.

REFERENCES

Brennen, C. E. (2011). *Hydrodynamics of pumps*. Cambridge University Press.

Capocelli, M., Musmarra, D., Prisciandaro, M., & Lancia, A. (2014). Chemical effect of hydrodynamic cavitation: simulation and experimental comparison. *AIChE Journal*, *60*(7), 2566–2572. https://doi.org/10.1002/aic.14472

Ding, H., Visser, F. C., Jiang, Y., & Furmanczyk, M. (2011). Demonstration and validation of a 3D CFD simulation tool predicting pump performance and cavitation for industrial applications. *Journal of fluids engineering*, *133*(1), 011101. https://doi.org/10.1115/1.4003196

Franc, J. P. (2006). *Physics and control of cavitation*. Grenoble Univ (France).

Gągol, M., Przyjazny, A., & Boczkaj, G. (2018). Wastewater treatment by means of advanced oxidation processes based on cavitation–a review. *Chemical Engineering Journal*, *338*, 599–627. https://doi.org/10.1016/j.cej.2018.01.049

Gogate, P. R., & Pandit, A. B. (2000). Engineering design methods for cavitation reactors II: hydrodynamic cavitation. *AIChE Journal*, *46*(8), 1641–1649. https://doi.org/10.1002/aic.690460815

Gogate, P. R., Tayal, R. K., & Pandit, A. B. (2006). Cavitation: a technology on the horizon. *Current science*, *91*(1), 35–46.

Gogate, P. R., Thanekar, P. D., & Oke, A. P. (2020). Strategies to improve biological oxidation of real wastewater using cavitation based pre-treatment approaches. *Ultrasonics Sonochemistry*, *64*, 105016. https://doi.org/10.1016/j.ultsonch.2020.105016

Iannetti, A., Stickland, M. T., & Dempster, W. M. (2016). A CFD and experimental study on cavitation in positive displacement pumps: Benefits and drawbacks of the 'full'cavitation model. *Engineering Applications of Computational Fluid Mechanics*, *10*(1), 57–71. https://doi.org/10.1080/19942060.2015.1110535

Kunz, R. F., Boger, D. A., Chyczewski, T. S., Stinebring, D., Gibeling, H., & Govindan, T. (1999). Multi-phase CFD analysis of natural and ventilated cavitation about submerged bodies. In *Proceedings of the 3rd ASME-JSME Joint Fluids Engineering Conference*. American Society of Mechanical Engineers.

Menter, F. (1993). Zonal two equation kw turbulence models for aerodynamic flows. In *23rd fluid dynamics, plasmadynamics, and lasers conference* (p. 2906).

Menter, F. R. (1994). Two-equation eddy-viscosity turbulence models for engineering applications. *AIAA journal*, *32*(8), 1598–1605.

Moholkar, V. S., & Pandit, A. B. (1997). Bubble behavior in hydrodynamic cavitation: effect of turbulence. *AIChE Journal*, *43*(6), 1641–1648.

Omelyanyuk, M., Ukolov, A., Pakhlyan, I., Bukharin, N., & El Hassan, M. (2022). Experimental and Numerical Study of Cavitation Number Limitations for Hydrodynamic Cavitation Inception Prediction. *Fluids*, *7*(6), 198. https://doi.org/10.3390/fluids7060198

Patil, P. B., Bhandari, V. M., & Ranade, V. V. (2021). Improving efficiency for removal of ammoniacal nitrogen from wastewaters using hydrodynamic cavitation. *Ultrasonics Sonochemistry*, *70*, 105306. https://doi.org/10.1016/j.ultsonch.2020.105306

Salvatore, F., Streckwall, H., & Van Terwisga, T. (2009). Propeller cavitation modelling by CFD-results from the VIRTUE 2008 Rome workshop. In *Proceedings of the first international symposium on marine propulsors, Trondheim, Norway* (pp. 22–24).

Sauer, J., & Schnerr, G. H. (2001). Development of a new cavitation model based on bubble dynamics. *ZAMM-Journal of Applied Mathematics and Mechanics/Zeitschrift für Angewandte Mathematik und Mechanik*, 81(S3 S3), 561–562. https://doi.org/10.1002/zamm.20010811559

Schnerr, G. H., & Sauer, J. (2001). Physical and numerical modeling of unsteady cavitation dynamics. In *Fourth international conference on multi-phase flow* (Vol. 1). ICMF New Orleans.

Shi, H., Li, M., Nikrityuk, P., & Liu, Q. (2019). Experimental and numerical study of cavitation flows in venturi tubes: From CFD to an empirical model. *Chemical Engineering Science*, *207*, 672–687.

Singhal, A. K., Athavale, M. M., Li, H., & Jiang, Y. (2002). Mathematical basis and validation of the full cavitation model. *J. Fluids Eng.*, *124*(3), 617–624. https://doi.org/10.1115/1.1486223

Subhas, S., Saji, V. F., Ramakrishna, S., & Das, H. N. (2012). CFD analysis of a propeller flow and cavitation. *International Journal of Computer Applications*, *55*(16), 26–33.

Tao, Y., Cai, J., Huai, X., Liu, B., & Guo, Z. (2016). Application of hydrodynamic cavitation to wastewater treatment. *Chemical engineering & technology*, *39*(8), 1363–1376. https://doi.org/10.1002/ceat.201500362

Wang, B., Su, H., & Zhang, B. (2021). Hydrodynamic cavitation as a promising route for wastewater treatment–A review. *Chemical Engineering Journal*, *412*, 128685. https://doi.org/10.1016/j.cej.2021.128685

Zheng, X. B., Liu, L. L., Guo, P. C., Hong, F., & Luo, X. Q. (2018, July). Improved Schnerr-Sauer cavitation model for unsteady cavitating flow on NACA66. *IOP Conference Series: Earth and Environmental Science*, *163*(1), 012020).

Zwart, P. J., Gerber, A. G., & Belamri, T. (2004, May). A two-phase flow model for predicting cavitation dynamics. In *Fifth international conference on multi-phase flow, Yokohama, Japan* (No. 152).

Applied Computer Science, vol. 18, no. 3, pp. 42–53
doi: 10.35784/acs-2022-20

Submitted: 2022-05-06 | Revised: 2022-06-14 | Accepted: 2022-06-17

Keywords: FEM, parallel computing, dieless drawing, thin wire

Andrij MILENIN [0000-0002-6266-2881]*

PARALLEL SOLUTION OF THERMOMECHANICAL INVERSE PROBLEMS FOR LASER DIELESS DRAWING OF ULTRA-THIN WIRE

Abstract

The paper discusses the solving of inverse thermomechanical problems requiring a large number of FEM tasks with various boundary conditions. The study examined the case when all tasks have the same number of nodes, finite elements, and nodal connections. In this study, the speedup of the solution of the inverse problem is achieved in two ways: 1. The solution of all FEM tasks in parallel mode. 2. The use by all FEM tasks a common matrix with addresses of nonzero elements in the stiffness matrices. These algorithms are implemented in the own FEM code, designed to solve inverse problems of the hot metal forming. The calculations showed that developed code in parallel mode is effective for the number of tasks late than 0,7-0,9 of the number of available processors. Thus, at some point, it becomes effective to use a sequential solution to all tasks and to use a common matrix of addresses of nonzero elements in the stiffness matrix. The achieved acceleration at the optimal choice of the algorithm is 2–10 times compared with the classical multivariate calculations in the FEM. The paper provides an example of the practical application of the developed code for calculating the allowable processing maps for laser dieless drawing of ultra-thin wire from copper alloy by solving the thermomechanical inverse problem. The achieved acceleration made it possible to use the developed parallel code in the control software of the laboratory setup for laser dieless drawing.

1. INTRODUCTION

Inverse thermomechanical problems arise when the subject of analysis is both the mechanical behavior of the material (Kubo, 1988) and the temperature distribution (Jaluria, 2021). Such problems are often encountered in technical applications of theories of elasticity, fluid mechanics, plasticity, and heat transfer (Lesnic, 2021). A rather difficult version of these problems is associated with the hot metal forming (Chenot, Massoni & Fourment, 1996). In this case, the direct problem contains the coupled problems of unsteady-state heat transfer and deformation of an incompressible viscoplastic material. One of the well-known inverse problems in practice is to determine the parameters of a material model based on indirect experimental data. For example, in the paper (Szeliga & Pietrzyk, 2007) the problem of determining the flow stress model of microalloyed niobium steel was considered.

* AGH University of Science and Technology, Faculty of Metals Engineering and Industrial Computer Science, Department of Applied Computer Science and Modelling, Krakow, Poland, milenin@agh.edu.pl

As the objective function, the square of the difference between the experimental results (for example, the compression force in the plastometric test) and the FEM calculation is used. As shown in (Szeliga, Gawąd & Pietrzyk, 2004), the optimization method is essential. This is because the inverse analysis requires a large number of similar FEM tasks, especially when identifying complex materials (Pokorska, 2007). Another type of inverse problems is associated with the determination of process parameters that lead to a given result – for example, to the necessary metal forming (Thomas et al., 2017). An interesting example in this sense is the relatively new process of laser dieless drawing of thin wire. The process of laser dieless drawing is a stretching of a wire with its simultaneous local heating in the deformation zone by a laser beam (Li, Quick & Kar, 2002). This process differs significantly from the conventional wire drawing. The conventional process is based on a drawing in dies with diamond cores. The use of a die significantly increases the cost of the process. Also, conventional wire drawing requires the use of some lubricants, and their chemical removal from the final wire degrades the surface quality and is not harmless to the natural environment. Thus, conventional technology is quite expensive (Kraft, 1980). On the other hand, in laser dieless drawing, the prediction of such parameters as the final wire diameter, strain, or temperature of the deformation requires complex FEM calculations. It is important to note that because of the asymmetry of laser heating, the boundary value problem becomes three-dimensional. For this reason, the existing axisymmetric FEM solutions for typical dieless drawing process with electrical or induction heating (for example (Furushima & Manabe, 2007) or (Tiernan & Hillery, 2004)) cannot be applied.

In the dieless drawing process, the diameter of the wire is formed freely and is not determined by the shape of the die, in contrast to conventional wire drawing (Tiernan & Hillery, 2008). Thus, to determine the laser dieless drawing parameters leading to the production of a wire of a given diameter, the inverse problem must be solved. Furthermore, from this point of view, solving the individual direct problem for this process is usually not of practical interest. This is the first important feature of this process. The second feature of the laser dieless drawing of thin wire is the practical need to obtain a map of allowable process parameters. To compile such a map, it is necessary not only to find the one optimal solution but also to solve the vector of direct problems. Solving the inverse problem in such a formulation requires a significant speedup of the numerical solution by optimizing the FEM code. The third feature of the process is that all FEM tasks have the same number of nodes, finite elements, and same nodal connections (in this process is not necessary of remeshing of FEM grid during the calculation). This means that the position of nonzero elements in the stiffness matrix is the same for all tasks, solved in the process of inverse analysis. Thus, considering the solution of the inverse problem as the main mode of operation of the developed FEM code, the address matrix of nonzero elements of the stiffness matrices (thermal and mechanical) can be determined once and used by all FEM tasks during the inverse analysis.

The second way to speed up the solution of the inverse problem is to use parallel computing. The idea of using parallel computing to solve inverse problems was applied earlier, for example, in (Milenin, 2017) to analyze tube production by laser dieless drawing. A comparison of the results of the calculation of temperature and strain with experimental data showed their good agreement (Milenin et al., 2018). However, these findings cannot be extrapolated directly to laser drawing of thin wire because in this process the FEM grid and stiffness matrices had a different structure. On the other side, recent research (Milenin, Wróbel & Kustra, 2022) has suggested that during the production of thin wire by dieless drawing the use of such FEM code for analysis and optimizing the production parameters is much more important, since experimental control of the temperature and deformation of a wire with a diameter of several tens of micrometers is very difficult.

Thus, in this paper, the FEM code for solving inverse problems based on the use of both a general address matrix of nonzero elements of stiffness matrices and parallel computations is proposed for laser dieless drawing of thin wire. The paper also investigates the numerical efficiency of the developed code using the example of the laser dieless drawing problem of a thin wire made of CuZn37 alloy. The paper also proposes a practical solution to the inverse problem in the form of an allowable processing map.

2. FEM MODEL OF THE LASER DIELESS DRAWING PROCESS OF WIRE

2.1. Description of the laser dieless drawing process of thin wire

The process of elongation of the wire during the laser dieless drawing takes place in a small volume of material heated by a laser beam with a diameter of 0.4 mm. In Fig. 1 this corresponds to the intersection of beam 4 with wire 1. The rollers of the drawing machine rotate at different speeds, with $V_1 > V_0$. The larger the value of $\Delta V = V_1 - V_0$, corresponding to the greater elongation of the wire. However, a too large ΔV value will lead to wire breakage. The deformation temperature also depends on the velocities V_1, V_0. The higher velocities, the shorter the heating time of the wire and the lower the deformation temperature. Since the laser heats the wire only on one side, the task is three-dimensional. Only the part of the wire that is near the heating zone is considered during FEM simulation.

a) **b)**

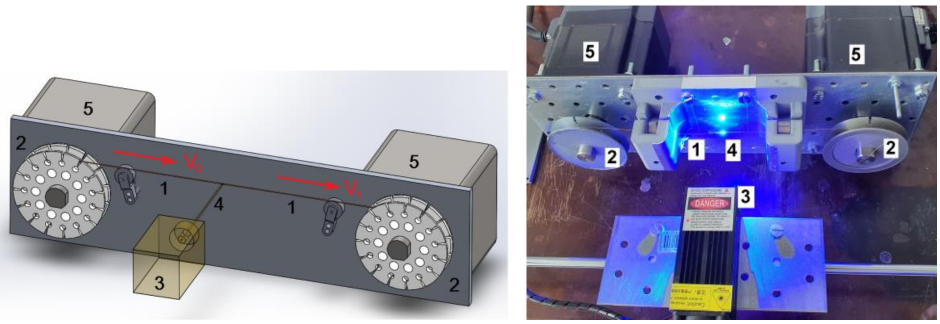

Fig. 1. Scheme (a) and the corresponded setup (b) of the simulated process: 1 – wire; 2 – rollers; 3 – laser; 4 – laser beam; 5 – engines

2.2. FEM model

The boundary problem is described by the equations of the theory of plasticity for non-compressible materials and the equation of non-steady-state heat exchange. In this model the flow velocities v_i, the mean stress σ_0 and temperature *t* is unknown. Thus, the developed FEM code contains the solution of the following group of equations:

– equilibrium equations:

$$\sigma_{ij,i} = 0, \tag{1}$$

– compatibility condition:

$$\dot{\varepsilon}_{ij} = \frac{1}{2}\left(v_{i,j} + v_{j,i}\right), \tag{2}$$

– constitutive equations:

$$\sigma_{ij} = \delta_{ij}\sigma_0 + \frac{2\sigma}{3\dot{\varepsilon}}\dot{\varepsilon}_{ij}, \tag{3}$$

– incompressibility equation:

$$v_{i,j} = 0, \tag{4}$$

– equation of non-steady state heat exchange:

$$\rho c\dot{t} = div\big(k\ grad(t)\big) + \beta\sigma\dot{\varepsilon}, \tag{5}$$

– and model for flow stress:

$$\sigma = \sigma(\varepsilon, \dot{\varepsilon}, t), \tag{6}$$

where: σ_{ij} – stress tensor,
σ_0 – mean stress,
$\dot{\varepsilon}_{ij}$ – strain rate tensor,
v_i – velocity component,
$\sigma, \varepsilon, \dot{\varepsilon}$ – flow stress, effective strain, and effective strain rate, respectively,
t – temperature,
β – heat generation efficiency which is usually assumed as $\beta = 0.95$,
k – thermal conductivity,
ρ – density,
c – heat capacity.

In equations (1)–(5) summation convention is used.

As a model for flow stress (6) the equation of Hensel-Spittel (Hensel & Spittel, 1978) was used:

$$\sigma = A\ exp(m_1 t)\varepsilon^{m_2}\dot{\varepsilon}^{m_3} exp(m_4/\varepsilon)(1+\varepsilon)^{m_5 t} exp(m_6\varepsilon)\ \dot{\varepsilon}^{m_7 t}\ t^{m_8} \tag{7}$$

Following empirical coefficients A and $m_1 - m_8$ for CuZn37 alloy have been found in the paper (Milenin et al., 2022) as a result of the inverse analysis of the plastometric tests: A = 81259.14, m_1 = −0.004279279, m_2 = 0.09383521, m_3 = −0.03657546, m_4 = = −0.004250721, m_5 = 6.06186E-05, m_6 = −0.4821499, m_7 = 0.000317437, m_8 = −0.596443559.

Equations (1)–(4) were transformed into the discrete form using the virtual work-rate principle and FEM technique resulting in a linear system of algebraic equations. The equation of non-steady-state heat exchange (5) is treated using the Galerkin method.

The mechanical boundary conditions involve moving and tensile of wire along heated zone according to the scheme in Fig. 1. The thermal boundary conditions on the contact of wire with air are described by the convection law:

$$q_{air} = \alpha_{air}(t - t_{\infty}) \tag{8}$$

and for heating zone are presented in the form of heat flux:

$$q_{laser} = A\frac{W}{S} \tag{9}$$

where: W – laser power (5.5 W),
A – absorption coefficient of the laser (0.91),
S – the area of contact between the laser and the wire,
α_{air} – coefficient of convective heat exchange with air (120 W/^{0}C m^2),
t_{∞} – the temperature of the environment (20 ^{0}C).

The 8-nodal 3d isoparametric finite elements were used.

2.3. Properties of matrices (using a shared address matrix)

Consider the properties of the stiffness matrix for a mechanical problem. For the heat capacity matrix for the thermal problem, the conclusions are similar. The global stiffness matrix after assembling is sparse. For the grid chosen as an example (12288 nodes, 9155 elements, 46019 Degree Of Freedom (DOF)) there is 0.14% of the non-zero elements in the global stiffness matrix for the mechanical problem and 0.18% for the thermal problem. A schematic representation of the positions of nonzero elements in the heat capacity matrix and stiffness matrix is presented in Fig. 2, a and Fig. 2, b respectively. For such systems of equations, a solver for sparse matrix should be used. In this study, PARDISO software presented by (Schenk & Gärtner, 2004) was used.

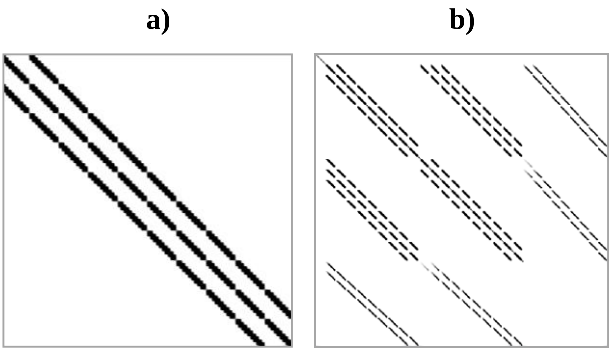

Fig. 2. Graphic representation of heat capacity (a) and stiffness matrices (b); black pixels – nonzero values, white pixels – zero values

For solving systems of equations the following data have to be transmitted to PARDISO solver:

– the number of nonzero elements in the stiffness matrix (*Nonzero*);
– nonzero values in a stiffness matrix (*AK*(*Nonzero*));
– the number of column in the full stiffness matrix containing the nonzero values *JA*(*Nonzero*);
– the beginning of each row *IA*(DOF+1). *IA*(*i*) points to the first column index of row *i* in the array *JA* in compressed sparse row format, *IA*(DOF+1) = *Nonzero* + 1.

The process of solving the system of equations for one time step is relatively fast (is 16 seconds for *DOF* = 46019), but the preparation of the above data requires much more time (is 132 seconds).

One of the key ideas of the proposed solution is to use the fact that for a one task arrays *JA* and *IA* remain constant at every time step. Thus, the task is to find quickly the position of the coefficients of the global stiffness matrix in the linear array *AK*. The proposed solution is to form a service matrix of indexes *IJ*(DOF,DOF) containing an integer number of non-zero elements in *AK* array. For zero elements of the stiffness matrix, *IJ* contains 0. Thus, it is possible to directly fill an array *AK* during assembling the elements. The memory of matrix *IJ*(DOF,DOF) for the described example is more than 8 Gb. This is still a large amount of data, but it is filled once and does not change in the process of the solution. Essential is also the fact that it is possible to use the same copy of the array *IJ* for all tasks solved in the parallel mode. In that case, the proposed solution becomes more efficient both for parallel and sequential solutions of the tasks vector.

2.4. Example of simulation

An example of the simulation result of the direct problem is shown in Fig. 3 and Fig. 4. For this example V_0 = 15 mm/s, V_1 = 20 mm/s. The top image in Fig. 3 corresponds to one of the intermediate stages of the calculation, the bottom – to the last. As follows from the distributions in Fig. 3, the maximum temperature is localized over a very short wire length (about 0.5 mm), which leads to a high strain rate (Fig. 4).

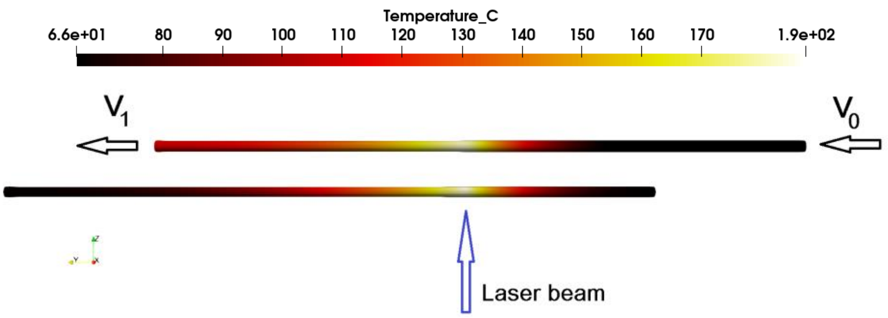

Fig. 3. An example of the result of temperature calculation for the initial (top) and final (down) moment of the simulation

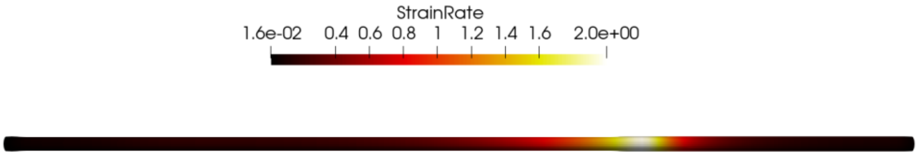

Fig. 4. An example of the result of the strain rate calculation

2.6. Parallelization

The identical numbers of nodes, elements, and same nodal connections for all used FE grids guarantee the same position of non-zero elements in the global stiffness matrix. Therefore, arrays *IA*, *JA*, and *IJ* for all tasks at all stages of the solutions will be the same and can be stored in a single copy. Thus, only the organization of the access to these data to all parallel processes is needed. OpenMP library (Chandra et al., 2001) is used to implement a parallel FEM code. In each parallel task, the sequential algorithm of FEM calculation was used. That's why each task used only one processor and the number of used processors is equal to the number of tasks (*N*). The developed code automatically distributes the processors after generating the vector of tasks. All calculations were performed on Intel® Workstation with Xeon® 2.27 GHz 16-cores processor and 24 GB RAM.

3. RESULTS

In the developed code speedup of calculations is achieved in two independent ways. The first is based on one calculation of one index matrix *IJ*(DOF,DOF) for all tasks. The effectiveness of this method depends on the relationship between the time of calculating the index matrix *IJ* τ_m and the time of one solution of FEM τ_S. During calculation, the number of tasks *N* variated from 1 to 20. The calculations were performed on a computer with the number of processors (*p*) 16.

For conventional sequential computations, the calculating time is $\tau = N(\tau_m + \tau_S)$. But if the proposed algorithm is used, this value becomes equal to $\tau = \tau_m + N\tau_S$. Therefore, $SpeedUp_1$ can be calculated from the equation:

$$SpeedUp_1 = \frac{(\tau_s + \tau_m)N}{\tau_m + N\tau_s} \tag{10}$$

The value of $SpeedUp_1$ depends on DOF, *N*, and conditions of calculation. For the analysis, three FEM models with different DOF in mechanical tasks were chosen. Model 1 matched the DOF = 23004, model 2 – DOF = 46008, and model 3 – DOF = 60963. The dependence of $SpeedUp_1$ on the number of tasks (*N*) and the value of DOF is shown in Fig. 5.

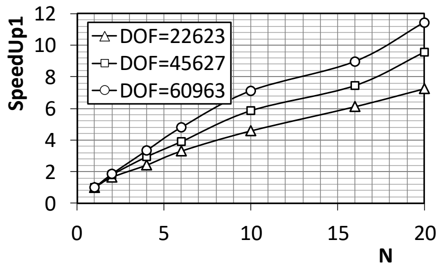

Fig. 5. Dependence of *SpeedUp*$_1$ on the number of tasks (N) and the value of the degree of freedom (DOF)

The second way of speedup computing is based on the parallelization of calculations. To evaluate the efficiency of parallel computations, a comparison was made between parallel and sequential modes. The two parameters were calculated to evaluate the efficiency of parallel computations:

$$SpeedUp_2 = \frac{(\tau_s+\tau_m)N}{\tau_m+\tau_{sNpar}} \tag{11}$$

and

$$SpeedUp_3 = \frac{\tau_s N}{\tau_{sNpar}} \tag{12}$$

where: τ_{sNpar} – time of solution of *N* tasks in parallel mode.

The parameter *SpeedUp*$_2$ characterizes the total acceleration of the solution from the influence of two factors – the use of a common matrix of addresses of nonzero elements and parallel solution of FEM tasks. Fig. 6 shows the dependence of *SpeedUp*$_2$ on *N*. Unlike *SpeedUp*$_1$, the dependence of *SpeedUp*$_2$ on *N* is non-linear and has an extremum for large DOF. The reasons for this nonlinearity will become clear if we analyze the dependence of *SpeedUp*$_3$ on N (Fig. 7). As follows from Fig. 7, the speedup during solving the FEM tasks in parallel mode decreases to 1 at *N* = 11–15.

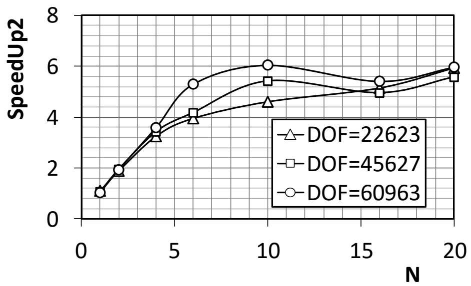

Fig. 6. Dependence of SpeedUp$_2$ on the number of tasks (N) and the value of the degree of freedom (DOF)

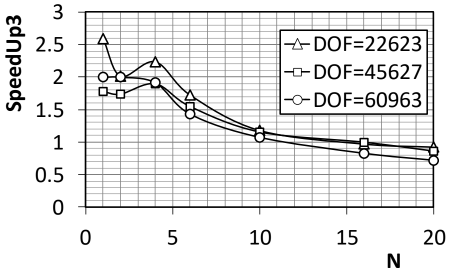

Fig. 7. Dependence of SpeedUp$_3$ on the number of tasks (N) and the value of the degree of freedom (DOF)

4. DISCUSSION AND PRACTICAL IMPLEMENTATION

The calculation results showed that the speedup of parallel solution ($SpeedUp_3$) decreases with an increase in the number of parallel tasks (parallel slowdown). This is because the number of calls to one common piece of computer memory (matrix with addresses of nonzero elements in the stiffness matrix) is increasing. There is also a decrease in $SpeedUp_3$ when the number of tasks exceeds the number of available processors. It is empirically established that developed code in parallel mode is effective for number of tasks late than 0,7–0,9 of the number of available processors. Thus, at some point, it becomes effective to use a sequential solution to all tasks and to use a shared matrix of addresses of nonzero elements in the stiffness matrix. The achieved acceleration at the optimal choice of the algorithm is 2–10 times compared with the classical multivariate calculations in the FEM. For sequential mode the dependence between the time of solution and N is close to linear for all ranges of N. However for parallel mode, this dependence is not linear. The time of solution in parallel mode significantly increased for $N > p$ and became more than the time of sequential solution ($SpeedUp_3 < 1$).

Consider the practical application of the developed code to obtain a map of allowable parameters. To this goal, we perform calculations by the technique of the factor design. Velocity V_0 varied in the range 10–20 mm/s with increments of 5 mm/s, and ΔV varied in the range 2–11 mm/s with increments of 3 mm/s. Such a matrix of factors led to the calculation of 12 variants. The initial diameter of the wire was 0.2 mm, the laser power was 5.5 W and the diameter of the laser beam was 0.4 mm. This value is larger than the wire diameter. Therefore, only part of the laser energy heats the wire. This fact was taken into account in the model by determining the real area of intersection of the laser beam and the wire. The results of calculating the final diameter are presented in the form of a map of allowable parameters (Fig. 8). On this map, the isolines correspond to the final diameter of the wire, which can be obtained using the appropriate combination ΔV and V_0. The area above the isoline 0.1 mm corresponds to the neck formation and subsequent breaking of wire (in Fig. 8 it is indicated by the caption "Fracture"). An example of a calculation in which a neck is formed is shown in Fig. 9. Thus, the resulting map allows to determine the process parameters based on the required final wire diameter, that is, solve the inverse problem. The solution was carried out in parallel mode, the total solution time was 2h 15’. The achieved speedup of calculation of inverse problems made it possible to use the developed FEM code in the control software of laboratory setup for laser dieless drawing, shown in Fig. 1 for generation maps of allowable parameters for required diameters and materials.

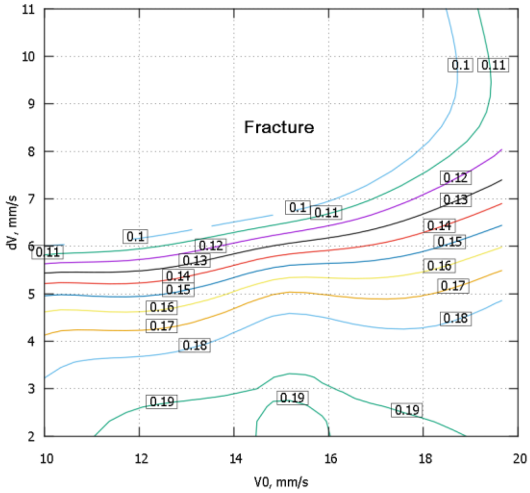

Fig. 8. Calculated allowable processing map for laser dieless drawing of wire from CuZn37 alloy for initial wire diameter 0.2 mm

Experimental tests, carried out on a laboratory setup (Fig. 1, b) in accordance with the calculated allowable processing map (Fig. 8) showed the following. For the calculation shown in Fig. 9, a, in the experiment, a wire breakage is also observed according to the neck formation mechanism (Fig. 9, b).

On the other hand, drawing in the zone of acceptable parameters gives a satisfactory result, which consists in obtaining a defect-free wire, which is shown in Fig. 10.

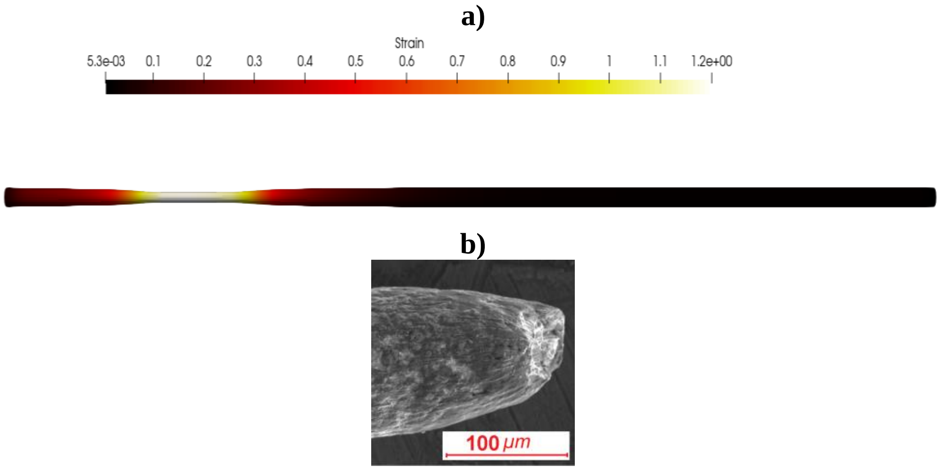

Fig. 9. Example of neck formation during dieless drawing (V_0 = 15 mm/s, ΔV = 7 mm/s): a – simulation; b – experiment

a) b)

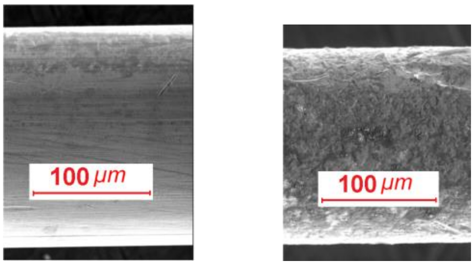

Fig. 10. Example of successive deformation of wire according allowable processing map (V_0 = 15 mm/s, ΔV = 5 mm/s): a – initial wire of diameter 0.2 mm; b – wire after dieless drawing to diameter 0.17 mm

5. CONCLUSIONS

This study is devoted to the problem of solving and accelerating the solution of inverse thermomechanical problems for the laser dieless drawing process of thin wire. The proposed methods, however, can be extended to any inverse problems, when all direct tasks have the same number of nodes, finite elements, and same nodal connections.

The developed FEM code was designed to solve inverse problems in the technology of laser dieless drawing of thin wires. The numerical efficiency of the code is based on simultaneous use by all FEM tasks one shared matrix of addresses of non-zero elements in the stiffness matrix and parallel computing. The developed FEM code in parallel mode is more effective for the number of tasks late than 0.7-0.9 of the number of available processors.

A practical example of analysis of the laser dieless drawing process, in which the map of allowable parameters was obtained, is shown and validated in the study.

Acknowledgments

This project was financed by the NCN of Poland, Project No. 2017/27/B/ST8/01471.

REFERENCES

Chandra, R., Dagum, L., Kohr, D., Menon, R., Maydan, D., & McDonald, J. (2001). *Parallel Programming in OpenMP*. Elsevier Science.

Chenot, J., Massoni, E., & Fourment, J. L. (1996). Inverse problems in finite element simulation of metal forming processes. *Engineering Computations*, *13*(2/3/4), 190–225. https://doi.org/10.1108/02644409610114530

Furushima, T., & Manabe, K. (2007). Experimental and numerical study on deformation behavior in dieless drawing process of superplastic microtubes. *Journal of Materials Processing Technology*, *191*(1), 59–63. https://doi.org/https://doi.org/10.1016/j.jmatprotec.2007.03.084

Hensel, A. & Spittel, T. (1978). *Kraft- und Arbeitsbedarf bildsamer Formgebungsverfahren*. VEB Deutscher Verlag fur Grundstoffindustrie.

Jaluria, Y. (2021). Strategies for solving inverse problems in thermal processes and systems. *International Journal of Numerical Methods for Heat & Fluid Flow*, *31*(10), 3073–3088. https://doi.org/10.1108/HFF-12-2019-0926

Kraft, F. B. (1980). Three fine wire drawing systems – in economic comparison. *Wire Journal International*, *19*, 103–105.
Kubo, S. (1988). Inverse Problems Related to the Mechanics and Fracture of Solids and Structures. *JSME International Journal. Ser. 1, Solid Mechanics, Strength of Materials*, *31*(2), 157–166. https://doi.org/10.1299/jsmea1988.31.2_157
Lesnic, D. (2021). *Inverse Problems with Applications in Science and Engineering*. Chapman and Hall/CRC.
Li, Y., Quick, N. R., & Kar, A. (2002). Dieless laser drawing of fine metal wires. *Journal of Materials Processing Tech.*, *123*(3), 451–458.
Milenin, A. (2017). Parallel FEM code for simulation of laser dieless drawing process of tubes. *Computer Methods in Materials Science*, *17*(4), 178–185.
Milenin, A., Kustra, P., Furushima, T., Du, P., & Němeček, J. (2018). Design of the laser dieless drawing process of tubes from magnesium alloy using FEM model. *Journal of Materials Processing Technology*, *262*, 65–74. https://doi.org/https://doi.org/10.1016/j.jmatprotec.2018.06.018
Milenin, A., Wróbel, M., & Kustra, P. (2021). Investigation of the workability and surface roughness of thin brass wires in various dieless drawing technologies. *Archives of Civil and Mechanical Engineering*, *22*(1), 10. https://doi.org/10.1007/s43452-021-00331-2
Pokorska, I. (2007). Direct and inverse problems in metal forming of rigid-poroplastic materials. *Journal of Materials Processing Technology*, *184*(1), 146–156. https://doi.org/https://doi.org/10.1016/j.jmatprotec.2006.11.015
Schenk, O., & Gärtner, K. (2004). Solving unsymmetric sparse systems of linear equations with PARDISO. *Future Generation Computer Systems*, *20*(3), 475–487. https://doi.org/https://doi.org/10.1016/j.future.2003.07.011
Szeliga, D., Gawąd, J., & Pietrzyk, M. (2004). Parameters Identification of Material Models Based on the Inverse Analysis. *International Journal of Applied Mathematics and Computer Science*, *14*, 549–556.
Szeliga, D., & Pietrzyk, M. (2007). Testing of the inverse software for identification of rheological models of materials subjected to plastic deformation. *Archives of Civil and Mechanical Engineering*, *7*(1), 35–52. https://doi.org/https://doi.org/10.1016/S1644-9665(12)60003-X
Thomas, A. E., Abbes, B., Li, Y. M., Abbes, F., Guo, Y.-Q., & Duval, J.-L. (2017). A coupled thermo-mechanical pseudo inverse approach for preform design in forging. *AIP Conference Proceedings*, *1896*, 170004. https://doi.org/10.1063/1.5008202
Tiernan, P., & Hillery, M. T. (2004). Dieless wire drawing—an experimental and numerical analysis. *Journal of Materials Processing Tech.*, *155–156*(Complete), 1178–1183. https://doi.org/10.1016/j.jmatprotec.2004.04.175
Tiernan, P., & Hillery, M. T. (2008). Technical paper. *Journal of Manufacturing Processes*, *10*(1), 12–20. https://doi.org/10.1016/j.manpro.2008.05.001

Applied Computer Science, vol. 13, no. 8, pp. 54–62
doi: 10.35784/acs-2022-21

Submitted: 2022-06-23 | Revised: 2022-07-26 | Accepted: 2022-09-26

Keywords: sustainable development, process optimization

Agnieszka ZACHCIAŁ [0000-0003-4538-1954]*,
Andrzej JARDZIOCH [0000-0003-1285-8330]**

APPLICATION OF SIMULATION RESEARCH TO ANALYSE THE PRODUCTION PROCESS IN TERMS OF SUSTAINABLE DEVELOPMENT

Abstract

Sustainable development is an very important idea nowadays and it influences on many factors. It is very important to focus on the goals of sustainable development and implement them both in industry and in everyday life. The aim of the article is to analyse the impact of implementing an automatic conveyor belt transport system between the stands of an exemplary assembly line on sustainable development in economic and environmental terms. The analyzed production process consists of one production line with six assembly stations. The efficiency of individual design solutions and electricity consumption were adopted as the evaluation criteria. To compare the two processes, a simulation analysis was performed in the Plant Simulation program. First chapter is the introduction to the article. The second chapter describes the current applications of simulation tests. The third chapter describes the production system that is improved by adding conveyors. The next chapter compares the processes with and without the use of conveyors and presents how much energy must be used additionally by implementing conveyor belts, but also what energy savings can be obtained by installing additional stop sensors. The fifth chapter presents the conclusions: the conducted research allowed concluding that the implementation of conveyor belts affects a higher number of finished products at the same time as the transport of components is manual. However, the best solution is to use conveyors with stop sensors, and the power consumption is then low and more profitable for the enterprise.

1. INTRODUCTION

Sustainable development has many definitions, but the main goals of sustainable development are to focus on economic, social and environmental factors (Adamczyk, 2009). According to the World Commission on Environment and Development, sustainable development is a process of progress in which asset utilization, investment management, organization of technological development, and corporate revolution are perpetuated against

* West Pomeranian University of Technology in Szczecin, Faculty of Mechanical Engineering and Mechatronics, Mechanical Engineering, Szczecin, Poland, za24915@zut.edu.pl
** West Pomeranian University of Technology in Szczecin, Faculty of Mechanical Engineering and Mechatronics, Mechanical Engineering, Szczecin, Poland, andrzej.jardzioch@zut.edu.pl

new and existing requirements (Gazzola, Del Campo & Onyango, 2019). It should be emphasized that nations show different levels of development. Sustainable development is emerging as a global key perception we must recognise to meet socio-economic, technological and environmental challenges (Jovane et al., 2008; Tucki et al., 2022). In manufacturing companies, we have an influence on all the factors mentioned above. Starting with economic factors, you can influence the process optimisation by using energy-saving and efficient machines, and you can also optimise production processes so that energy efficiency is as high as possible. Energy consumption is also very important in a social context. Energy consumption has doubled over the last 40 years and is expected to double again in the next 10 years (May et al., 2015). Industry is one from major energy consumers. It is necessary to reduce energy consumption and demand in the manufacturing industry. Industry plays a key role in meeting the continual increase in demand as the standard of living increases. Direct reduction of energy supply for manufacturing industry is unrealistic because energy is an irreplaceable production factor. Enterprises limit to some extent the reduction of energy consumption while maintaining the same power. Hence, questions arise as to how to improve energy efficiency or reduce energy demand for the same production, and this becomes a critical approach to achieving the goal of reducing energy consumption and sustainable development (Gao et al., 2020). Economic factors affect the minimisation of expenses and increase the company's profits, with a simultaneous positive impact on the environment. The growing interest in more ecological solutions influences the search for solutions with a positive impact on the environment (Seroka-Stolka, 2014). By having an impact on the environment, the production company contributes to lower energy consumption, the use of renewable materials, as well as minimising material scrap, and this affects social factors. Society is not exposed to an unhealthy natural environment, lack of natural resources, and an excessive amount of post-production waste. Therefore, sustainable development is important and touches on many levels. Influencing all of the above factors, more and more companies are trying to meet the requirements of sustainable development (Misztal, 2018). Achieving sustainable development is important to any society, especially developing ones, but industrial growth may not be enough. On the one hand, development means an increase in GDP; on the other hand, it is a means to raise the financial and social status of impoverished economies, raise employment levels, make better use of resources and stimulate social equality (Salih, 2003). A very important element of implementing sustainable development in any field is the support of social, management, and regional and national policy, which is described in detail in the dissertation (Conroy & Berke, 2004).

The aim of the article is to analyse the impact of implementing an automatic conveyor belt transport system between the stands of an exemplary assembly line on sustainable development in economic and environmental terms.

First chapter is the introduction to the article. The second chapter describes the current applications of simulation tests. The third chapter describes the production system that is improved by adding conveyors. The next chapter compares the processes with and without the use of conveyors and presents how much energy must be used additionally by implementing conveyor belts, but also what energy savings can be obtained by installing additional stop sensors. The fifth chapter presents the conclusions.

2. APPLICATION OF SIMULATION RESEARCH

One of the methods of analysing production processes is the use of simulation tests. Having access to many computer programs, it can be recreated or create the desired process and optimise it. With such tools, at a low cost, it can be checked what changes or how to create a production line to meet the goals and requirements of sustainable development. For example, in real processes, machine tools remain idle most of the time and then consume about 80% of the energy (Mouzon, Yildirim & Twomey, 2007). In this case, the appropriate planning of the machining process as well as the appropriate use of production scheduling can significantly affect the efficiency of the process. When analysing the research to date, one can refer to the research (Misztal, 2018), where the assessment of the progress of the sustainable development of Polish business entities was carried out, taking into account economic, environmental and social conditions. However, these studies do not focus on a specific example of an improvement used in a given enterprise, but on a total of 105 enterprises in a given period. Sustainable development is described a bit more in the book (Kronenberg & Bergier, 2010), but the authors focused on general knowledge without researching the sustainable development of enterprises. Also, in the article (Terelak Jardzioch & Biniek, 2018), the impact of the use of production scheduling on energy efficiency was analysed, and the results showed that in the scheduling of production orders, from 5 to 45% electricity savings can be achieved, while in my research, I am going to use the scheduling of production orders and check whether it will affect the sustainable development of the company. In the article (Lee, Zhang & Ng, 2019), the authors presented a comparison of simulation results with a real process, how decisions are made to optimise the workforce, improve performance in a specific dishwasher factory, and the impact of these studies on sustainable development. Optimisation of work on the production line is presented. Another example of simulation tests was described in the article (Liu et al., 2018; Jasiulewicz-Kaczmarek & Gola, 2019)), first, the drivers and challenges were analysed, and the boundaries and connotations of production systems were defined. Next, an energy-based computational model for energy, materials, services, and waste was presented, taking into account the diversity and input and output dimensions of production systems. In addition, certain indicator systems have been established, including functional energy indicators, structural energy indicators, eco-efficiency indicators and sustainability indicators of production systems. Thanks to these indicators, the internal relationship between the economic, environmental and social benefits of production systems is revealed. On this basis, an improvement card was developed to achieve excellent quality, high efficiency, reduction of energy consumption, resource-saving and environmental protection of production systems. Finally, the case study illustrates the feasibility of the proposed method, and the results show that the proposed method provides theoretical support for assessing and improving the sustainability of production systems to coordinate resources and develop the manufacturing industry. Additionally a very important issue in production is to use modern transmitters, sensors and telematics tools. In the article (Topolski, 2018), the authors proved that replacing the push method with the pull method shortened the production time, additionally, the implementation of RFID technology increased the company's turnover by 19.9–21.2%.

3. DESCRIPTION OF THE PRODUCTION SYSTEM

The production process consists of one production line with six assembly stations. The layout is shown in Figure 1. All assembly stations are used for the manual assembly process. One production order consists of fifteen identical products. No retuning of the production line is required. Operation times at each workstation are similar; however, in the production process, where employees transport the product between workstations, the time is extended. To show the impact of the ranking on sustainable development, the value of the energy consumed was assigned, which is consumed at each station and in the second model, in which transporters are used. To compare the two processes, a simulation analysis was performed in the Plant Simulation program.

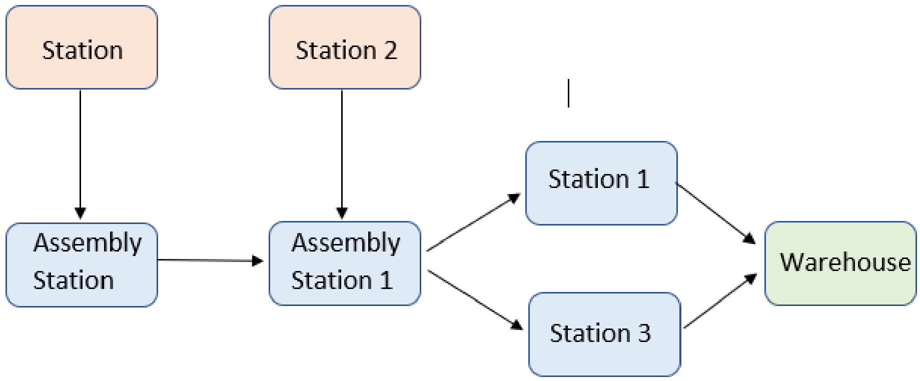

Fig. 1. Diagram of the production line

Table 1 shows the original working times at the given positions. After simulating with conveyor belts, times will be optimized. The times for station1 and station3 are extended by 1 minute – this is an additional time to transfer the final product to the storage place. In the model with the use of tapes, this time is not needed.

Tab. 1. Working time at given positions

Position	Working time [min]
Station	10:00
AssemblyStation	08:00
Station2	10:00
AssemblyStation1	10:00
Station1	21:00
Station3	21:00

As part of the drive to build a system that meets the requirements of sustainable production development, the company decided to investigate whether the implementation of conveyors will allow optimizing the production process, increase the efficiency of the production line and the work of employees (Kopas & Paulikova, 2009). Additionally, to reduce energy consumption (Zhang, 2019), the company decided to check how installing stop sensors in conveyor belts would affect energy consumption. Given that one of the goals of sustainable development is also to facilitate employees' work, this is an additional factor that impacts labour productivity.

4. COMPARISON OF THE PRODUCTION PROCESS WITH AND WITHOUT THE USE OF CONVEYORS

The original production process assumes that employees move components between stations by themselves. The assembled product in the first operations weighs about 3 kg, while the final product weighs 20 kg. Due to the loads transferred, workers move 1 m/s. Employees work 7.5 hours (450 minutes) in one shift.

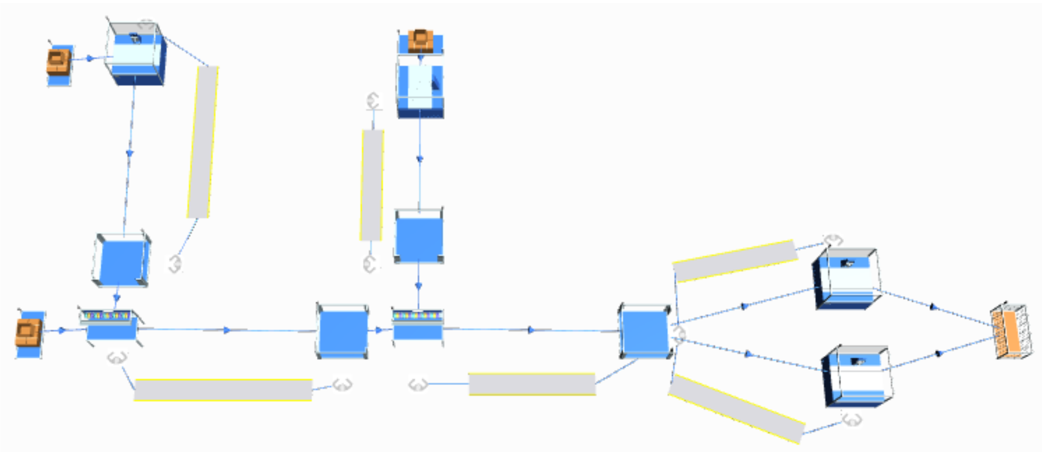

Fig. 2. Scheme of distribution of production stations on the production line without conveyors

Figure 3 shows a diagram of the production line with the use of conveyors between stations.

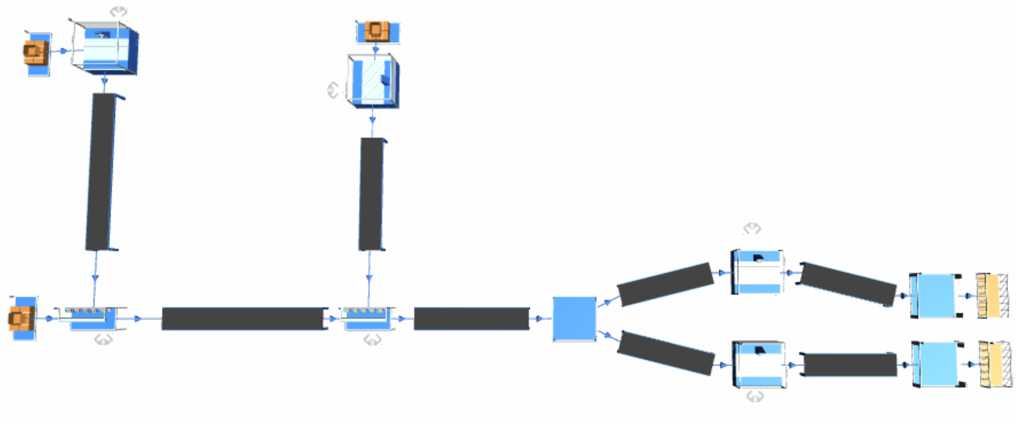

Fig. 3. Scheme of distribution of production stations on the production line with conveyors

4.1. Comparison of the performance of the two production lines

The first data was collected for a line without belt conveyors and with belt conveyors during one shift and during one month of operation, assuming three shifts. The results are showed in Table 2.

Tab. 2. The number of products produced on the production line with and without conveyors at a specified time.

	1 shift (7,5 h)	1 month (3 shifts)
The number of products produced on the production line without conveyors	38	3949
The number of products produced on the production line using conveyor belts	41	4181

During production without the use of conveyors, 38 units of the finished product were produced during one shift and 3,949 units of the finished product were produced during one month. During production with the use of conveyor belts, 41 units of the finished product were produced during one shift and, 4181 units of the finished product were produced during one month.

4.2. Comparison of energy consumption

The results of energy consumption by individual conveyors are presented below. Two options for installing conveyors were analysed: without and with a stop sensor. The belt conveyor stop sensor allows the belt conveyor to be stopped when nothing is being transported. Simulation tests were carried out to check whether the installation of such a sensor allows a significant reduction in the electricity consumption needed to transport items in the production system under consideration.

4.2.1. One shift – 7.5 hours

The first data of energy consumption was collected for a line without and with stop sensors during one shift of operation. The results are showed in Table 3.

Tab. 3. Energy consumption of the production process with the use of conveyors without and with stop sensor

Energy Consumers	Without stop sensors [kWh]	With stop sensors [kWh]
Conveyor	52.5	6.30
Conveyor2	52.5	1.59
Conveyor5	52.5	3.47
Conveyor6	52.5	4.63
Conveyor1	52.5	6.97
Conveyor7	52.5	8.07

4.2.2. One month of production line operation for three shifts

The first data of energy consumption was collected for a line without and with stop sensors during one month of operation, assuming three shifts. The results are showed in Table 4.

Tab. 4. Energy consumption of the production process with the use of conveyors without and with stop sensors during one month of operation

Energy Consumers	Without stop sensors [kWh]	With stop sensors [kWh]
Conveyor	4882.5	489.30
Conveyor2	4882.5	41.84
Conveyor5	4882.5	15.25
Conveyor6	4882.5	16.43
Conveyor1	4882.5	139.16
Conveyor7	4882.5	140.34

4.3. Comparison of the results

When analysing the production process where conveyor belts have been implemented, it can be noticed that the increase in the number of manufactured products is about 6–8%, which means that about a month of work on the production line can be saved per year.

Tab. 5. Comparison of the number of units produced at a given time on two different production lines

	Production line without conveyors	Production line with conveyors	Difference
7,5 h 1 shift	38 pcs	41 pcs	7.3%
1 month 3 shifts	3949 pcs	4181 pcs	5.5%

However, it is equally important to compare the energy consumption of transporters. The parameters of belt conveyors with and without the use of a stop sensor were compared. Below is an overview of the energy consumption of the conveyors.

Tab. 11. Comparisons of energy consumption by conveyors with and without the use of stop sensors

	Conveyors without stop sensor, average power consumption for one belt [kWh]	Conveyors with stop sensor, average power consumption for one belt [kWh]	Difference
7,5 h 1 shift	52.0	5.17	1005.8%
1 month 3 shifts	4882.5	140.39	3477.8%

The cost of 1 kWh for an enterprise is approximately 0.66 PLN on average. Thus, the cost for one shift is approximately PLN 3.41. The rates for 1 kWh are calculated individually for each company. The purchase of conveyor belts is also an individual cost, and each entrepreneur must analyse for himself whether the cost of purchasing belts, maintenance, maintenance, and electricity costs are higher or lower than the profit from shorter maintenance of the production line.

5. CONCLUSIONS

The article presents a simulation that allows comparing two solutions of the designed assembly system. One solution involved transporting products by employees, and the other transporting products using belt conveyors. In the case of the use of belt conveyors, the influence of the use of additional sensors allowing for stopping the conveyor when there are no items to be transported was also checked. The efficiency of individual design solutions and electricity consumption were adopted as the evaluation criteria. The conducted research allowed concluding that the implementation of conveyor belts affects a higher number of finished products at the same time as the transport of components is manual. The difference changes exponentially with longer production times. The lack of conveyor belts is a cheaper solution at the time of implementation, but with annual production, we gain an additional month of production using transporters. The downside of this solution is the high consumption of electricity, which significantly increases production costs. However, the best solution is to use conveyors with stop sensors, and the power consumption is then low and more profitable for the enterprise. Of course, a high initial cost is the purchase, implementation, and then servicing of the conveyors, but these are certainly costs; however, the purchased transporters can be used in other production lines or sold in the future. An additional profit, which is very important and uncountable, is the satisfaction, safety and less burden on employees. Employees do not have to move products between workstations every 10 or 20 minutes. It will have a positive impact on their health, but also increase work safety.

Funding

This study was supported by the Ministry of Education and Science, Poland [Impelenatation Doctorate Programme, granted to Agnieszka Zachciał]

REFERENCES

Adamczyk, J. (2009). *Społeczna odpowiedzialność przedsiębiorstw*. PWE.

Conroy, M., & Berke, P. (2004). What makes a good sustainable development plan? An analysis of factors that influence principles of sustainable development. *Environment and Planning A*, *36*, 1381–1396.

Gao, K., Huang, Y., Sadollah, A., & Wang, L. (2020). A review of energy-efficient scheduling in intelligent production systems. *Complex & Intelligent Systems*, *6*(2), 237–49.

Gazzola, P., Del Campo, A. G., & Onyango, V. (2019). Going green vs going smart for sustainable development: Quo vadis. *Journal of Cleaner Production*, *214*, 881–892.

Jasiulewicz-Kaczmarek, M., & Gola, A. (2019). Maintenance 4.0 Technologies for Sustainable Manufacturing – an Overview. *IFAC-PapersOnLine*, *52*(10), 91–96. https://doi.org/10.1016/j.ifacol.2019.10.005

Jovane, F., Yoshikawa, H., Alting, L., Boer, C. R., Westkamper, E., Williams, D., & Paci, A. M. (2008). The incoming global technological and industrial revolution towards competitive sustainable manufacturing. *Journal of CIRP Annals – Manufacturing Technology*, *57*, 641–659.

Kopas, M., & Paulikova, A. (2009). Specifics of belt conveyor as part of checkout counters and their impacts on operational staff. *Lifting equipment in theory and practice*, *2*, 41–45.

Kronenberg, J., & Bergier, T. (2010). *Wyzwania zrównoważonego rozwoju w Polsce*. Fundacja Sendzimira.

Lee, C. K. M., Zhang, S., & Ng, K. K. H. (2019). In-Plant Logistics Simulation Model for the Catering Service Industry Towards Sustainable Development: A Case Study. *Sustainability*, *11*(13), 3655. https://doi.org/10.3390/su11133655

Liu, C., Cai, W., Jia, S., Zhang, M., Guo, H., Hu, L., & Jiang, Z. (2018). Emergy-based evaluation and improvement for sustainable manufacturing systems considering resource efficiency and environment performance. *Energy Conversion and Management*, *177*, 176-189. https://doi.org/10.1016/j.enconman.2018.09.039

May, G., Stahl, B., Taisch, M., & Prabhu, V. (2015). Multi-objective genetic algorithm for energy-efficient job shop scheduling. *International Journal of Production Research*, *53*(23),7071–89.

Misztal, A. (2018). Zrównoważony rozwój polskich przedsiębiorstw-ewalucja. *Handel Wewnętrzny*, *2*(373), 27–40.

Mouzon, G., Yildirim, M. B., & Twomey, J. (2007). Operational methods for minimization of energy consumption of manufacturing equipment. *International Journal of Production Research*, *45*(18–19), 4247–71.

Salih, T. M. (2003). Sustainable economic development and the environment. *International Journal of Social Economics*, *30*(1/2), 153–162.

Seroka-Stolka, O. (2014). The development of green logistics for implementation sustainable development strategy in companies. *Procedia- Social and Behavioral Sciences*, *151*, 302–309.

Terelak-Tymczyna, A., Jardzioch, A., & Biniek, A. (2018). Planowanie procesu produkcyjnego zorientowane na efektywność energetyczną. In: *Innowacje w Zarządzanie i inżynierii Produkcji* (pp. 521–529). Oficyna Wydawnicza Polskiego Towarzystwa Zarządzania Produkcją.

Topolski, M. (2018). A model for controlling the flow of materials in the production process. *AUTOBUSY – Technika, Eksploatacja, Systemy Transportowe*, *19*(6), 1141–1144. https://doi.org/10.24136/atest.2018.242

Tucki, K., Orynycz, O., Wasiak, A., Gola, A., & Mieszkalski, L. (2022). Potential Routes to the Sustainability of the Food Packaging Industry. *Sustainability*, *14*(7), 3924. https://doi.org/10.3390/su14073924

Zhang, S. (2019). Research on improvement of belt conveyor performance. *International Journal of Recent Advances Multidisciplinary Research*, *6*(04), 4828–4830.

APPLIED COMPUTER SCIENCE

Applied Computer Science, vol. 18, no. 3, pp. 63–85
doi: 10.35784/acs-2022-22

Submitted: 2022-06-14 | Revised: 2022-09-05 | Accepted: 2022-09-14

Keywords: accessibility, usability, universal design, eye tracking, WCAG

Błażej BADZIO[*], *Agnieszka BODZIAK*[*],
Bartłomiej BRODAWKA[*], *Karol BUCHAJCZUK*[*],
Maria SKUBLEWSKA-PASZKOWSKA [0000-0002-0760-7126]*,
Mariusz DZIEŃKOWSKI [0000-0002-1932-297X]*,
Paweł POWROŹNIK [0000-0002-5705-4785]*

ANALYSIS OF THE USABILITY AND ACCESSIBILITY OF WEBSITES IN VIEW OF THEIR UNIVERSAL DESIGN PRINCIPLES

Abstract

Universal design is a strategic approach for planning and designing both the products and their environment, aimed at making a given product available to the widest number of possible users. It ensures equality for all of them and the opportunity to participate in the society. This concept is also crucial in the process of designing and developing software. The research was conducted with the use of four services, three of them were implemented for the purpose of this study. Two of them took into consideration the principles of universal design, while the others did not. The aim of the study was verification of the level of usability and accessibility of services by means of three independent methods: the LUT (Lublin University of Technology) checklist, an assessment taking into account WCAG 2.0 (Web Content Accessibility Guidelines) standards using the automatic WAVE evaluation tool (Web Accessibility Evaluation Tool) and a device allowing to track the movement of the eye while performing various tasks on websites. The websites were assessed by twenty experts in the field of creating web application interfaces, using the LUT checklist. The time to the first fixation (TTFF) that it took respondents to look at specific website elements was measured using the eye tracker device and iMotions software. All websites were checked by means of the WAVE tool to detect irregularities and non-compliance with universal design standards. The analysis performed clearly indicated that websites that follow the universal design guidelines were more useful, intuitive and accessible for users. It might be concluded that interfaces allow to find necessary information and perform desired actions in a shorter time when prepared in accordance with the principles of universal design.

[*] Department of Computer Science, Lublin University of Technology, Lublin, Poland,
blazej.badzio@pollub.edu.pl, agnieszka.bodziak@pollub.edu.pl, bartek.brodawka@gmail.com,
karol.buchajczuk@pollub.edu.pl, maria.paszkowska@pollub.pl, m.dzienkowski@pollub.pl,
p.powroznik@pollub.pl

1. INTRODUCTION

Access to the Internet has become much more common nowadays – about 60% of the Earth's population has it (Digital Around the World, n.d.). News services are the main, and often the only source of news from the world, used by millions of people. Among the users, a significant percentage of them are people with disabilities, often with defects that prevent proper vision or hearing. This problem is marginalized and, as research shows, many websites do not take into account users with special needs, which excludes them from the social space (Leszczyńska, 2019). Therefore, in order to enable all users to have equal access to all available information, special solutions are implemented to make it easier for people to receive content published in the Internet. The main institution dedicated to spread awareness about web accessibility is the World Wide Web Consortium – W3C (W3C, 2022). This year it has come up with the Web Accessibility Initiative, or WAI (Initiative (WAI), W3C Web Accessibility, n.d.). In addition to educational activities, it is also involved in the creation of new guidelines, the development of evaluation tools and conducting research, the effect of which is to improve the accessibility of graphical user interfaces (GUIs). The field that deals with equality in access to products and the environment is universal design (UD). It assumes access for as many users as possible, who can use them independently (Centre for Excellence in Universal Design, n.d.). It should be noted, however, that facilitating access to content via the Internet for people with disabilities is only one of many aspects of universal design. Another, equally important, is to facilitate access to information for technically excluded people. The needs of these people require taking into consideration specific functionalities at the interface design level in order to comfortably use the Internet resources. One of the above-mentioned groups are people with visual impairment. Depending on the type of visual impairment, they require additional GUI functionalities, such as: the ability to magnify the text, listening to content, or entering it by voice. One of the key issues for the interface to be clear and easy to use is the way elements are arranged on the page. For their correct implementation, the WCAG guidelines (Web Content Accessibility Guidelines 2.1., n.d.) are used. It is a set of rules and recommendations aimed at guaranteeing solutions to the largest group of users.

The aim of this paper was to build two websites, taking into consideration the WCAG guidelines, and then compare them with real equivalents existing in the Internet that do not meet the accessibility requirements. The principles of universal design were implemented during the development of both websites. In the case of the implementation of the former, the emphasis was placed on the placement of GUI elements, while in the case of the latter – on the contrast settings. An experiment was prepared for the analysis, in which three different research methods were used. The eye tracking technique was used in the first analysis, the WAVE validator in the second, and the LUT (Lublin University of Technology) checklist in the last one. The impact of the placement of elements on the website on the speed of their location by the user, the number of errors according to the WCAG 2.0 standard and the ergonomics of the developed user interfaces were examined. As part of the work, two research hypotheses were formulated: "an information service limited by access barriers for people with visual impairment is less perceived and more difficult to use than an accessible service" and "a service made in accordance with the principles and guidelines of universal design is more intuitive to use".

2. LITERATURE REVIEW

Accessibility for people with various disabilities, broadly understood, has been a frequently analyzed scientific issue recently. In the article (Stasiak & Dzieńkowski, 2021) university websites were examined in terms of the level of their accessibility for people with disabilities. The study consisted of two parts. The first one uses a 13-question checklist, while the second one uses five automatic tools (Lighthouse, ACE, MAUVE ++, FAE, Utilitia) to evaluate websites in terms of their compliance with the WCAG standard. On the basis of the obtained results, the authors concluded that the analyzed websites required additional functionalities, such as the possibility of changing the interface colours and implementing the mobile version of the website.

The availability of library pages for people using screen readers was analyzed in (Yoon et al., 2016). Research was carried out, consisting of a survey part, in which participants reported accessibility problems, and a part in which automated testing tools were used. The results showed that the library sites are not accessible to users with visual impairments who use screen readers. The most frequently encountered accessibility barriers were due to problems with navigation and semantics, not to coding errors.

The article (Fogli, Provenza & Bernareggi, 2014) presents the developed language of design patterns ensuring accessibility also for blind designers, the creation of which was preceded by a three-stage analysis: heuristic evaluation, a survey and an analysis of created websites. The paper (Pascual et al., 2014) analyzed the impact of barriers on the mood of website users depending on the accessibility of information contained on websites. The study took into account time of performed tasks, efficiency as a way to understand the usefulness of the website through the percentage of positively completed tasks and the final satisfaction of each task. The results showed that the WCAG 2.0 compliant site had better performance, effectiveness and user satisfaction scores. The availability of the Norwegian Broadcasting Corporation's news services to ensure equal access to information for different social groups was analyzed in (Sanderson, Chen & Kessel, 2015). The study consisted of interviews with participants, analysis of functionality, structure and navigation of websites. Based on the answers provided and the heuristic assessment, it was concluded that the websites that participated in the study did not meet the standards compliant with WCAG 2.0. The availability of websites of universities, corporations and federal institutions in the USA, with particular emphasis on people with visual impairments, has been investigated in (Michalska et al., 2014). The results of more than ten years of research presented there proved that the analyzed websites were unavailable in terms of consistency and transparency according to the WCAG guidelines. The main cause of these problems was the constant change of information on pages, the rotation of people responsible for the appearance of the sites and too fast maintenance of the system, not taking into consideration the issues of compliance with WCAG rules. A similar study was presented in (Harper & Chen, 2012), where over 6,000 websites over 10 years were analyzed in terms of the accessibility standards used. The results showed that only 10% of the websites surveyed follow the WCAG guidelines.

The article (Pivetta et al., 2013) analyses a number of validation tools to verify the Moodle learning platform for compliance with WCAG 2.0 standards. The WAVE tool (WAVE Web Accessibility Evaluation Tool, n.d.) proved to be the most effective automatic validator. In some situations, an audit using one evaluation tool may turn out to be insufficient, as evidenced by the results of the study presented in (Kumar, Shree DV

& Biswa, 2021). The authors analyzed the availability of two news services using 10 of the most popular evaluation tools. This article (Acosta-Vargas, Acosta & Luján-Mora, 2018) analyzed 348 major Latin American university sites for WCAG 2.0 compliance errors using seven evaluation tools. The results showed that almost all of the analyzed websites were characterized by a significant number of errors, mainly concerning the contrast of elements on the page. The study (Ismail, Kuppusamy & Paiva, 2020) analyzed 59 websites of universities in Portugal in terms of the accessibility of websites for people with disabilities. The analysis was performed with the use of three tools for website validation according to the W3C standard: WAVE, AChecker and aXe. Based on the collected statistical data, it was found that the main problems of the pages concerned the contrasts of elements on the pages, links without visible text, alternative texts for graphics and buttons. It should be noted that the analysis with automatic evaluation tools may often turn out to be insufficient. The book (Abascal, Arrue & Valencia, 2019) compared solutions based on automated scripts and manual crowdsourcing solutions. The results showed that manual analysis was necessary to adapt the website for people with disabilities.

The graphical user interface design is one of the most important aspects when creating and implementing a website. The GUI must not only be readable, but also follow established conventions, such as the arrangement of individual elements on the page. Otherwise, it may be difficult to find the information one is interested in. A study (Alonso-Virgós et al., 2020) proved that there were "learned" behaviors, both for users and web developers, regarding page layout. A similar issue was addressed in (Isa et al., 2016), which analyzed the accessibility of the Malaysian tourism site using the Achecker evaluation tool, and developed a series of guidelines that made it possible to adapt the website and make it more accessible to people with disabilities.

The research carried out in this paper is unique due to the lack of research on websites using eye tracker focusing on the elements responsible for the availability of websites for people with visual impairment, such as farsightedness, myopia or colour blindness.

3. PROTOTYPE TEST APPLICATIONS

The WordPress tool (Narzędzie do blogowania, platforma wydawnicza i system zarządzania treścią witryny, n.d.) was used to create the first application, which allowed the maximum fulfilment of WCAG guidelines and thus managed to minimize the number of errors during testing with the WAVE tool. Wordpress made it easy to manage the content and modify elements directly in the code or with the use of appropriate plugins. The second application was created using three web technologies: HTML hypertext markup language, CSS stylesheet and PHP language. Such a choice was dictated by the desire to gain more control over each fragment of the website, which was important when examining the arrangement of elements.

3.1. Service for testing the contrast and size of elements

In this case, the layout of the graphical user interface has the characteristic features of an Internet information service which contains the most current and most important data on the home page. It is displayed as the largest tile on the page (Fig. 1). Conversely, less important or older messages are displayed below as small tiles. The website also has archival entries, a search by category and a tool for changing the size and type of font, as well as for changing the contrast of colours displayed on the page. It also allows the user to log in/create an account and add comments under articles, in the appropriate section. The user panel also offers the option of editing personal data, changing the password, profile photo and deleting the account on the website.

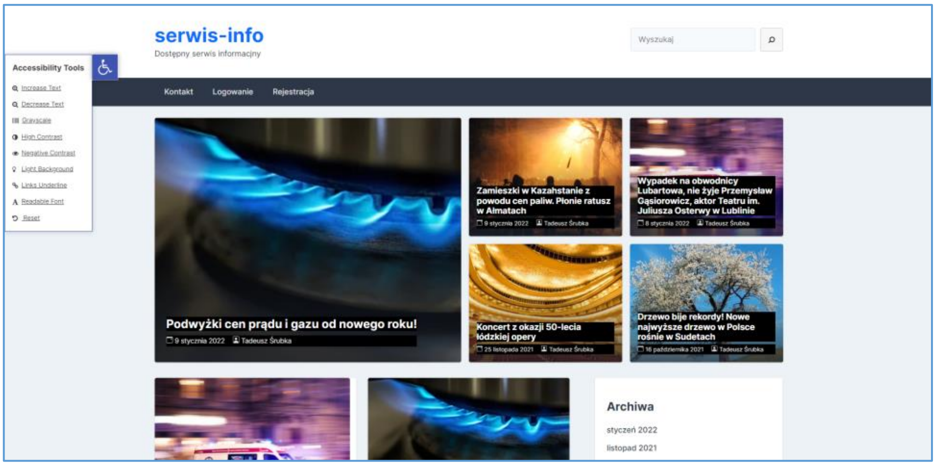

Fig. 1. The main page of the service

3.2. Service for examining the arrangement of elements

The second website has been designed in such a way that its elements responsible for the implementation of the accessibility aspects are arranged in a way resembling other, similar, most popular websites. For this version of the website, prepared in accordance with the principles of universal design (Fig. 2), a CSS file was produced, which ensured the correct arrangement of appropriate elements.

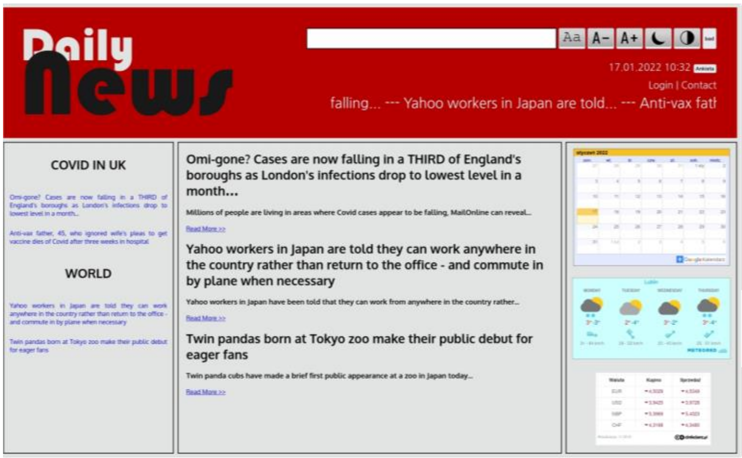

Fig. 2. Main page of UD compatible service

The version of the website inconsistent with the universal design guidelines for the arrangement of elements, created for the purpose of this study, is presented in Fig. 3.

Fig. 3. Main page of UD incompatible service

4. RESEARCH METHODOLOGY

Four experiments were conducted to investigate the quality and accessibility of the web application interface. Two of them involved the use of the eye tracker tool to examine the contrast and the placement of elements on the page. The next one was to use the WAVE validator to verify errors and irregularities according to the WCAG 2.0 standard. For the last study, the LUT (Lublin University of Technology) checklist (Miłosz, 2014) was used, by means of which a subjective assessment of the quality of the analyzed websites was made. Four websites were used for the study. Three developed for the purposes of the research. The first two (Fig. 1 and 2) were compatible with the UD guidelines, while the third one (Fig. 3) was not. The fourth website, available in the Internet (TVP Info, n.d.), also was not compatible with the UD guidelines.

Twenty students of Computer Science with extensive experience in designing and implementing applications participated in the study. All of them took part in the eye tracking study. The participants were divided into two separate groups for assessment of the interfaces using the LUT checklist. They assessed the websites that were and were not compliant with the Universal Design guidelines. Ten of the participants had visual impairments: farsightedness, myopia and colour blindness. They all signed the consent for the study.

4.1. Assessment methods

The first part of the experiment was performed using the Gazepoint GP3 HD eye tracker (GP3 HD Eye-Tracking Device – Take Advantage Of Research-Grade Equipment, n.d.), which uses a camera to monitor the activity of the eyeball (blinks, stops or fast movements) at a frequency of 150 Hz. The iMotions 9.0 (iMotions: Unpack Human Behavior, n.d.) software was used to do the research using the eye tracker. Each participant was shown charts with instructions and individual views of the tested visualizations. The task of the participants was to locate specific elements. The data obtained from the experiment were exported and a statistical analysis was conducted. The measures used in the study were: the number of fixations, fixation duration and the time to the first fixation. Each participant completed 10 tasks for each website.

In the second part of the study, each participant, in order to get acquainted with the websites, received a list of eleven commands to be executed, the content of which was related to the interfaces of two sites with UD and without UD principles. The commands concerned the layout of the interface components and the GUI transparency. Based on their experience, after interacting with websites, they filled in the LUT checklist, using a rating scale from 1 to 5. This measure is based on the Nielsen heuristics. The WUP measure was calculated from the obtained results (Miłosz, 2014).

To determine the availability of websites, the Internet tool "wave.webaim.org" was used to analyze the compliance of websites with the WCAG guidelines. Additionally, this tool allowed to verify the level of the website and set the direction of actions to improve the website / web application. The validator indicated errors that were often unnoticeable and could seriously affect the functioning of the website. The choice of the WAVE tool was preceded by thorough analyses of similar solutions, and was determined by such issues a high assessment of specialists, a wide spectrum of analysis (not only HTML and CSS validation), free license, an attractive way of presenting results, the verification of the correctness of the source code and contrast testing. The research was carried out by two independent experts in the field of universal design and computer science.

5. RESULTS

The first part of the experiment involved conducting an eye tracking study. Each participant was displayed alternately a panel with the content of the task to be performed (Tab. 1) and a view of the website. The static analysis was performed with the use of libraries and a tool created in the R language. In order to verify whether the distribution of the samples is similar to the normal distribution, the Shapiro-Wilk test was performed. Additionally, the Levene's test and the Student's t-distribution were performed to see if the data were significantly different.

Tab. 1. Set of tasks to study contrast, size and placement of elements using an eye tracker

Task no.	Contrast	Size of elements	Element placement
1	Locate the item to search for.	Locate the "Contact" tab.	Locate the item that allows you to print the article.
2	Locate the comments section.	Locate the article tags.	Locate the item with user comments.
3	Locate the article tags.	Locate the article category.	Locate the login button item.
4	Locate the news service department/editorial section in the contact tab.	Locate the source of the article.	Locate the item with the currency rate widget.
5	Locate the article publication date field.	Locate the "Culture" categories in the Category Selection section.	Locate the item that allows to turn on the night mode.
6	Locate the source of the article.	Locate the author of the article.	Locate the item with a bar with scrolling article titles.
7	Locate the “Culture” categories in the Category Selection section.	Locate the item to search for.	Locate the item with the contact number.
8	Locate the “Poland” categories in the Category Selection section.	Locate the "Poland" categories in the Category Selection section.	Locate the marked location on the map.
9	Locate the author of the article.	Locate the comments section.	Locate the location of the registration button.
10	Locate the "World" categories in the Category Selection section.	Locate the article published date field.	Locate the location of the password field.

5.1. Eye tracking study – the Time to the First Fixation

The Time to the First Fixation (TTFF) determines the average time to localize a specific area of interest (AOI). This indicator provides information on how specific aspects of the visual scene are prioritized. This metric is useful for evaluating the performance of two or more areas on the same website, application interface, or for comparing similar GUI elements (iMotions: Unpack Human Behavior, n.d.). A short TTFF means that the searched element was found quickly and indicates its strong visibility through, for example, flashy colour, location in the center of the screen, a large size or visual differentiation from other objects. A longer TTFF may be due to the fact that a given element is not located in the typical place or it is only slightly visible. In Tab. 2. the TTFF was presented for contrast study, on pages with and without UD guidelines.

Tab. 2. TTFF for page contrast study

	UD website Time *(ms)*	**No-UD website Time *(ms)***
Screen 1	556.8	3546.8
Screen 2	120.3	3657.0
Screen 3	591.3	5043.0
Screen 4	897.0	5692.0
Screen 5	627.5	3436.8
Screen 6	524.5	2828.1
Screen 7	919.2	3191.5
Screen 8	1150.3	4940.5
Screen 9	732.4	3259.4
Screen 10	1298.6	3690.1
Mean	741.79	3928.52
Variance	115107.325	899549.006
Standard deviation	339.274	948.445
Confidence intervals	210.281	587.841
Shapiro-Wilka test	0.869	0.090
Levene's test		0.09296116
T-test		$8.872 * 10^{-9}$

The next step was to examine the influence of the element size on two separate websites on the searching time for an element in the GUI. The results are presented in Tab. 3.

Tab. 3. TTFF for size of elements on page study

	UD website Time *(ms)*	**No-UD website Time *(ms)***
Screen 1	780.6	4549.3
Screen 2	438.9	2357.1
Screen 3	877.1	5187.6
Screen 4	528.4	3948.8
Screen 5	838.6	3312.5
Screen 6	673.5	1601.1
Screen 7	651.4	3762.3
Screen 8	810.5	2693.2
Screen 9	549.9	3597.7
Screen 10	579.1	2631
Mean	672.8	3364.06
Variance	22190.375	1155253.394
Standard deviation	148.964	1074.827
Confidence intervals	92.327	666.172
Shapiro-Wilka test	0.635	0.992
Levene's test		0.001565083
T-test		$2.084 * 10^{-5}$

To analyze the influence of the arrangement of elements, tests were performed on two created services. The results of these tests are presented in Tab. 4.

Tab. 4. TTFF for placement of elements on page study

	UD website Time *(ms)*	No-UD website Time *(ms)*
Screen 1	2171.9	5021.3
Screen 2	655.1	1483.4
Screen 3	1541.1	6872.1
Screen 4	1196.8	2531.8
Screen 5	741.3	4488.1
Screen 6	789.7	4937.1
Screen 7	2236.4	5417.2
Screen 8	638.0	2693.3
Screen 9	1509.3	4819.7
Screen 10	512.6	4593.5
Mean	1199.22	4285.75
Standard deviation	640.7257	1592.372
Variance	410529.441	2535648.596
Confidence intervals	397.1186	986.9442
Shapiro-Wilk test	0.4365	0.1032
Levene's test	0.1366	
T-test	$2.16 \cdot 10^{-5}$	

A significant time difference can be noticed in locating all test items in all views used in the experiment. The results of the statistical analysis show that the samples have a normal distribution, however, the samples in the size tests have a non-uniform variance, and the samples in the contrast tests have a homogeneous variance. This means that the analysed samples differ significantly between the websites with and without universal design guidelines.

5.2. Eye tracking study – the number of fixations

The number of fixations is correlated to the total dwell time (Holmqvist et al., 2011). The higher the total number of fixations, the lower the participant's search ability or the worse the structure of displayed stimuli. This means that if the informativeness of stimuli is high (in other words, the structure of stimuli supports the information retrieval process), the number of fixations decreases (Grobelny et al., 2006).

Then, the analysis of the number of fixations for services in individual tasks was carried out. For the results, the mean, standard deviation, variance and confidence intervals were determined, and the Shapiro-Wilk, the Levene's and the t-Student tests were performed. The results for the study of the contrast, size and distribution of elements are presented in Tabs. 5, 6 and 7, respectively.

Tab. 5. Fixation number for the page contrast study

Scr.	UD website					No-UD website					Levene's test	T-test
	Mean	Std. dev.	Variance	Conf. int.	Shapiro-Wilk	Mean	Std. dev.	Variance	Conf. int.	Shapiro-Wilk		
1	4.25	2.022	4.092	0.886	0.2932	13.75	6.773	45.881	2.968	0.1821	0.2873	$5.517*10^{-7}$
2	7.9	4.089	16.726	1.792	0.0861	16.4	8.556	73.200	3.750	0.1593	0.6547	$2.752*10^{-4}$
3	5.95	2.928	8.576	1.283	0.08333	13.65	6.149	37.818	2.695	0.1545	1	$1.115*10^{-5}$
4	11.1	8.668	75.147	3.799	0.0609	25.95	10.708	114.681	4.693	0.0650	0.7282	$2.324*10^{-5}$
5	7	4.267	18.210	1.870	0.3782	15.9	6.307	39.778	2.764	0.0991	0.4259	$6.525*10^{-6}$
6	5.85	2.996	8.976	1.313	0.3123	16.15	9.343	87.292	4.094	0.0512	0.5738	$3.428*10^{-5}$
7	6.75	3.275	10.724	1.435	0.5321	19.05	10.555	111.418	4.626	0.0763	0.3990	$1.425*10^{-5}$
8	6.7	3.840	14.747	1.683	0.3627	18.6	8.543	72.989	3.744	0.0512	0.4630	$1.556*10^{-6}$
9	5.95	2.724	7.418	1.194	0.2119	16.5	6.939	48.157	3.041	0.0552	0.7548	$2.016*10^{-7}$
10	7.95	4.236	17.945	1.857	0.2455	15.4	7.576	57.410	3.320	0.0558	0.9282	$4.551*10^{-4}$

Tab. 6. Fixation number for size of elements on the page study

Scr.	UD website					No-UD website					Levene's test	T-test
	Mean	Std. dev.	Variance	Conf. int.	Shapiro-Wilk	Mean	Std. dev.	Variance	Conf. int.	Shapiro-Wilk		
1	7.6	2.186	4.778	0.958	0.434	18.65	5.742	32.976	2.516	0.35	0.834	$1.002*10^{-9}$
2	5.2	2.261	5.115	0.991	0.144	17.7	6.821	46.536	2.989	0.216	0.207	$2.233*10^{-9}$
3	11.95	6.27	39.313	2.747	0.227	20.2	8.799	77.431	3.856	0.142	0.673	$1.532*10^{-3}$
4	6.6	1.569	2.463	0.687	0.218	19.2	10.149	103.01	4.448	0.17	0.738	$2.879*10^{-6}$
5	6.95	1.19	1.418	0.521	0.112	17.7	8.202	67.273	3.594	0.422	0.464	$1.068*10^{-6}$
6	6.3	2.273	5.168	0.996	0.115	16.95	4.999	24.997	2.191	0.176	0.575	$1.532*10^{-10}$
7	5	2.555	6.526	1.120	0.402	13.6	6.193	38.357	2.714	0.215	0.742	$1.291*10^{-6}$
8	5.5	1.504	2.263	0.659	0.153	17.25	7.202	51.881	3.156	0.081	0.938	$1.585*10^{-8}$
9	6.7	3.294	10.853	1.444	0.151	18.7	10.250	105.063	4.492	0.746	0.746	$1.393*10^{-5}$
10	5.1	1.889	3.568	0.827	0.368	15.9	8.528	72.726	3.737	0.078	0.202	$2.515*10^{-6}$

Tab. 7. Fixation number for placement of elements on the page study

Scr.	UD website					No-UD website					Levene's test	T-test
	Mean	Std. dev.	Variance	Conf. int.	Shapiro-Wilk	Mean	Std. dev.	Variance	Conf. int.	Shapiro-Wilk		
1	8.4	4.453	19.831	1.952	0.1635	11.55	3.394	11.523	1.487	0.0756	0.7573	0.0162
2	7.45	3.605	12.997	1.580	0.5233	10.35	4.568	20.871	2.002	0.0868	0.0314	0.0318
3	6.95	3.845	14.786	1.685	0.4442	9.85	3.232	10.45	1.416	0.4293	0.2085	0.0138
4	7.2	4.456	19.853	1.953	0.1196	10.3	2.993	8.958	1.312	0.1174	0.6147	0.0138
5	7.15	4.171	17.397	1.828	0.0558	10	2.991	8.947	1.310	0.8289	0.4082	0.0175
6	10.5	3.886	15.105	1.703	0.8084	15.3	7.138	50.957	3.128	0.1645	0.4801	0.0119
7	7.05	3.790	14.365	1.661	0.1631	9.7	2.003	4.010	0.877	0.1167	0.1648	0.0088
8	6.6	3.604	12.989	1.580	0.0909	9.4	3.235	10.463	1.418	0.6025	0.7808	0.0137
9	6.05	3.236	10.471	1.418	0.9138	8.75	3.226	10.407	1.413	0.2718	0.5531	0.0119
10	6.9	3.697	13.673	1.621	0.1472	9.8	3.412	11.642	1.495	0.6052	0.6286	0.0139

Based on the above results, a statistical analysis was analogously performed using the same tools. The results show that the data are normally distributed and that they differ significantly. In order to better understand the results, the graphs shown below have been created.

The graphs presented in Figs. 4, 5, 6, 7, 8, 9 show the number of fixations with their statistical data (quarter range, median) depending on the view for studies on contrast, size and placement of elements on the website.

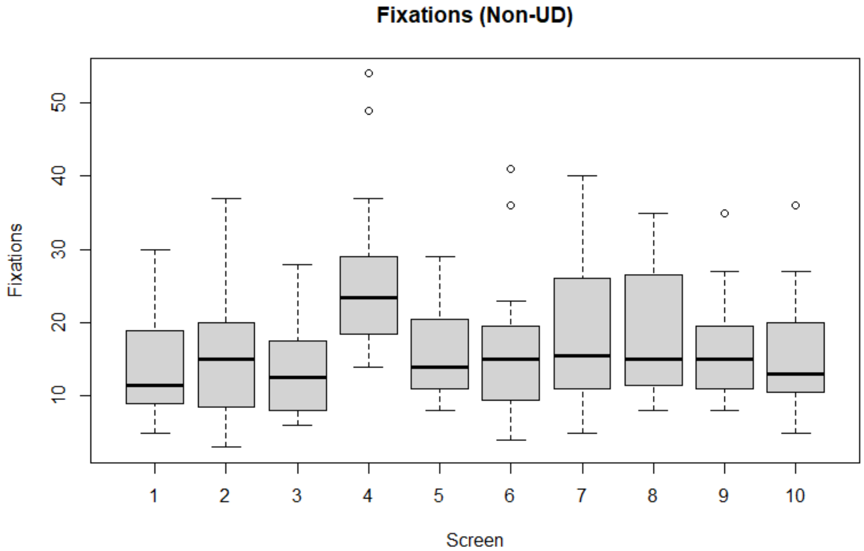

Fig. 4. Number of fixations – element contrast on the website without UD

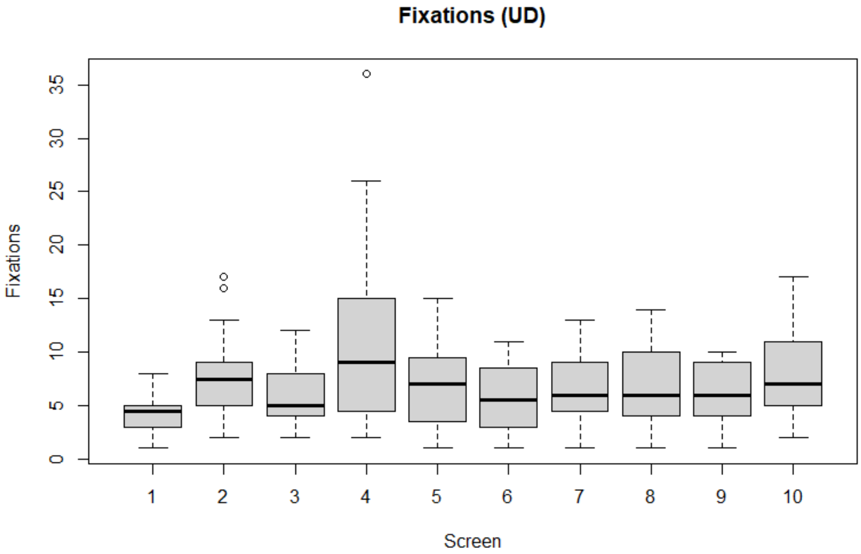

Fig. 5. Number of fixations – element contrast on the UD-enabled website

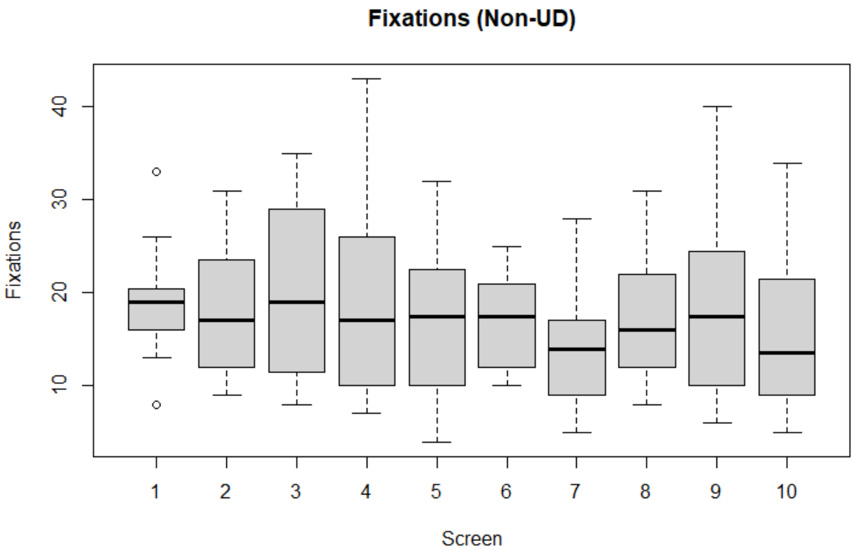

Fig. 6. Number of fixations – element size on the website without UD

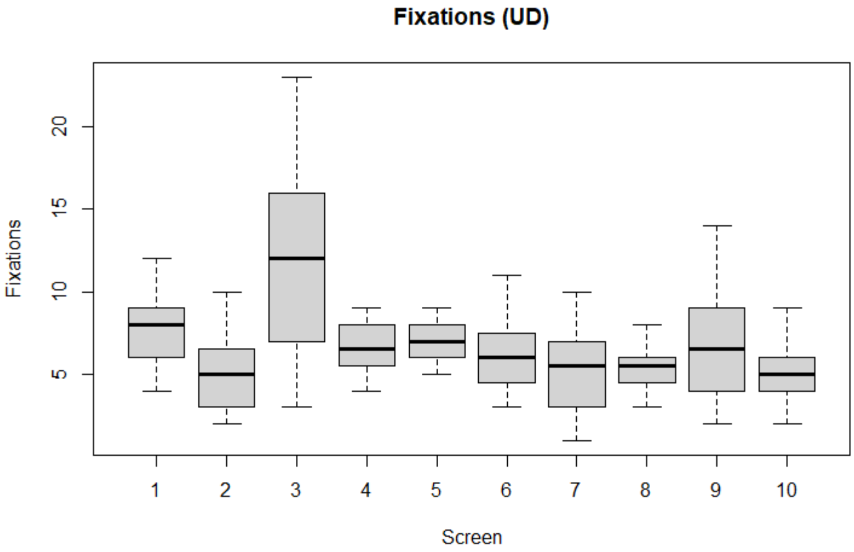

Fig. 7. Number of fixations – element size on the UD-enabled website

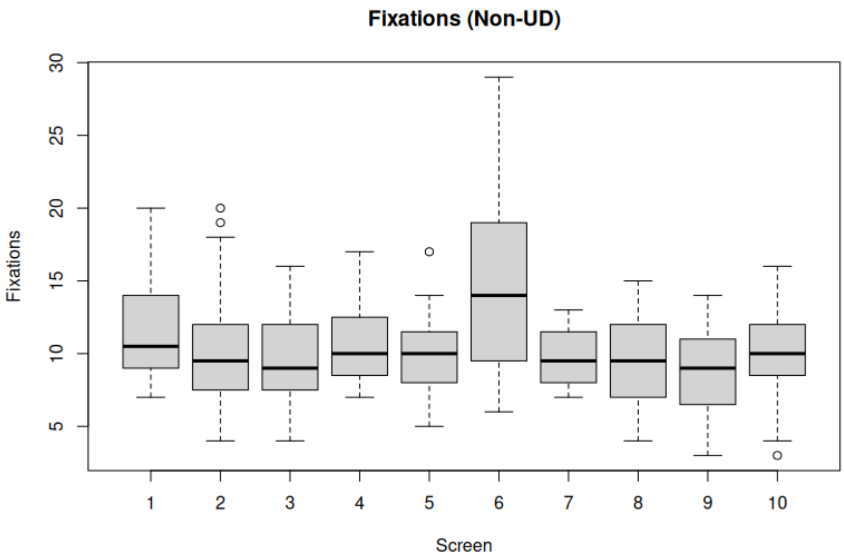

Fig. 8. Number of fixations – element placement on the website without UD

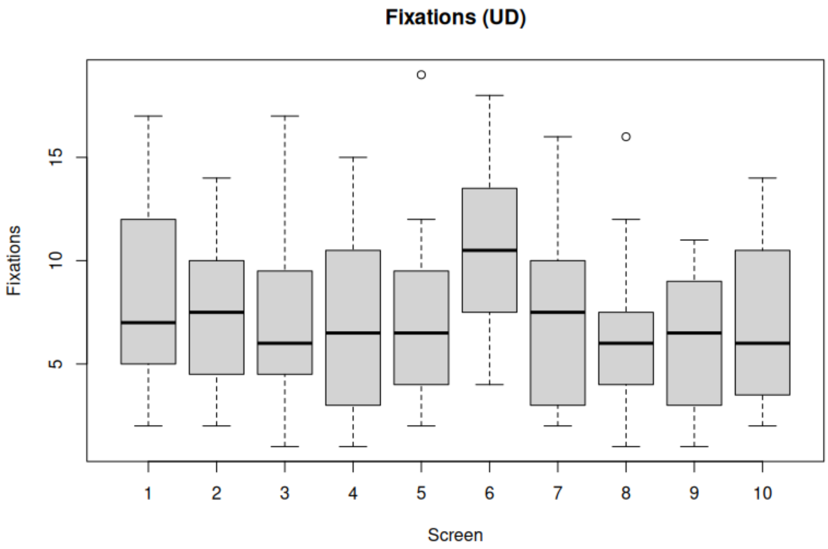

Fig. 9. Number of fixations – element placement on the UD-enabled website

5.3. Eye tracking study – fixation duration

The last analysis of the results concerned the duration of the eye fixation during the execution of the command on individual views. The results of the research and analyses are presented in Tabs. 8, 9 and 10. The duration of fixation can be applied to both individuals and groups. This measure is interesting in the analysis of various stimuli, i.e., various websites or web applications. In the case of the conducted research, the entire page area was the area of interest, and the stimulus exposure time was related to the time of finding the searched object. The interpretation of this measure may be such that the longer the fixation time, the more time the participants spent on it, which means that the displayed scene was more complicated for the respondent. Therefore, this parameter indicates the difficulty or ease of extracting information (Just & Carpenter, 1976).

Tab. 8. Fixation duration for size of elements on the page study

Scr.	UD website fixation duration *(ms)*			No-UD website fixation duration *(ms)*			Levene's test
	Mean	Std. dev.	Variance	Mean	Std. dev.	Variance	
1	2227.028	1766.995	3122270.715	5449.899	1769.524	3131214.445	0.581
2	1626.917	723.749	523813.327	5127.623	1857.711	3451091.645	0.857
3	3604.962	2010.896	4043702.245	6079.612	2051.412	4208292.572	0.207
4	1797.686	792.573	628172.486	5421.189	2640.315	6971261.691	0.257
5	1973.372	801.254	642007.503	5095.739	2147.701	4612618.320	0.535
6	1660.673	766.029	586799.958	4886.513	2715.365	7373205.503	0.548
7	1506.419	623.700	389001.543	4950.125	1959.981	3841524.830	0.903
8	2073.643	856.457	733518.380	5756.947	3622.310	13121127.490	0.228
9	2099.837	1139.046	1297425.948	5455.836	2535.253	6427506.842	0.782
10	2029.934	1576.429	2485128.774	4597.603	2274.366	5172741.132	0.428

Tab. 9. Fixation duration for the page contrast study

Scr.	UD website fixation duration *(ms)*			No-UD website fixation duration *(ms)*			Levene's test
	Mean	Std. dev.	Variance	Mean	Std. dev.	Variance	
1	1452.918	659.319	434702.145	4512.119	1886.928	3560495.866	0.484
2	2533.579	1814.358	3291894.103	4978.360	2730.994	7458329.946	0.712
3	1855.812	1194.277	1426297.826	4593.170	2625.858	6895127.762	0.954
4	3199.884	2715.384	7373309.636	7532.596	4730.115	22373987.380	0.836
5	2422.547	1342.039	1801069.752	5195.723	3177.848	10098718.730	0.825
6	1653.871	819.697	671903.248	4800.330	2172.514	4719816.377	0.928
7	2225.216	1016.202	1032667.433	5446.231	2518.568	6343187.245	0.986
8	2260.856	1366.621	1867652.940	6212.158	4636.144	21493827.830	0.479
9	1929.815	676.483	457629.680	4162.068	2687.036	7220162.087	0.541
10	2517.727	1068.469	1141626.572	4202.766	1914.743	3666240.791	0.944

Tab. 10. Fixation duration for placement of elements on the page study

Scr.	UD website fixation duration *(ms)*			No-UD website fixation duration *(ms)*			Levene 's test
	Mean	Std. dev.	Variance	Mean	Std. dev.	Variance	
1	3363.627	1966.889	3868653.098	3777.575	1645.394	2707324.495	0.8842
2	3004.432	1809.038	3272619.664	3178.353	1843.847	3399775.061	0.5235
3	2017.958	901.001	811804.268	2987.958	2094.494	4386908.777	0.3271
4	2690.388	1685.690	2841553.226	3337.922	1853.905	3436965.436	0.0350
5	2629.681	1627.812	2649772.994	2866.858	1452.316	2109224.619	0.9331
6	3860.748	2556.886	6537671.03	4762.058	2570.120	6605519.337	0.8462
7	2958.867	2297.602	5278976.192	2626.115	1170.858	1370909.47	0.9674
8	2111.905	1126.478	1268953.877	2530.234	1295.602	1678585.633	0.3995
9	2208.277	1103.397	1217486.821	2465.513	1424.831	2030144.452	0.7891
10	2543.359	1304.938	1702863.719	2802.539	1502.594	2257791.467	0.6698

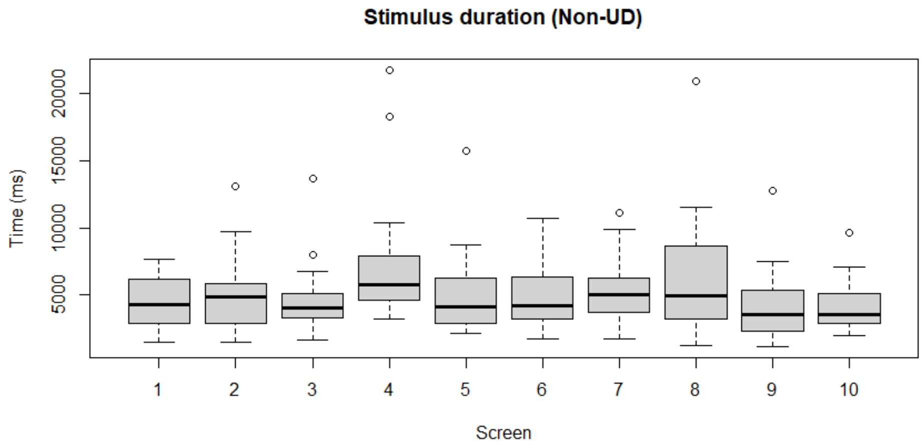

Fig. 10. Duration of fixations – element contrast on the website without UD

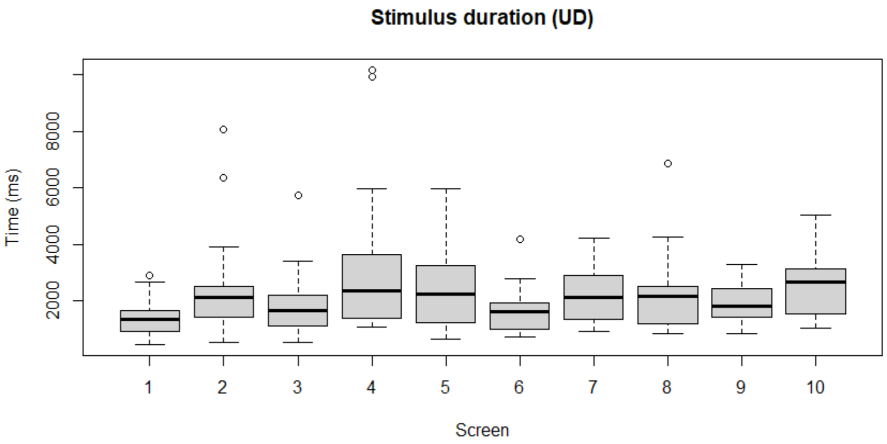

Fig. 11. Duration of fixations – element contrast on the UD-enabled website

In the analysis of the duration, in addition to the standard measures such as mean, standard deviation and variance, the Levene test was also performed, on the basis of which it can be concluded that the samples have a homogeneous variance. Only one sample has a heterogeneous variance. Similarly, as in the case of the number of fixations, due to the large amount of data, the graphs presented in Figures 10, 11, 12, 13, 14, 15 were made.

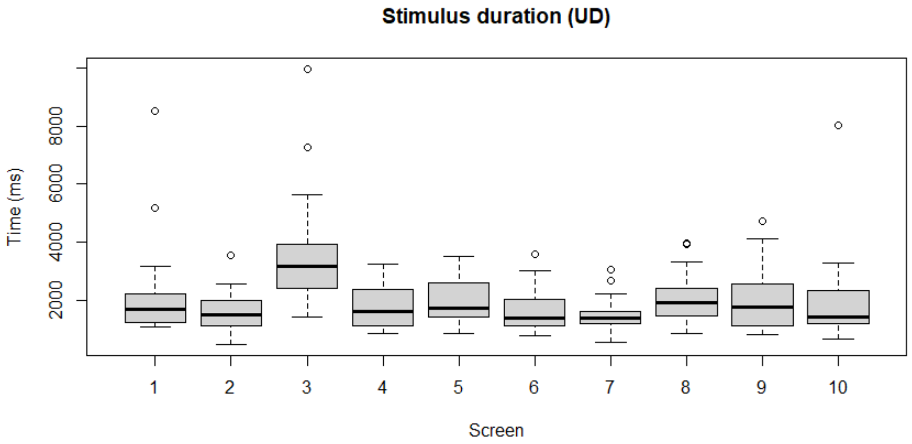

Fig. 12. Duration of fixations – element size on the UD-enabled website

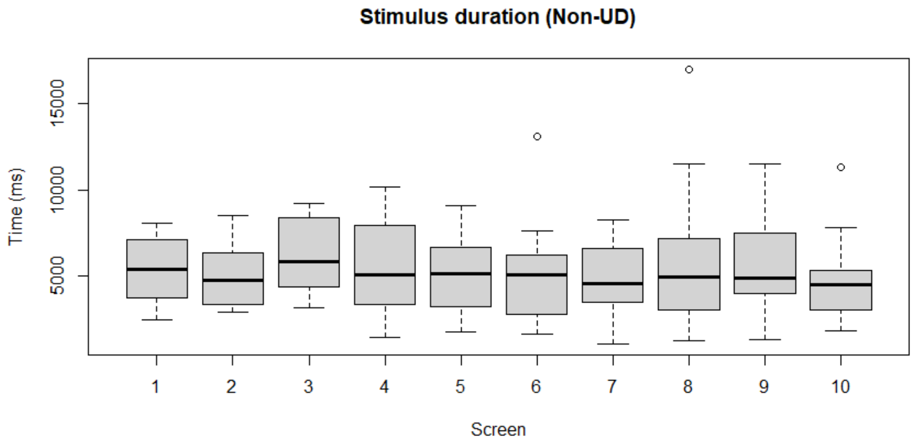

Fig. 13. Duration of fixations – element size on the website without UD

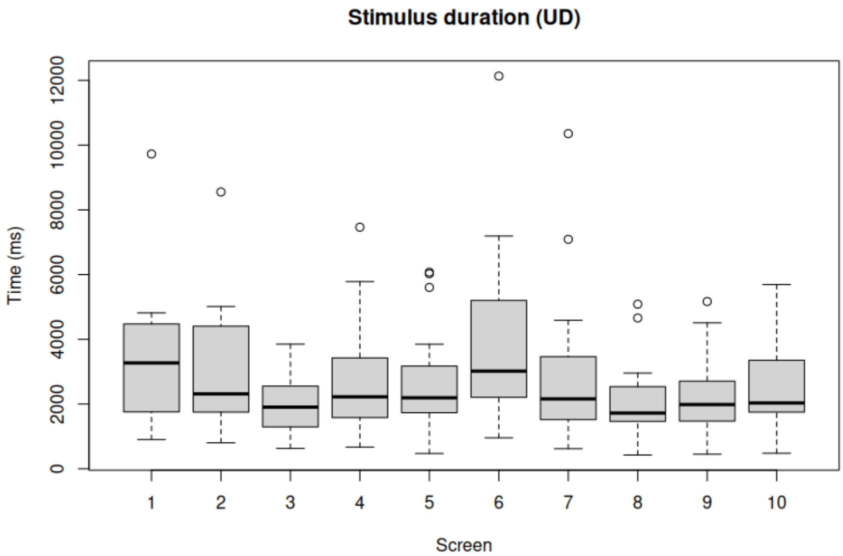

Fig. 14. Duration of fixations – element placement on the UD-enabled website

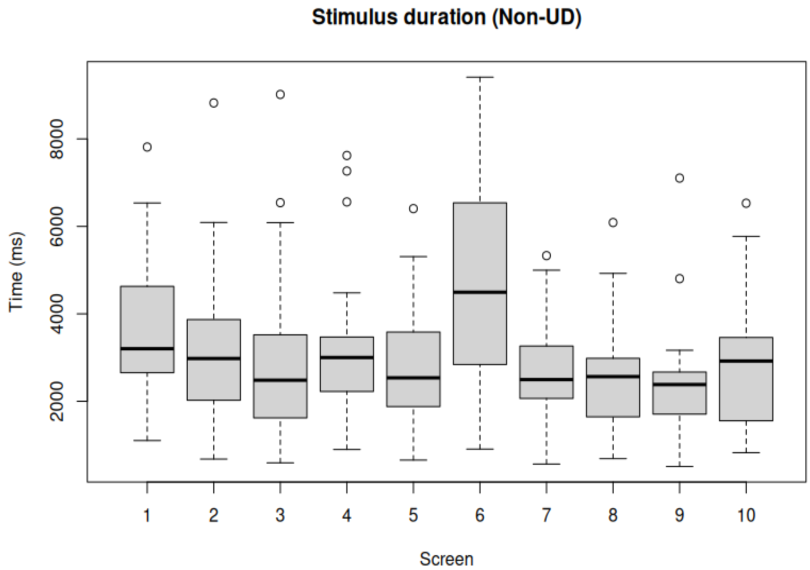

Fig. 15. Duration of fixations – element placement on the website without UD

5.4. LUT checklist

The results obtained using the LUT questionnaire were subjected to a statistical analysis, i.e. calculation of the mean, standard deviation, variance and the Levene's test. The results of the analysis are presented in Tab. 11.

Tab. 11. LUT checklist results – contrast, size and placements of website elements

Participant	WUP score of the UD-enabled	No-UD service with contrast	UD-enabled service with	No-UD service with placement
1	4.382	2.902	4.967	2.532
2	4.5	2.902	4.86	2.67
3	4.42	2.841	4.86	2.35
4	4.348	2.896	4.833	3.897
5	4.31	2.94	4.872	3.107
6	4.35	2.893	4.507	3.052
7	4.368	2.86	4.727	1.476
8	4.265	2.87	4.983	1.316
9	4.397	2.908	4.605	1.557
10	4.543	2.905	4.668	2.472
Mean	4.388	2.892	4.788	2.443
Std. dev.	0.083	0.0028	0.815	0.156
Variance	0.007	0.001	0.665	0.024
Levene's test		0.045		0.0081

In Levene's tests for all studies, the result indicated heterogeneity of variance (*p* value ≤0.05).

5.5. WAVE – the validator for automatic evaluation of web interfaces

The results of the study with the WAVE evaluation tool are graphically represented by pie charts in Figures 16 and 17.

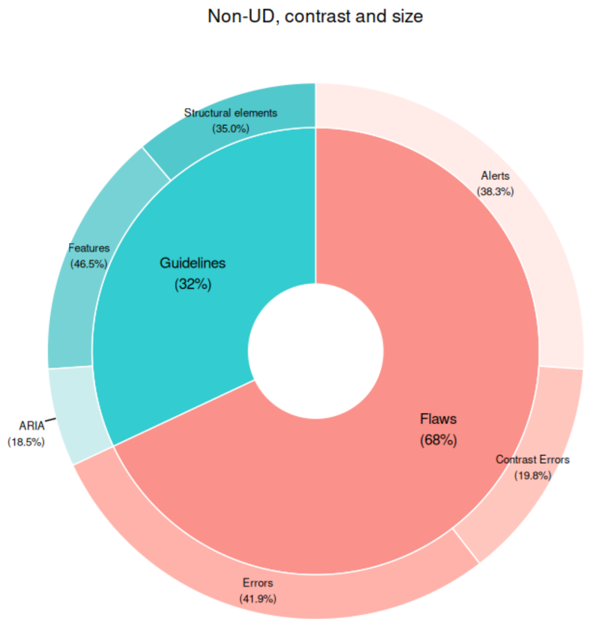

Fig. 16. WAVE analysis results chart – contrast and size of website elements without UD

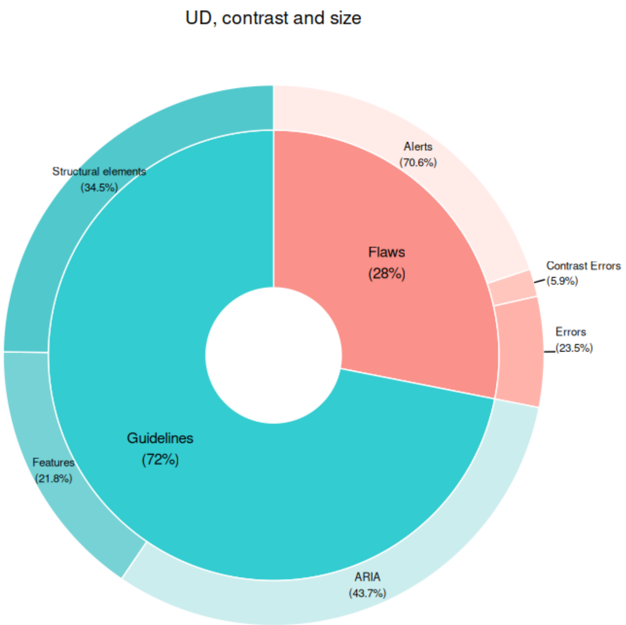

Fig. 17. WAVE analysis results chart – contrast and size of website elements with UD

6. DISCUSSION AND CONCLUSIONS

Based on the collected results of the statistical analysis, it was found that the results of the research proved the correctness of the hypotheses: "an information service limited by access barriers for people with visual impairment is worse perceived and more difficult to use than a fully accessible service" and "websites made in accordance with generally accepted principles and the universal design guidelines are more intuitive to use”.

The average time to search for an element, the duration of the eye fixation and the number of fixations on the views of websites designed according to the universal design guidelines was significantly lower by 93%, 342% and 114%, respectively (Tabs. 3-10). This indicates that the user was able to locate the selected GUI element much faster, and thus the website was easier to use and more intuitive.

The WUP indicator of the LUT checklist confirms that particular areas of websites with universal design are more useful than those that do not support these principles. In the sub-areas concerning layout and colour selection, the mean of the results was respectively higher by 80% and 137% for both websites created in accordance with universal design (Tab. 11). The smallest differences were in the areas related to entering data and forms, at the level of 34% and 72%, respectively. The participants indicate better intuitiveness, readability and accessibility of websites compliant with WCAG 2.0 standards.

Websites commonly used show a higher number of structural errors and contrast with the use of the WAVE tool (3766% and 5350%, respectively). Moreover, the ratio of errors to guidelines on the created website supporting the principles of universal design is clearly lower than on the website that does not comply with the above principles (Figs. 16, 17).

The conducted 3-element analysis confirmed that taking into consideration the principles of universal design while creating websites improves their intuitiveness, usability and accessibility. The application becomes available to a wide range of users, also to people with disabilities, e.g., with visual impairment.

The results of the research are complied with the results obtained in the analyzed literature (Acosta-Vargas et al., 2018; Ismail et al., 2020; Pivetta et al., 2013). They clearly indicate the lack of correct implementation of universal design guidelines on many popular websites.

Acknowledgments

This study has been conducted as part of the “Lublin University of Technology – Universal Design” project, funded by the European Social Fund under the PO WER program. Grant Agreement No. POWR.03.05.00-00-PU32/19-00.

The research programme titled “Usability and ergonomics of interfaces study”, was approved by the Commission for Research Ethics, No. 9/2019 dated. 27.05.2019.

Conflicts of Interest

The authors declare that they have no conflict of interest.

REFERENCES

Abascal, J., Arrue, M., & Valencia, X. (2019). Tools for Web Accessibility Evaluation. In Y. Yesilada & S. Harper (Eds.), *Web Accessibility. Human–Computer Interaction Series* (pp. 479–503). Springer, London. https://doi.org/10.1007/978-1-4471-7440-0_26

Acosta-Vargas, P., Acosta, T., & Luján-Mora, S. (2018). Challenges to Assess Accessibility in Higher Education Websites: A Comparative Study of Latin America Universities. *IEEE Access*, *6*, 36500–36508. https://doi.org/10.1109/ACCESS.2018.2848978

Alonso-Virgós, L., Espada, J. P., Thomaschewski, J., & Crespo, R. G. (2020). Test usability guidelines and follow conventions. Useful recommendations from web developers. *Computer Standards & Interfaces*, *70*, 103423. https://doi.org/10.1016/j.csi.2020.103423

Centre for Excellence in Universal Design. (n.d.). *What is Universal Design*. Retrieved May 20, 2022, from https://universaldesign.ie/what-is-universal-design/

Digital Around the World. (n.d.). *DataReportal – Global Digital Insights*. Retrieved May 19, 2022, from https://datareportal.com/global-digital-overview

Fogli, D., Provenza, L., & Bernareggi, C. (2014). A Universal Design Resource for Rich Internet Applications based on Design Patterns. *Universal Access in the Information Society*, *13*, 205–226. https://doi.org/10.1007/s10209-013-0291-6

GP3 HD Eye-Tracking Device – Take Advantage Of Research-Grade Equipment. (n.d.). *Gazepoint*. Retrieved May 20, 2022, from https://www.gazept.com/product/gp3hd/

Grobelny, J., Jach, K., Kuliński, M., & Michalski, R. (2006). Śledzenie wzroku w badaniach jakości użytkowej oprogramowania. *Historia i mierniki*. https://repin.pjwstk.edu.pl/xmlui/handle/186319/166

Harper, S., & Chen, A. Q. (2012). Web accessibility guidelines. *World Wide Web*, *15*(1), 61–88. https://doi.org/10.1007/s11280-011-0130-8

iMotions: Unpack Human Behavior. (n.d.). *Imotions*. Retrieved 20 May 2022, from https://imotions.com/

Initiative (WAI), W3C Web Accessibility. (n.d.). *Web Accessibility Initiative (WAI)*. Retrieved May 20, 2022, from https://www.w3.org/WAI/

Isa, W. A. R. W. M., Suhaimi, A. I. H., Ariffrn, N., Ishak, N. F., & Ralim, N. M. (2016). Accessibility evaluation using Web Content Accessibility Guidelines (WCAG) 2.0. In 2*016 4th International Conference on User Science and Engineering (i-USEr)* (pp. 1–4). IEEE. https://doi.org/10.1109/IUSER.2016.7857924

Ismail, A., Kuppusamy, K. S., & Paiva, S. (2020). Accessibility analysis of higher education institution websites of Portugal. *Universal Access in the Information Society*, *19*(3), 685–700. https://doi.org/10.1007/s10209-019-00653-2

Just, M. A., & Carpenter, P. A. (1976). Eye fixations and cognitive processes. *Cognitive Psychology*, *8*(4), 441–480. https://doi.org/10.1016/0010-0285(76)90015-3

Kumar, S., Shree DV, J., & Biswas, P. (2021). Comparing ten WCAG tools for accessibility evaluation of websites. *Technology and Disability*, *33*(3), 163–185. https://doi.org/10.3233/TAD-210329

Leszczyńska, E. (2019). *Polacy w sieci: Analiza przemian użytkowania Internetu*. Wydawnictwo Uniwersytetu Marii Curie-Skłodowskiej.

Michalska, A. M., You, C. X., Nicolini, A. M., Ippolito, V. J., & Fink, W. (2014). Accessible Web Page Design for the Visually Impaired: A Case Study. *International Journal of Human-Computer Interaction*, *30*, 995–1002. https://doi.org/10.1080/10447318.2014.925771

Miłosz, M. (2014). *Ergonomia systemów informatycznych*. Politechnika Lubelska.

Narzędzie do blogowania, platforma wydawnicza i system zarządzania treścią witryny (n.d.). *WordPress.org Polska*. Retrieved May 20, 2022, from https://pl.wordpress.org

Pascual, A., Ribera, M., Granollers, T., & Coiduras, J. L. (2014). Impact of Accessibility Barriers on the Mood of Blind, Low-vision and Sighted Users. *Procedia Computer Science*, *27*, 431–440. https://doi.org/10.1016/j.procs.2014.02.047

Pivetta, E. M., Flor, C., Saito, D. S., & Ulbricht, V. R. (2013). Analysis of an Automatic Accessibility Evaluator to Validate a Virtual and Authenticated Environment. *International Journal of Advanced Computer Science and Applications*, *4(*4), Article 4. https://doi.org/10.14569/IJACSA.2013.040403

Sanderson, N., Chen, W., & Kessel, S. (2015). The Accessibility of Web-Based Media Services – An Evaluation. In M. Antona & C. Stephanidis (Eds.), *Universal Access in Human-Computer Interaction. Access to Today's Technologies. UAHCI 2015. Lecture Notes in Computer Science* (9175, pp. 242-252). Springer. https://doi.org/10.1007/978-3-319-20678-3_24

Stasiak, W., & Dzieńkowski, M. (2021). Accessibility assessment of selected university websites. *Journal of Computer Sciences Institute*, *19*, 81–88. https://doi.org/10.35784/jcsi.2462

TVP Info. (n.d.). *TVP Info*. Retrieved May 20, 2022, from https://www.tvp.info

WAVE Web Accessibility Evaluation Tool. (n.d.). *WAVE Web Accessibility Evaluation Tool*. Retrieved May 20, 2022, from https://wave.webaim.org

Web Content Accessibility Guidelines (WCAG) 2.1. (n.d.). *World Wide Web Consortium*. Retrieved May 20, 2022, from https://www.w3.org/TR/WCAG

Yoon, K., Dols, R., Hulscher, L., & Newberry, T. (2016). An exploratory study of library website accessibility for visually impaired users. *Library & Information Science Research*, *38*(3), 250–258. https://doi.org/10.1016/j.lisr.2016.08.006

Applied Computer Science, vol. 18, no. 3, pp. 86–104
doi: 10.35784/acs-2022-23

Submitted: 2022-06-15 | Revised: 2022-08-17 | Accepted: 2022-09-24

Keywords: Computational Fluid Dynamics, PM Pollution, Propeller Aerodynamics, Multi-rotor Robot Design

Grzegorz SUCHANEK [0000-0003-0294-3574]*, *Roman FILIPEK* [0000-0003-4763-023X]**

COMPUTATIONAL FLUID DYNAMICS (CFD) AIDED DESIGN OF A MULTI-ROTOR FLYING ROBOT FOR LOCATING SOURCES OF PARTICULATE MATTER POLLUTION

Abstract

The use of flying robots for various environmental protection issues is a very important and current research topic. Designing a dedicated multi-rotor flying robot is necessary for the efficient and automated localization of sources of air pollution, especially solid particles. In particular, one of the most important requirements that must be met by such a robot is its appropriate impact on the measurement process, i.e., increasing the sensitivity of sensors or reducing the interference. This is particularly difficult because its rotating rotors introduce significant disturbances to the surrounding fluid. In these studies, the design process is supported by the creation of a mathematical flow model and a series of analyzes to optimize the PM measurement system. The model is built using the finite-volume method in ANSYS Fluent software and steady-state RANS averaging. First, a flow field model with one propeller was modeled and its parameters identified by comparison with the results from the dedicated original dynamometer stand -- characteristics of the propeller performance. On the basis of the simulations and measurement of one rotor, subsequent systems of the highest practical importance are built. The effect of that design process was the preparation and testing of a functional robot prototype. The field parameter distributions resulting from the analyzes, in particular the turbulence intensity, allow one to propose a criterion on the basis of which both the best rotor configuration and localization of sensors are selected.

1. INTRODUCTION

Human health and life, especially under urban conditions, are constantly exposed to the adverse effects of polluted air. It is responsible for the prevalence of various types of allergies or other diseases, including cancer. Decaying building facades can also be included here as less obvious environmental damages. High concentrations of solid particles pose

* AGH University of Science and Technology, Faculty of Mechanical Engineering and Robotics, Department of Power Systems and Environmental Protection Facilities, Krakow, Poland, suchanek@agh.edu.pl
** AGH University of Science and Technology, Faculty of Mechanical Engineering and Robotics, Department of Power Systems and Environmental Protection Facilities, Krakow, Poland, roman.filipek@agh.edu.pl

a particular threat. Therefore, there is a constant need to find and develop solutions that would allow to locate the sources of this type of pollution. The sources of this type include, among others, wildfires or other processes in which low-quality fuels or waste are incinerated.

Particle concentration data collection methods can be mainly divided into stationary or mobile methods. Stationary methods use a fixed measurement grid, which are stationary meteorological stations. However, nowadays the most important are mobile methods utilizing flying robots, in particular multi-rotor robots. The use of such a robot requires complex analysis, as rotating rotors of a multirotor robot during operation introduce a large disturbance into the natural field of air flow and gases that carry the particulate matter, thus disrupting the process of their measurement.

Measurements can be made directly during flight when the robot is equipped with appropriate sensors. However, that approach is limited only to the capabilities of usually low-cost, lightweight sensors that can be mounted on the robot. In cases where the robot's task is to locate the source of the pollution, the accuracy of the sensor is less important. The other option is to build robots where the robot is not equipped with an analyzer but with an air sampling system. The air is taken into special tanks or bags, and the composition analysis is carried out on the ground after landing. An example of such work can be (Chen et al., 2018; Cheng et al., 2019). An air intake system (Cheng et al., 2019), dedicated to the extraction of volatile organic compounds (VOCs), has been attached to a telescopic shaft to keep the system inlet away from the powerful air flow from the propellers. In this case, a measuring system was used in the form of a special thin tube (needle trap sampler). It has been shown to be a better solution than a stainless-steel air tank or teflon bags. The results were verified under controlled conditions. The optimal inlet location was determined using *SolidWorks* software. The work (Dieu Hien et al., 2019) presents an overview of the available methods for sampling volatile organic compounds. These solutions eliminate the problems of low accuracy of sensors placed directly on the robot. Due to the desirable features of low empty weight, such sensors do not have measurement properties similar to stationary devices used in laboratories. However, in this case, it is not possible for the robot to use the data on an ongoing basis, and thus, i.e., automatic locating the sources of maximum pollution concentration (Suchanek, Wołoszyn & Gołaś, 2022).

Measurements of solid particles using multirotor robots have been described in many articles (Chiang et al., 2020, Chang; Chen & Huang, 2018; Landolsi et al., 2018). More advanced studies are: (Wang, 2019) where the vertical profile, incl. $PM_{2.5}$ particles and O_3 ozone were determined at heights up to 140 m (Mayuga et al., 2018), where the measurements carried out in the city during heavy traffic with the use of a quadcopter robot were presented. A simple recorder based on the Arduino platform was mounted under the robot, equipped with a: temperature, humidity, and a particulate matter sensor. In (Chunithipaisan et al., 2018) a similar simple system is presented, also based on the Arduino platform. Three-dimensional graphs of measured values for exemplary flights are presented. In the work (Gu, Michanowicz & Jia, 2018) a modular system was proposed, and sample measurements of PM2.5 and NO_2 were presented. The purpose of the study (Alvarado et al., 2017) was to develop a methodology to monitor PM10 dust particles produced as a result of mining activities. An aerodynamic experiment was carried out in which the robot was placed on a 2.5 m high pole and measurements were made using an anemometer. On the basis of the measurements, a three-dimensional map of the air flow around the robot was generated, and it was decided to place the measurement system inlet on the raised platform, about 50 cm above the robot. An analysis of the optimal hover time is also presented. Too short time (and therefore measurement) is undesirable as it increases the measurement errors. On the other hand, too long time reduces the number of possible measuring points. The article (Villa et al., 2016) presents a similar study in which air flow around a hexacopter robot was investigated. The tests were carried out using a manual anemometer, the position of which was tracked by the *VICON* system (Vicon Motion System Ltd., Oxford, UK). This system allows tracking and locate the position and orientation of an object in a room. In addition to the particle detector, the use of CO_2, CO, NO_2, NO gas sensors were also assessed to evaluate the possible performance of a robot-based flying measurement system of diesel engine emissions. On the basis of the conducted research, some design guidelines were indicated, including: the best solution is to mount the sensors on the extended arm at a distance of about 1–1.2 m from the robot's center, and the propellers cause a thinning effect, which manifests itself as a decrease in the gas concentration indicated by sensors mounted closer to the center of the robot.

The study (Wang et al., 2020) focused on the analysis and determination of the vertical profile of the distribution of solid particles. The six-rotor robot was equipped with a *AM510* $PM_{2.5}$ sensor. Measurements were made at heights of up to 1000m. The advantages and disadvantages of various measurement methods of particulate matter, such as ground station, meteorological tower, tethered balloon, ground *LiDAR*, satellite remote sensing, as well as manned and unmanned aerial vehicles, are also discussed. In the case of an unmanned vessel, it is necessary to take appropriate safety measures by avoiding airport zones and crowded communities and avoiding measurements in extreme weather conditions. Measurements were made at several different times of the day. The influence of temperature and humidity on the vertical distribution of solid particles is also discussed. Attention was paid to the problem of verifying the accuracy of measurements made with the use of a flying robot, therefore comparative measurements were carried out with a tethered balloon. It was indicated that it is necessary to reduce the influence of turbulent flow around the robot by appropriate localization of the inlet of the measuring system.

The work aimed at analyzing and describing the air movement around the robot includes (Burgués et al., 2019), presenting a small commercial *Crazyflie 2.0* nanoquadrocopter, weighing only 27 g. The use of such a robot is therefore limited to closed rooms and low wind speeds. The work shows visualization of aerodynamic phenomena around the robot in the wind tunnel. The work (Ni et al., 2017) concerns the monitoring of crops using a multi-rotor robot. For this purpose, advanced research was performed in the *ANSYS* environment of the *Phantom* commercial robot from *DJI*. Both the propeller and the entire robot were scanned with a 3D scanner. A non-structural mesh was used for the analysis. Based on the results obtained, it was established that two multispectral sensors of crop growth should be placed at the ends of a 1.5 m symmetrical extended arm. The measurement data are analyzed at the ground station. The paper (Luo et al., 2016) presents a numerical model for dynamic simulation of dispersion under the influence of propeller motion. The study (Smith et al., 2016) uses smoke to visualize the aerodynamic phenomena around a robot with four rotors. (Nagy & Jahn, 2019) uses the approach of placing the sensors on a symmetrical boom. A commercial robot and a self-built measuring system are used to measure wind farms.

The paper (Parra et al., 2018) analyzes the aerodynamic disturbances caused by the operation of a six-rotor robot equipped with propellers with two or four blades. However, the work did not analyze the forces, torques, or power generated for the options analyzed. Preliminary research, where the CFD model was verified on the basis of measurements on the dynamometer stand were presented in (Ciesielka & Suchanek, 2019). In this paper, modelling and simulation of the robot prototype with four rotors were also carried out. The work (Faraz et al., 2020) modeled the flow field around a robot with four rotors. In the tests, the generated thrust force of the robot's propeller was determined for different rotational speeds of the rotor, which allowed the determination of an unknown rotor thrust constant. Based on the research, it was found that the analyzed propeller is able to generate the necessary thrust to lift the robot and can withstand a dynamic load without failure. However, the research conducted was not compared with the data from the experiment.

The article (Hutchinson, Liu & Chen, 2019) generally summarizes the problems of optimal placement of the measuring system, i.e., the influence of the rotors on the dispersion of the measured gas concentration and the overall operation of the sensors. As mentioned above, as well as in this article, it was indicated that this effect was taken into account and various studies were carried out in order to determine the optimal position for the measuring system. Various solutions were considered: under the rotors of the robot, in its center, either elevated above or below the platform, between the rotors, or on the boom. As the authors point out, on the basis of simulations *CFD*, smoke visualizations or pressure and flow measurements on the rotors carried out in various studies, certain conclusions can be drawn, despite contradictory results. The general consensus is that the robot has a negative influence on the measuring system: the results of gas concentration measurements are underestimated and their uncertainty increases. The most accurate measurements can be obtained from a sensor located outside of the area disturbed by the rotors; however, this may cause problems with the stability of the platform during flight. The panacea may be a pumped metering system with input outside the platform, but this also increases the weight of the platform. Therefore, the most common practice in the literature is to place the measuring system centrally, elevated above the robot, as was done in this work. Given the large increase in interest in gas detection applications and research with flying robots, the authors predict that the specially designed new sensors will bring significant benefits and will be an important area for future research.

Based on the examples cited, some research gaps can be identified, related to, i.e., the analysis of a single robot configuration and no experimental verification of the calculations made (model calibration). Other deficiencies are related to the analysis of commercial robot solutions, which, due to their design, cannot easily integrate a measurement system for the purpose of automatically searching for the source of pollution. In cases where the sensor is placed over the robot, there are difficulties in measuring when the robot is hovering over a source of pollution. Particulate matter was also not taken into account in the simulation tests.

The aim of the work was to model the aerodynamic field around the rotors of selected types of flying robots. On this basis, the disturbance of the natural flow field caused by the rotors was estimated. Estimation allows the correct design of the particulate measurement system to search for the source of contamination. Performing such an analysis is necessary for the robot to fulfill its assigned function of locating sources of pollution. The CFD simulations were verified on a constructed dedicated dynamometer stand. As a result of this design process, the best rotor configuration and localization of sensors were selected and then a functional drone prototype for locating pollution sources was prepared and tested.

2. COMPUTATIONAL MODELS

The subjects of the analysis were configurations with one, two, four and finally six rotors (Fig. 1). The single rotor configuration was used to validate the simulations. The results of this model were compared with the data from the experiment. The two-rotor configuration is one arm of the octocopter, a quadrocopter with two rotors on each arm. The four and six rotor systems were directly related to the types of flying robots analyzed: quadro- and hexacopter. These are the robot configurations of the greatest practical importance. For these configurations, computational models of the flow field were built and then the velocity, pressure, and turbulence field distributions were determined. Aerodynamic phenomena around the robot rotors were analyzed in dedicated *ANSYS Fluent* fluid flow software.

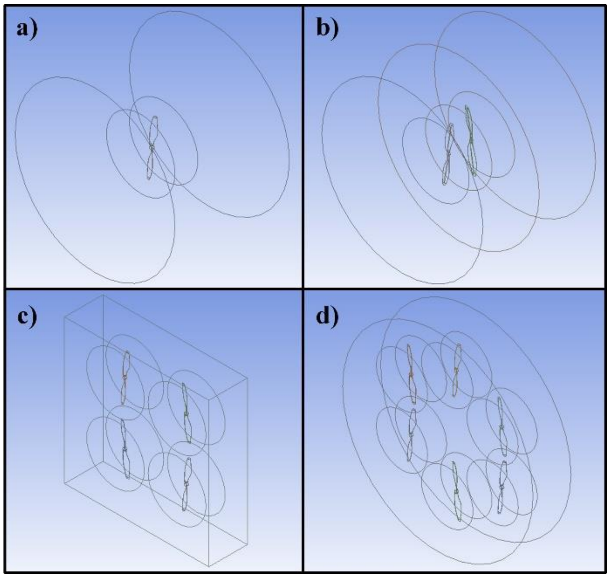

Fig. 1. Geometric models of the analyzed rotor configurations: a) one, b) two, c) four, d) six rotors

The first of the models constructed contained a single rotor (Fig. 1a). Two propellers used in the described robots were analyzed: the smaller type 1045 (10 inch diameter and 4.5 inch pitch) and the larger type 1238 (12 inch diameter and 3.8 inch pitch). The rotational speeds assumed for the calculations corresponded to the operating conditions of the discussed multirotor robots. The computational domain for these cases has the shape of a cylinder with the following dimensions: for a propeller 1045 with a diameter of 0.7 m and a height of 0.5 m, for a larger one with a diameter of 0.8 m and a height of 0.6 m. These models were verified on the basis of experimental data from a constructed dynamometer stand.

With a single-rotor model verified, it was possible to model systems with a greater number of them. The first of the more complex models was a dual-rotor system from an octocopter. This robot is in a redundant configuration, which means that it has four arms, and there are two sets of drives per arm, the top and bottom one. The total weight of this robot is 4.3 kg and is equipped with a 1238 propeller. Due to the large external dimensions and the resulting high computational complexity, it was decided to perform an analysis for the counter-rotating configuration of the two propellers, as shown in Figure 1b. For this purpose, it was necessary to create two dynamic zones above each other, in the shape of a cylinder with a diameter of 0.36 m and a height of 0.12 m. Dynamic zones rotate at identical speeds but in opposite directions. The surroundings are a static zone, which is cylindrical in shape, 0.8 m in diameter and 0.6 m in height.

Another of the robots analyzed is a quadcopter robot equipped with four rotors, one for each arm. This robot is equipped with 1045 propellers and weighs 1.35 kg. The prepared geometrical model (Figure 1c) contains four cylindrical revolving zones with a diameter of 0.3 m and a height of 0.1 m. The robot environment is a static rectangular zone with dimensions of 0.75 m × 0.75 m × 0.2 m. The construction of the hexacopter robot (Figure 1d) is very similar. It is equipped with the same type of propeller; therefore, the same dynamic zones are adopted. Additional rotors are included, and in this case, the static zone is cylindrical in shape, 1m in diameter, and 0.2 m in height. The robot weighs 2.54 kg. In cases where a configuration of four or six rotor numbers was modeled, the prepared model covered only the closest robot environment. This is due to the fact that the arm of the measuring system must not be too far from the center of gravity of the robot, as this would significantly deteriorate the stability of the robot in the air.

First, a geometric model of the rotor (propeller) was built. In this case, the work began with 3D scans of the two described propellers. The following description of the model building process refers to a single small (1045) propeller system. Subsequent systems with a larger number of rotors were constructed in the same way. As a result of the scanning process, a file is obtained in the polygonal mesh format (STL). Such a file is not suitable for further calculations, as a solid-format model is required. Software *CATIA* was used for this task. The next step was to prepare a geometric model of the environment in which the rotor will operate. The propeller was placed in a cylinder with a diameter of 0.3 m and a height of 0.1 m. Then another cylinder, 0.7 m in diameter and 0.5 m in height, was created. A large cylinder without the volume of a small cylinder is hereinafter referred to as the static (stationary) zone. The second domain is a small cylinder without the volume of the propeller body, hereinafter referred to as the dynamic (rotational) zone.

The next step was to prepare the computational mesh. Due to the complex geometry of the propeller's body, a non-structural, non-conformal mesh was prepared. The non-structural mesh is generated automatically by the software based on defined guidelines. In particular, it was established that the element size in the revolving zone should not exceed 0.003 m (Figure 2b), and in the static 0.01 m (Figure 2a). The non-conformal mesh type means that the consistency of the mesh nodes at the domain boundaries was not guaranteed, which was difficult in the case of complex geometries and multi-rotor configurations. Additionally, in order for the modeled aerodynamic phenomena near the rotor to be considered correct, it is required that, as a result of calculations, the dimensionless distance from the wall on the rotor surface must be less than 1 over the rotor surface. This parameter of the dimensionless distance from the wall, which is determined during the modeling of flows in the vicinity of rigid walls, is called y^+. To obtain y^+ at a certain level, an additional boundary layer should be modeled. This goal is achieved by local mesh refinement (as shown in Fig. 2c) on the wall surface (here: rotor surface). The following parameters are determined: the height of the first boundary layer y, the inflation ratio, that is, the degree of increase in the height of subsequent layers, and the number of these layers. On the basis of analytical calculations, the height of the first boundary layer y was assumed to be approximately 0.006 mm. Eight boundary layers for the rotor were assumed and the inflation ratio was assumed to be 1.2. As discussed above, it denotes the scale of growth of successive layers, starting from the boundary layer. The number of all elements in the mesh (Figure 2a) was approximately 4.4 million. Other cases were prepared in the same way, and the numbers of elements in the remaining cases were: single 1238 propeller 9.5 mln, two 1238 propellers 16.3 mln, four 1045 propellers 11.4 mln and six 1045 propellers 15.3 mln. For that mesh, the maximum value of y^+ on the rotor surface was approximately 0.74. The parameters of the grid prepared in this way were acceptable, i.a. the maximum skewness was less than 0.8. Elements with a skewness above 0.5 constituted only about 3% of all elements, which were 6 node wedges elements mostly.

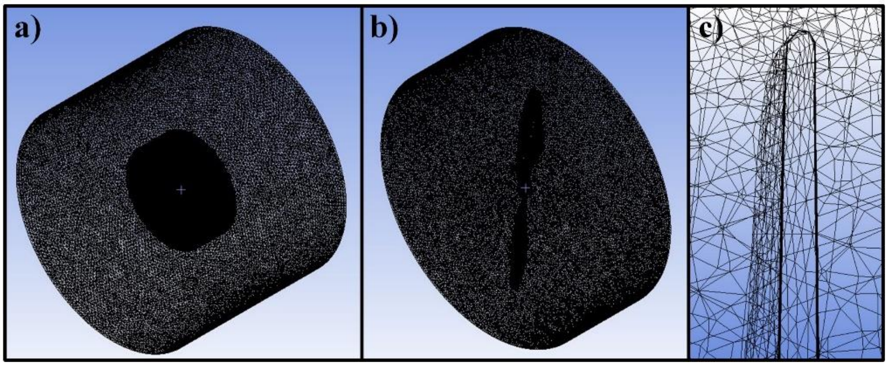

Fig. 2. Prepared mesh for the configuration with one rotor: a) whole domain, b) dynamic zone, c) close-up on the rotor boundary layer

Then the input data for the *Fluent* software was prepared, which was used to calculate the solution. In particular, the boundary conditions have been defined. The adopted boundary conditions for a configuration with one rotor are presented in Figure 3.

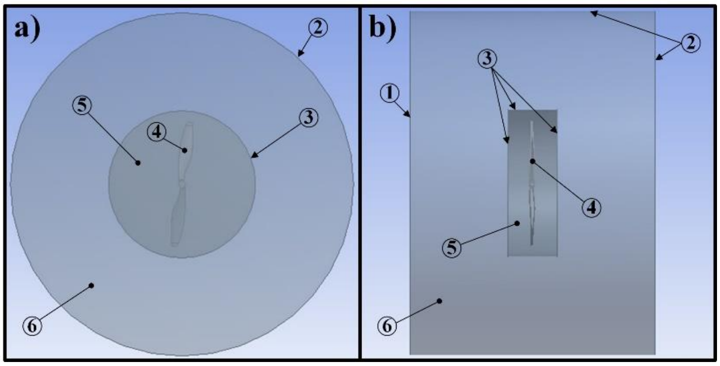

Fig. 3. Boundary conditions: a) top view, b) side view. Symbols in the drawing: 1 – *pressure-inlet* (inlet), 2 – *pressure-outlet* (outlet), 3 – *interface* (domains contact surfaces), 4 – *rotating-wall* (the surface of the propeller rigid body), 5 – dynamic zone, 6 – static zone

The upper plane (1) of the static zone cylinder (6) was defined as of *pressure-inlet* type. On the other hand, the bottom and side surfaces (2) were defined as *pressure-outlet*. The inner contact surfaces of the domain's *interfaces* (3) define the way in which the dynamic

(5) and static (6) zones interfere, that is, they define the domain contact. The propeller body itself (4) is rigid and rotates together with the rotating domain (5), so it is of the *rotating-wall* type. In addition, the axis of rotation and the rotational speed of the dynamic zone were also defined.

ANSYS Fluent solves the flow equations on a stationary frame of reference. A system with one or more rotating rotors, however, belongs to a group of problems for which it is advantageous, or even necessary, to solve equations in a non-inertial frame of reference. After activating the moving frame of reference for each of the modeled rotors of the system, the software modifies the equations of motion to consider the additional terms of acceleration that occur due to the transformation from stationary to moving frame of reference. In simulated multi-domain cases, it is required to specify the domain contact surfaces as interfaces. The interface definition method leads to two approximate steady-state modeling methods; these are the mixing plane model (MPM) or the multiple reference frame (MRF) approach used in this case. The MRF model is a steady-state approximation in which specific rotational speeds are assigned to each rotational zone. The flow in each moving zone is solved using the equations of the moving coordinate system. A local coordinate system transformation is performed at the interfaces between the rotating and stationary zones to allow the flow parameters in one zone to calculate flows at the boundary of an adjacent zone. In the case of a single-rotor system, it is possible to define the entire domain as rotating without separate division into rotating and static parts. This variant is known as a single reference frame (SRF) approach. However, because this work analyzed different rotor systems rotating at different rotational speeds, this approach was not used. When the equations of motion are solved in a moving frame of reference, additional conditions that appear in the momentum equations are considered to determine the acceleration of the fluid. In this case, the equations are formulated by expressing the momentum equations using absolute speeds as dependent variables in the momentum equations, which is known as absolute velocity formulation. It is also possible to use the frozen-rotor approach (Tulwin, 2019), where interfaces are also not used. However, the MRF model, although more complicated, allows easy use of the sliding-mesh (SM) method in the future. It is a more accurate method for high rotational speeds.

ANSYS Fluent (Ansys Fluent Theory Guide, 2020) solves the Navier-Stokes partial differential equations resulting from the principle of conservation of mass and momentum. If the flow is turbulent, additional transport equations are added. The mass conservation equation is written in a generalized form as follows:

$$\frac{\partial \rho}{\partial t} + \nabla \cdot (\rho \vec{u}) = S_m \tag{1}$$

where: ρ is the fluid density, $\vec{u}$ is the velocity, and S_m is the mass source. The conservation of momentum principle for a stationary frame of reference is described (Batchelor, 1967) by:

$$\frac{\partial}{\partial t}(\rho \vec{u}) + (\rho \vec{u} \cdot \nabla)\vec{u} = -\nabla p + \nabla \cdot \left(\overline{\overline{\tau}}\right) + \rho \vec{g} + \vec{F} \tag{2}$$

where: p is the static pressure and $\rho \vec{g}$ and $\vec{F}$ are the gravitational force and external forces, respectively. The stress tensor $\overline{\overline{\tau}}$ is given by:

$$\bar{\bar{\tau}} = \mu\left[\left(\nabla\vec{u} + \nabla\overrightarrow{u^T}\right) - \frac{2}{3}\nabla\cdot\vec{u}I\right] \tag{3}$$

where: μ is the kinetic viscosity, I is the unit tensor, and the second term on the right describes the volume dilation effect. This paper introduces simplifications regarding the lack of mass sources ($S_m = 0$), the lack of external forces ($F = 0$) and the constant fluid density ($\rho = const$), which simplify equations (1) and (2) in the form:

$$\nabla\cdot\vec{u} = 0 \tag{4}$$

$$\rho\left[\frac{\partial\vec{u}}{\partial t} + (\vec{u}\cdot\nabla)\vec{u}\right] = -\nabla p + \nabla\cdot\left(\bar{\bar{\tau}}\right) + \rho\vec{g} \tag{5}$$

Due to the necessity of solving these equations numerically, the finite-volume method, namely its RANS variant (Reynolds-Averaged Navier-Stokes), was used to determine the approximate solution. In this method, the solution variables in instantaneous (exact) Navier-Stokes equations are broken down into mean components (averaged in space or averaged over time) and unaveraged variables. For velocity u and scalar parameters ϕ this can be written as:

$$u_i(x_i,t) = \overline{u}_i(x_i) + u_i'(x_i,t), \quad \phi(x_i,t) = \overline{\phi}(x_i) + \phi'(x_i,t) \tag{6}$$

where: $\bar{u}_i$ and u_i' are respectively the mean and time-varying velocity components in three directions ($i = 1,2,3$), and $\overline{\phi}$ and ϕ' are the mean and time-varying components of scalar quantities such as pressure, energy or intensity. The turbulence intensity is a very useful metric for characterizing turbulence and is defined as the ratio of the root mean square of the velocity fluctuations to the mean flow velocity (Rodriguez, 2019). If the turbulent energy *k* is known the turbulence intensity can be computed on its basis (Ansys Fluent Theory Guide, 2020).

The standard model of *k-ω* in *Ansys Fluent* (Ansys Fluent Theory Guide, 2020; Romik & Czajka, 2022) is based on the model proposed by Wilcox (Wilcox, 2006), which is an empirical model based on the equations of transport of the kinetic energy of turbulence (*k*) and the specific dissipation rate (*ω*). Over the years, this model has been improved by adding production conditions to both equations, which has increased the accuracy of the prediction of free shear flow. The main problem with the Wilcox model is its well-known strong sensitivity to free-stream conditions. The base model *k-ω* (BSL) was developed by Menter (Menter, 1994) and contains different modeling constants. Its unique feature is that in its formulation, the standard *k-ω* model and the transformed *k-ϵ* model are multiplied by the blending function and both models are added together. The blending function is designed to be one in an area close to the wall, which activates the standard *k-ω* model, and zero away from the surface, which activates the transformed *k-ϵ* model. Another difference is that the BSL model includes a derivative of damped cross-diffusion in the equation. The Shear-Stress Transport (SST) *k-ω* model includes all the improvements to the BSL model and also includes the principal turbulent shear stress transport in the definition of turbulent viscosity. These characteristics make the SST model (Menter, 1994) more accurate and reliable for a wider class of flows, for example, with an unfavorable pressure gradient or around the airfoil, and make it definitely better for this study than the standard and BSL models.

The last stage of the work included performing the calculations and analysis of the data obtained. In general, if there are critical errors in the modeling and model definition phases, the calculations will not converge. This can be defined as the first necessary criterion for the correctness of the calculations. After satisfying this criterion, the parameters obtained on the rotor were checked next: the resulting torque and thrust force was compared with the data from the experiment. Comparison of the thrust forces and torques values is presented in the chapter on the calculation validation. The independence of the solution from the computational mesh was also examined.

3. EXPERIMENTAL VALIDATION OF SINGLE-ROTOR MODEL

To determine the unknown parameters of the selected drive sets, it turned out that it was necessary to design, build, and prepare software for a dedicated mobile dynamometer stand. The construction of the station allowed us to identify the drive unit that will be characterized by the highest thrust force achieved. Moreover, the data obtained made it possible to verify the mathematical model of the CFD. The prepared mobile measuring station enables the collection of data necessary to determine the characteristics of the drive sets of multi-rotor robots. A drive unit is understood as a complete set consisting of a propeller, a motor, and an engine speed controller (ESC). The following design assumptions were adopted for the constructed stand, i.e., that it will enable measurements of the thrust force and torque, the propeller rotational speed and the supply voltage and the current.

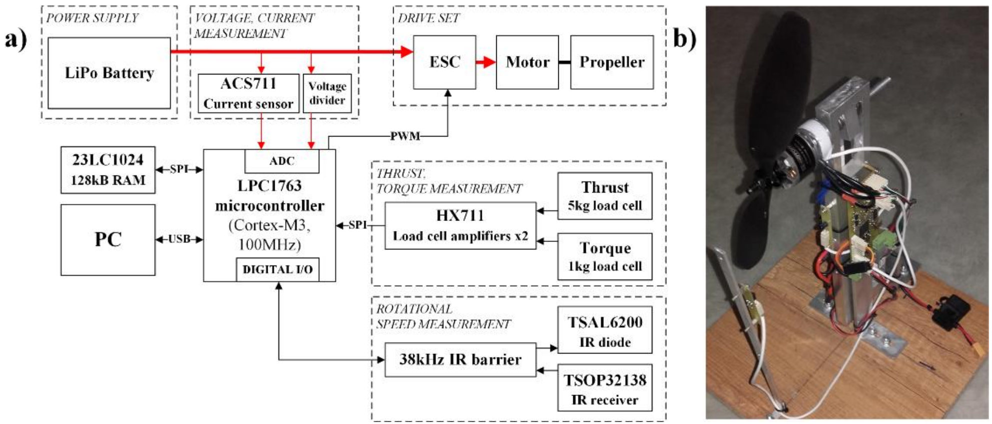

Fig. 4. Constructed dynamometer test stand: a) block diagram, b) view of the stand

The block diagram of the prepared dynamometer stand was presented in Figure 4a. The external dimensions of the entire stand (Figure 4b) are 0.3 m × 0.3 m × 0.34 m. The main control element of the electronic part of the system is the NXP LPC1763 microcontroller, which performs the measurement and control function of the entire stand. Dedicated 24bit HX711 digital scale amplifiers were used to amplify and digitize the weak signal from strain gauge beams. The motor current was measured using a ACS711 (25 A max) Hall effect current\voltage converter. Supply voltage measurements and voltage measurements from a current sensor were carried out using the microcontroller internal ADC converter. Measurement of the rotational speed of the propeller is carried out with the help of an optical barrier. The special structure of the barrier eliminates the influence of the flickering light sources present in the room on measuring the propeller rotation speed. The optical barrier can be mounted in three different positions, thus adjusting it to the size of the mounted propeller. Measurement data are stored in an additional 23LC1024, 128 kB RAM memory. The system can communicate with a PC using the integrated USB\UART converter. These were additional technical issues that ensured the integrity of the measurement data. The stand is equipped with additional necessary safety measures. It is possible to quickly disconnect the power in the events of the internal microcontroller or PC software crashing and loss of communication with the PC. All internal microcontroller software that manages low-level functions of the station was prepared in C language. The program was prepared at a low level to obtain the highest efficiency of collecting and processing measurement data. The PC-side software that cooperates with the station was prepared in C++.

The Gefman 1045 propeller was tested with the Emax MT2213 motor, a 30A Emax ESC with a LiPo 11.1V (3S) battery. The Gefman 1238 was tested with the Emax MT2814 motor, a 40A DYS ESC with a LiPo 14.8V (4S) battery. The batteries were fully charged before measurements. Other propellers of the same type were also examined, but the presented ones were characterized by the largest thrust.

The motor with a propeller, which shaft is rotating at ω, generates a torque of M and a thrust force F, while it draws the power of P. Both the thrust force F and the torque M generated are proportional to the square, and the power P to the cube of rotational speed (Glauert, 1935). Therefore, this can be expressed as the following equations:

$$F = k\omega^2, \quad M = b\omega^2, \quad P = p\omega^3 \tag{7}$$

where: k, b, p – thrust force, torque, and power constants, respectively. These are not usually given by the manufacturer, so they were designated on the prepared dynamometer stand. In cases where the robot moves at low speeds or a steady state is analyzed when the robot is in a hover state, the influence of additional factors, such as motor shaft inertia, can be omitted. Typically, for the propulsion of analyzed robots, a dedicated brushless DC motors with a small moment of rotor inertia are used.

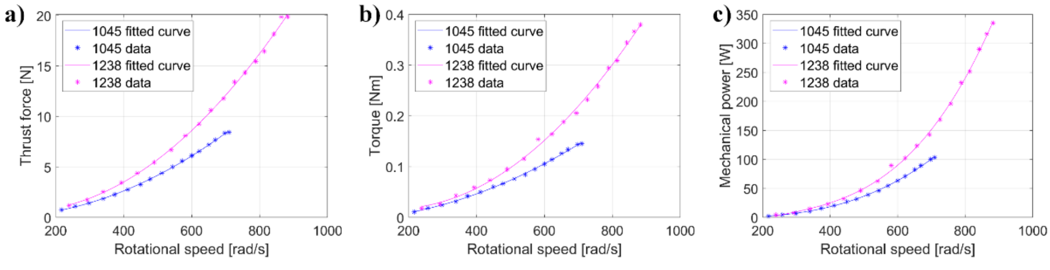

Fig. 5. Determined characteristics for both rotors: a) thrust force, b) torque, c) mechanical power

In Figure 5 the characteristics determined as a function of the rotational speed of the rotor are presented. Mechanical power was determined as the product of torque and rotor speed. On the basis of these data, a polynomial approximation could be performed, which was also presented in the chart. In the case of the thrust force and torque, a second-order polynomial was fitted, for power, the third order. The determination coefficient R^2 of these approximation functions exceeded 0.99.

On the basis of the experimental data, the CFD thrust forces and torques can be verified. The results obtained for all cases, along with the data from the experiment, are presented in Table 1. Obtaining similar results regarding these values for different meshes allowed us to state that the independence of the solution from the computational mesh was obtained.

Tab. 1. The CFD and experimental data for the single-rotor configurations analyzed

Rotor type	**1045**						**1238**		
Rotational speed [rad/s]	421.92			481.50			438.25		
	CFD	Exp.	Diff. [%]	CFD	Exp.	Diff. [%]	CFD	Exp.	Diff. [%]
Thrust force [N]	2.90	2.94	1.36	3.78	3.86	2.07	3.94	4.29	8.16
Torque [Nm]	0.047	0.052	9.62	0.061	0.068	10.29	0.061	0.071	14.08
Mechanical power [W]	19.83	21.79	9.00	29.37	32.67	10.10	26.73	33.17	19.42

As shown in Table 1, the differences between the data from the model and those from the experiment for a smaller rotor did not exceed about 10%. For a larger rotor it was around 19.5%, however, this was concerning mechanical power. For force and torque, these differences were approximately 8% and 14%, respectively. The sources of these differences can be sought primarily in: reproduction of the propeller model in the process of reverse engineering, determining engine parameters, or in general the numeric model itself. However, such small differences can be considered irrelevant, and the calculations were considered accurate enough. Moreover, the measured electric power, determined as the product of the supply voltage and current, confirmed the correct methodology of the mechanical power measurement. The estimated losses were considered in the validation.

4. COMPUTATIONAL RESULTS FROM MULTI-ROTOR MODELS

With a calibrated model for a single-rotor configuration, it was possible to verify the calculations for configurations with more than one rotor. First, the configuration with a single larger (1238) with the two rotors was compared. The results obtained were combined in Table 2. The following nomenclature was used here: *L* – left, *R* – right rotating propeller.

Tab. 2. Comparison of configurations with one and two rotors based on the CFD data

Configuration	**Single (L)**	**Dual**		
		Top (L)	Bottom (R)	Sum
Thrust force [N]	3.94	3.66	2.11	5.77
Torque [Nm]	-0.061	-0.060	0.050	-0.010
Mechanical power [W]	26.73	26.30	21.91	48.21

According to Table 2 it should be stated that the rotors working in the column generate unequal thrust forces and torques. When comparing the data with those of a single independent rotor, the top rotor in the column generates 93% of the force and 98% of the torque. For the bottom one, these amounted to only 53% and 81%, respectively. In other words, the bottom rotor generates only 37% of the total thrust force for the entire column. When it comes to the generated moment, it is 11% smaller for that rotor. This is primarily due to the fact that the bottom propeller is already powered by pre-accelerated air by the top one. In terms of power, the column requires approximately 90% of the power compared to two independent single rotors, generating a thrust force of 73% at the same time. The verification of the four- and six-rotor configuration was carried out in the same way. Due to the similarity of these cases, only the data for a six-rotor configuration will be presented. The results obtained are presented in Table 3.

Tab. 3. Thrust forces and torques of each rotor in the six-rotor configuration

Rotor	1 (L)	2 (R)	3 (L)	4 (R)	5 (L)	6 (R)	Sum
Thrust force [N]	3.36	3.38	3.40	3.43	3.38	3.39	20.34
Torque [Nm]	-0.058	0.058	-0.057	-0.058	-0.059	0.059	0.001

As presented in Table 3, both the thrust forces and the torques generated by each of the rotors are similar in value. Compared to a single-rotor system (3.78 N thrust force, 0.061 Nm torque), lower values were obtained. In the case of forces, the result was about 10% smaller, in the case of moments about 5% smaller. It is related to the mutual influence of the working rotors on each other.

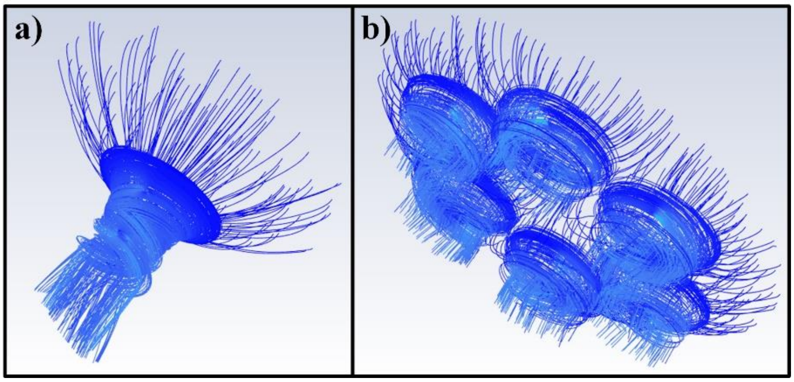

Fig. 6. Fluid flow velocity streamlines for: a) one dual, b) six single rotors configurations

Next, it was also possible to determine additional data, which was difficult to determine experimentally. These were the fluid flow velocity streamlines and the velocity, pressure (Figure 7) and the turbulence intensity field distributions. The streamlines for selected systems, colored depending on the velocity of the particles, are presented in Figure 6.

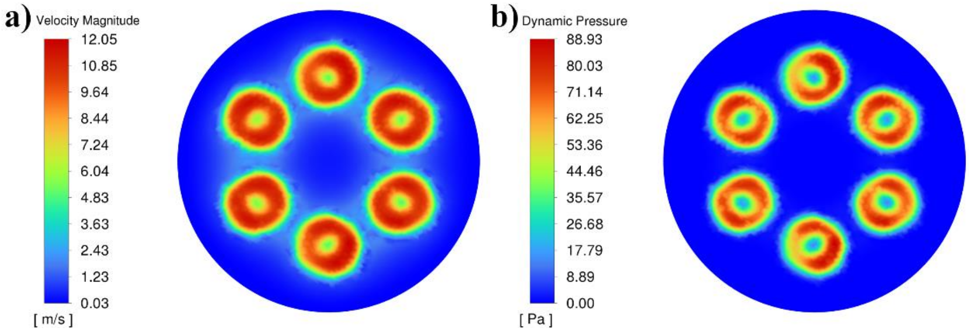

Fig. 7. The six rotors' configurations – outlet side: a) velocity magnitude, b) dynamic pressure

As can be seen in Figure 7 for the six-rotor configuration, the air velocities on the outlet side at the boundary of the computational domain reached a value of approximately 12 m/s, while the dynamic pressure was approximately 89 Pa. With these data, the following approach was determined to compare the analyzed systems. For each of them, in the transverse sections (parallel to the rotor plane) two planes were located 0.05 m and 0.1 m below the rotor plane, respectively. In the case of a two-rotor configuration, these distances are referenced to the bottom one. Then, in post-processing, using the polar coordinate system, control points were located on circles with radii increasing every 0.001 m. The coordinates of the points were selected so that the angular resolution for each radius was constant and amounted to 0.0013 radians (i.e. maintaining a constant number of 500 points on circle). At all points, total flow velocities and turbulence intensities were read and exported to the *Matlab* software, where their maximum values for each radius were determined and presented in Figures 8-9.

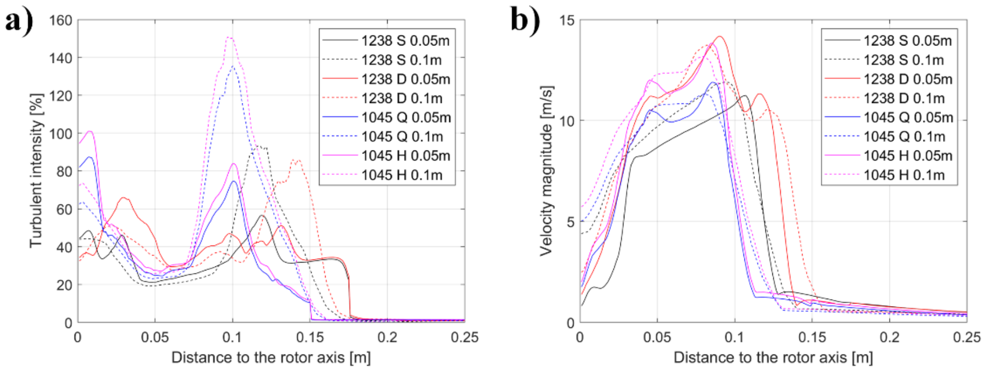

Fig. 8. Comparison of single rotors configurations: a) turbulent intensity, b) velocity magnitude

This approach made it easy to compare and evaluate each configuration. Figure 8 presents a comparison of the analyzed systems with one and two rotors in terms of turbulence intensity and flow velocity. Based on these data, it is possible to adopt a criterion that will enable the indication of the correct distance from the rotor, assuming a constant (less than) value of the flow velocity or the intensity of turbulence. The following nomenclature is used here: *1045 Q*, *1045 H* - smaller rotor for the operating conditions of a: four and six rotor robots, respectively, *1238 S*, *1238 D* – larger rotor in a single and double arrangement, respectively. Based on these figures, it should be noted that for a cross section at a larger distance from the rotor plane, the flow velocity is slightly decreasing. In particular, for the configuration of two rotors, increased values are observed at a greater distance from the rotor.

From these results, it might be concluded that the configuration with a larger rotor is characterized by a smaller intensity of turbulence. However, the distances given in the case of this configuration are too close to the rotor, and thus there is no visible comprehensive development of the disturbed field in these figures. In addition, in the case of a system of two rotors, the defined distances are under the bottom rotor. Therefore, for a larger rotor, a cross section of 0.1 m should be compared with a cross section of 0.05 m.

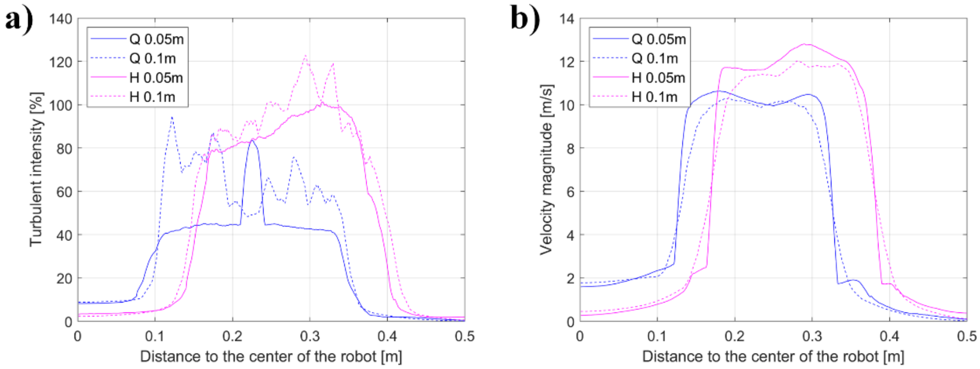

Fig. 9. Comparison of multi rotors configurations: a) turbulent intensity, b) velocity magnitude

It should be noted (Figure 8a) that the intensity of the turbulence quickly drops to a small value of about 2–3% for a smaller rotor for a distance of 0.15 m, while for the larger one it is around 0.175 m. This is because these distances correspond to the length of the propeller blade. For velocities (Figure 8b), they reach maximum values at a distance of about 0.09 m from the center of the propeller. In Figure 9 the same data for configurations with four rotors (marked *Q*), and six rotors (marked *H*) were presented. In this case, these values were determined in relation to the center of the robot.

Based on these, it can be concluded that in the case of a six-rotor configuration, both the turbulence intensity and the flow velocity are higher compared to the four-rotor configuration. However, in the case of a four-rotor configuration, these parameters closer to the geometric center of the robot are higher. This is because the distances between the rotors in the case of a quadrocopter robot are smaller. Therefore, if sensors were placed underneath the robot, a configuration with more rotors would be more appropriate. Taking into account the intensity of the turbulence, the observed small values are 0.4 m and 0.45 m, respectively, for the four- and six-rotor configurations. Figure 10 shows the six-rotor robot final design.

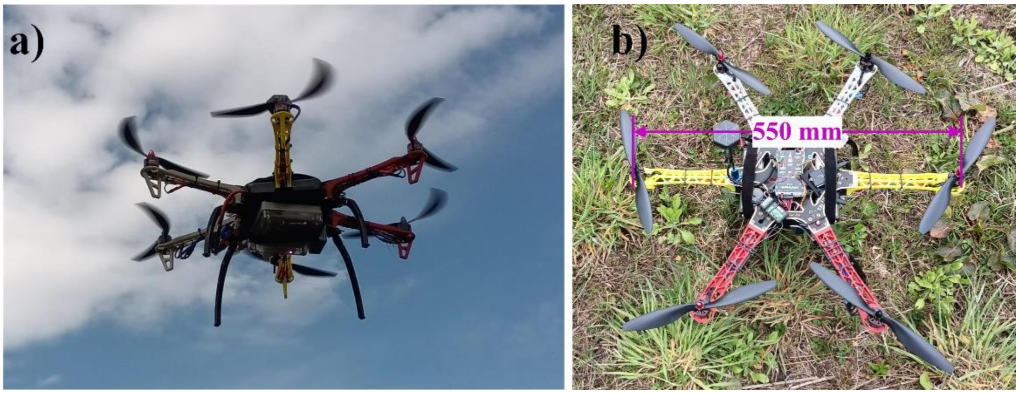

Fig. 10. Final design of six rotor robot: a) during the flight, b) on the ground

5. CONCLUSIONS

In conclusion, an analysis was carried out for selected rotor configurations of multirotor flying robots of the greatest practical importance. On the basis of the workflow presented, an analysis can be performed for any rotor configuration. The results obtained from computer models allow both to improve the design of the robot's measurement system and to improve control, which will also allow for more accurate and faster localization of pollution sources.

The analyzed configurations, among others, were characterized based on the turbulence intensity and flow velocity data. In this way, it was possible to compare and choose the most appropriate configuration. The configuration chosen for future work was a six-rotor robot. Other, additional practical considerations also decided on that choice. That is, for tests with the sensors mounted on the extended arm, the most suitable configuration is the one with more than four rotors. It not only provides redundancy, but allows one to carry larger masses. The configuration with eight rotors introduces a much larger flow-field disorder. Additional factors should be taken into account, such as the smaller thrust force of the dual rotor configuration compared to two independent rotors.

When comparing the values of the maximum parameters given in the cases of four and six rotors, the larger of them were characterized by about 29.5% higher turbulence intensity and 20.4% higher flow velocity. However, for the four-rotor configuration, the magnitudes of these flow parameters closer to the geometric of the robot are greater. When comparing data at a distance of 0.06 m from the center, the flow velocity is about 3.16 times higher and the intensity of turbulence about 2.42 times higher. This is due to the fact that the distances between the rotors of this configuration are smaller. Therefore, when locating the measuring system under the robot, the configuration with more rotors is more suitable.

The dedicated and prepared dynamometer stand allowed not only to verify the CFD computer models but also to determine the characteristics of thrust force, torque, and mechanical power. It enabled a quick and automated way to collect the necessary data. By comparing the thrust force data, itself, the largest difference between the model and the experiment value was about 8%. This value has occurred for the larger of the propellers analyzed, in the case of a smaller rotor it was only about 2%. The biggest difference occurred for the determined mechanical power. The differences in the case of a smaller rotor were at about 10% levels, the higher at about 19%. When comparing the configuration of six smaller rotors with a single system of the same type, the differences amounted to about 5%. The biggest differences occurred for the dual rotor system; however, it is difficult to make a comparison here at the current stage because this configuration was not measured on the dynamometer station. However, in each case, these results can be considered accurate enough, and the modeling process is considered correct.

In future work, more complex simulations should be performed, including both the robot body and the particulate matter in the flow field. Furthermore, the configuration of eight rotors could be taken into account, where single rotors are arranged on eight individual robot arms, and not in a dual configuration on four arms. However, this type of robot is characterized by significant large external dimensions, which is why it is less practical. Moreover, in subsequent studies, it is planned to perform additional calculations for the SRF or frozen-rotor approaches without interfaces and SM calculations, so that the obtained results can be compared. The extended model should also have a larger computing domain and take into account the body of the robot and the particulate matter.

Author Contributions

Conceptualization, methodology, validation, and formal analysis, G.S. and R.F.; investigation, software, resources, data curation, visualization, and writing - original draft preparation, G.S.; writing – review and editing, R.F. All authors have read and agreed to the published version of the manuscript.

Funding

This research was supported by National Subvention No. 16.16.130.942.

Acknowledgments

This research was supported in part by PLGrid Infrastructure.

Conflicts of Interest

The authors declare no conflict of interests.

REFERENCES

Alvarado, M., Gonzalez, F., Erskine, P., Cliff, D., & Heuff, D. (2017). A Methodology to Monitor Airborne PM10 Dust Particles Using a Small Unmanned Aerial Vehicle. *Sensors*, *17*(2), 343. https://doi.org/10.3390/s17020343

Ansys Fluent Theory Guide. Release 2020 R1, ANSYS Inc.

Batchelor, G. K. (1967). *An Introduction to Fluid Dynamics*. Cambridge Univ. Press.

Burgués, J., Hernández, V., Lilienthal, A., & Marco, S. (2019). Smelling Nano Aerial Vehicle for Gas Source Localization and Mapping. *Sensors*, *19*(3), 478. https://doi.org/10.3390/s19030478

Chang, J. H., Chen, Y. Y., & Huang, Y. M. (2018). Design and implementation of an ambient data collection mechanism based on a quadcopter. *Proceedings – 2018 1st International Cognitive Cities Conference, IC3 2018* (pp. 32–36). IEEE. https://doi.org/10.1109/IC3.2018.00017

Chen, J., Scircle, A., Black, O., Cizdziel, J., Watson, N., Wevill, D., & Zhou, Y. (2018). On the use of multicopters for sampling and analysis of volatile organic compounds in the air by adsorption/thermal desorption GC-MS. *Air Qual Atmos Health*, *11*, 835–842. https://doi.org/10.1007/s11869-018-0588-y

Cheng, W. H., Hsieh, T. S., Chu, C. M., Chiang, C. C., & Yuan, C. S. (2019). Application of a Telescoping Microextraction Needle Trap Sampling Device on a Drone to Extract Airborne Organic Vapors. *Aerosol Air Qual. Res.*, *19*, 1593–1601. https://doi.org/10.4209/aaqr.2019.04.0183

Chiang, Y. L., Wang, J. C., Sun, C. H., Wen, T. H., Juang, J. Y., & Jiang, J. A. (2020). Mobile Measurement of Particulate Matter Concentrations on Urban Streets: System Development and Field Verification. *IEEE Access, 8,* 197617–197629. http://doi.org/10.1109/ACCESS.2020.3034489

Chunithipaisan, S., Panyametheekul, S., Pumrin, S., Tanaksaranond, G., & Ngamsritrakul, T. (2018). Particulate Matter Monitoring Using Inexpensive Sensors and Internet GIS: A Case Study in Nan, Thailand. *Engineering Journal*, *22*, 25–37. http://doi.org/10.4186/ej.2018.22.2.25

Ciesielka, W., & Suchanek, G. (2019). Modelling and simulation tests of a quadrocopter flying robot. *New Trends in Production Engineering*, *2*(1), 486–495. http://doi.org/10.2478/ntpe-2019-0052

Dieu Hien, V. T., Lin, C., Thanh, V. C., Kim Oanh, N. T., Thanh, B. X., Weng, C. E., Yuan, C. S., & Rene, E. R. (2019). An overview of the development of vertical sampling technologies for ambient volatile organic compounds (VOCs). *Journal of Environmental Management, 247,* 401–412. http://doi.org/10.1016/j.jenvman.2019.06.090

Faraz, A., Pushpendra, K., Yasar, K., & Pravin, P. P. (2020). Flow and Structural Analysis of a Quadcopter UAV. *International Journal of Advanced Research in Engineering and Technology (IJARET)*, *11*(8), 880–888. http://doi.org/10.34218/IJARET.11.8.2020.086

Glauert, H. (1935). *Airplane Propellers. In: Aerodynamic Theory*. Springer Heidelberg. https://doi.org/10.1007/978-3-642-91487-4_3

Gu, Q. R., Michanowicz, D., & Jia, C. (2018). Developing a Modular Unmanned Aerial Vehicle (UAV) Platform for Air Pollution Profiling. *Sensors*, *18*(12), 4363. https://doi.org/10.3390/s18124363

Hutchinson, M., Liu, C., Chen, W. H. (2019). Source term estimation of a hazardous airborne release using an unmanned aerial vehicle. *J Field Robotics, 36,* 797–817. https://doi.org/10.1002/rob.21844

Landolsi, T., Sagahyroon, A., Mirza, M., Aref, O., Maki, F., & Maki, S. (2018). Pollution monitoring system using position-aware drones with 802.11 Ad-Hoc networks. *2018 IEEE Conference on Wireless Sensors, ICWiSe 2018* (pp. 40–43). IEEE. https://doi.org/10.1109/ICWISE.2018.8633285

Luo, B., Meng, Q., Wang, J., & Ma, S. (2016). A numerical model to simulate the aerodynamic olfactory effect of the gas-sensitive UAV. 2*016 12th World Congress on Intelligent Control and Automation (WCICA)* (pp. 3295–3300). IEEE. http://doi.org/10.1109/WCICA.2016.7578639

Mayuga, G. P., Favila, C., Oppus, C., Macatulad, E., & Lim, L. H. (2018). Airborne Particulate Matter Monitoring Using UAVs for Smart Cities and Urban Areas. *TENCON 2018 - 2018 IEEE Region 10 Conference* (pp. 1398–1402). IEEE. http://doi.org/10.1109/TENCON.2018.8650293

Menter, F. R. (1994). Two-Equation, Eddy-Viscosity, Turbulence Models for Engineering Applications. *AIAA Journal*, *32*, 1598–1605. https://doi.org/10.2514/3.12149

Nagy, A., & Jahn, I. (2019). Advanced Data Acquisition System for Wind Energy Applications. *Periodica Polytechnica Transportation Engineering*, *47*(2), 124–130. https://doi.org/10.3311/PPtr.11515

Ni, J., Yao, L., Zhang, J., Cao, W., Zhu, Y., & Tai, X. (2017). Development of an Unmanned Aerial Vehicle-Borne Crop-Growth Monitoring System. *Sensors*, *17*(3), 502. http://dx.doi.org/10.3390/s17030502

Parra, P. H. G., Angulo, M. V. D., & Gaona, G. E. E. (2018). CFD Analysis of two and four blades for multirotor Unmanned Aerial Vehicle. *2018 IEEE 2nd Colombian Conference on Robotics and Automation (CCRA)* (pp. 1–6). IEEE. http://doi.org/10.1109/CCRA.2018.8588130

Rodriguez, S. (2019). *Applied Computational Fluid Dynamics and Turbulence Modeling: Practical Tools, Tips and Techniques*. Springer Cham. https://doi.org/10.1007/978-3-030-28691-0

Romik, D., & Czajka, I. (2022). Numerical Investigation of the Sensitivity of the Acoustic Power Level to Changes in Selected Design Parameters of an Axial Fan. *Energies*, *15*(4), 1357. https://doi.org/10.3390/en15041357

Smith, B., John, G., Stark, B., Christensen, L. E., & Chen, Y. (2016). Applicability of unmanned aerial systems for leak detection. *2016 International Conference on Unmanned Aircraft Systems (ICUAS)* (pp. 1220–1227). IEEE. http://doi.org/10.1109/ICUAS.2016.7502635

Suchanek, G., Wołoszyn, J., & Gołaś, A. (2022). Evaluation of Selected Algorithms for Air Pollution Source Localisation Using Drones. *Sustainability*, *14*(5), 3049. https://doi.org/10.3390/su14053049

Tulwin, T. (2019). Low Reynolds Number Rotor Blade Aerodynamic Analysis. *MATEC Web of Conferences*, *252*, 04006. https://doi.org/10.1051/matecconf/201925204006

Villa, T., Salimi, F., Morton, K., Morawska, L., & Gonzalez, F. (2016). Development and Validation of a UAV Based System for Air Pollution Measurements. *Sensors*, *16*(12), 2202. https://doi.org/10.3390/s16122202

Wang, D., Wang, Z., Peng, Z. R., & Wang, D. (2020). Using unmanned aerial vehicle to investigate the vertical distribution of fine particulate matter. *International Journal of Environmental Science and Technology*, *17*, 219–230. https://doi.org/10.1007/s13762-019-02449-6

Wang, Q. (2019). Real-time Atmospheric Monitoring of Urban Air Pollution Using Unmanned Aerial Vehicles. *WIT Transactions on Ecology and the Environment*, *236*, 79–88. http://doi.org/10.2495/AIR190081

Wilcox, D. C. (2006). *Turbulence Modeling for CFD (Third Edition)*. D C W Industries.

Applied Computer Science, vol. 18, no. 3, pp. 105–129
doi: 10.35784/acs-2022-24

Submitted: 2022-05-19 | Revised: 2022-09-20 | Accepted: 2022-09-23

Keywords: vector network analyzer, microwave device, S-Band network, reflection coefficient, waveguide

Benjamin KOMMEY [0000-0003-3145-0066]*, *Ernest Ofosu ADDO**, *Elvis TAMAKLOE**, *Eric Tutu TCHAO* [0000-0002-3242-9747]*, *Henry NUNOO-MENSAH**, *Bright YEBOAH AKOWUAH**

A SIX-PORT MEASUREMENT DEVICE FOR HIGH POWER MICROWAVE VECTOR NETWORK ANALYSIS

Abstract

The changes experienced in technology due to the third industrial revolution have over the years contributed immensely to the development of efficient devices and systems. As a result, solutions have been provided to challenges encountered in the heating industry. However, higher efficiency and better performance has undoubtedly been highly sort after. This paper presents the complete industrial development of a new system of a microwave device for use in S-band networks (2.45 GHz ISM band in this application): a vector network analyzer (VNA). The VNA, which is designed based on the six-port measurement principle, provides accurate measurements of both magnitude and phase of the load reflection coefficient. The device is designed to have high power handling capabilities and works under the full operating conditions of high-power microwave generators. Initial measurements show that the device perform stable and can perform temperature-independent measurements over protracted periods. The system is suited for on-line monitoring and control of network parameters in industrial waveguide applications.

1. INTRODUCTION

Heating is arguably the commonest process in the manufacturing industry, where it is used to effect physical and chemical changes in raw materials to produce food, textile, and fuel, among others. However, industrial heating remains largely a sluggish, imprecise, and difficult process to control especially when done through conventional way of material surface heating. Microwave volumetric heating offers an exceptionally efficient solution to these problems. In this process, injected energy is transferred electromagnetically through the surfaces of workpieces, rather than as heat flux like in conventional methods. Infinitesimal elements in the workload volume are thus heated individually and at an approximately equal rate. Heating times and effective energy variation within workload are reduced significantly while maintaining competitive running costs. A basic industrial

* Kwame Nkrumah University of Science and Technology, Faculty of Electrical and Computer Engineering, Department of Computer Engineering, Kumasi, Ghana, bkommey.coe@knust.edu.gh

microwave heating system comprises a high-power magnetron-head that generates and supplies microwave energy at 900 MHz or 2.45 GHz to a cavity oven through a waveguide network. A typical transmission line features components such as an isolator for magnetron protection, an analyzer for network monitoring, and a tuner for maintaining maximum magnetron-load power coupling. Current high power microwave heating processes rely on the use of the loop coupler for measuring the reflection in waveguide networks. This device determines the reflection coefficient by measuring the forward and reverse power flowing in the guide section. However, the coupler only produces the magnitude of the reflection coefficient but not the phase. This measurement information is often inadequate to properly match the network.

In this paper, we present a simplified formulation for extracting the vector reflection from sampled wave-amplitude measurements in a microwave network. The discussed method is based on the six-port measurement technique first introduced in (Engen,1977), but without the need for extensive calibration. Using this formulation, we describe the design and implementation of a compact VNA capable of measuring the magnitude and phase of the reflection coefficient in high microwave power waveguide applications. It is useful in systems which require online and inline network parameter monitoring, where employing commercial VNAs may not be feasible. Empirical results show good performance when compared to a commercial VNA. The proposed VNA is designed for use in applications where the network is sourced by a 6-kW magnetron. Using simulations, the power handling capability of the VNA and its suitability for the intended application has been demonstrated. The presented VNA was designed as part of a larger system where reflection measurements are fed to another device which is used to achieve automatic tuning of the network in a feedback loop. Description of the tuning device is outside the scope of this paper and will not be discussed. However, references will be made to this device and its interface with the VNA.

This paper is organized as follows: Section 2 review some literature and section 3 discusses fundamentals of network analysis and the design of the network analyzer. Section 4 describes the implementation, calibration and evaluation of the developed system and section 5 concludes the paper.

2. LITERATURE REVIEW

There are many processes that take place in the manufacturing industries today. However, only few processes are indisputably integral to the continuous operation and success of these industries. Industrial heating by far has come a long way since its inception. It is employed in the industries to effect physical and chemical changes in raw materials for the fabrication of food (Sorică et al., 2021), medicines (Gartshore, Kidd & Joshi, 2021; Shah, 2019), textiles (Elshemy & Haggag, 2019; De-chao, 2015), fuels (MacDonald & Miadonye, 2018; Amornraksa & Sritangthung, 2020) and many more. Over the years, industrial heating has experienced advancements to improve upon the shortfalls of the conventional heating techniques. Microwave volumetric heating has provided an efficient solution to conventional heating methods as it heats both the core and surface of each element of the product simultaneously and approximately at equal rate. Information and data collected from this field has prompted a few studies aimed at developing microwave heating techniques with a handful of prototypes developed. Traditional or conventional heating used in the early days of industrialization was achieved primarily through fuel-based heating techniques. In this method, the generated heat is transferred as heat flux to the surface of the product either by heat conduction, convection, radiation, or all three-transfer media. Physical and chemical changes take place from the surface to the core of the product and are dependent on certain properties like specific heat capacity and many more. Even though conventional heating system and equipment are easy to build, this heating techniques are not energy saving, time consuming, difficult to control heating flow rates, presents quality problems of products and raises CO_2 emission concerns.

As opposed to traditional heating method, electricity-based heating techniques have dynamically changed the heating mechanism to date. Although there are various electro-technologies employed for heating for instance induction and laser heating (Vishnuram et al., 2021; Caiazzo & Alfieri, 2018; Murzin, Kazanskiy & Stiglbrunner, 2021), the use of microwave energy has been indispensable. The use of microwave technology provides significant benefits such as energy efficiency, time saving, effective control of heat flow rate, improves CO_2 emissions and assures the quality level of products.

Microwave heating systems that exist have different designs. These differences primarily stem from the nature of the network analyzer and the tuner. In reference to the network analyzer which measures complex reflection coefficient characterizing the load, different design models exist based on the measurement principles employed. Wave separation method and Interference method are the categories under which network analyzers are made. Conventional network analyzers were designed based on wave separation methods. In this method, an incident wave injected into one network port is observed as responses at all ports and compared to stimulus. Reflection coefficient measurements are achieved provided the stimulus and back-propagating signal waves are separated since they appear at the same port. This separation is carried out using directional couplers or bridges which increases design cost. In contrast to wave separation method, interference method does not involve separation of port stimulus from responses. This method primarily depends on the combination of two waves to produce standing wave patterns along the transmission line. The creation and observation of the wave combinations can be achieved either simultaneously at different ports or sequentially at a given port. Six-port reflectometer typical operates on interference method. It is employed as the standard for complex measurement of the reflection coefficient of a device under test (DUT) using four power readings and can be easily calibrated for diverse applications (Moubarek & Gharsallah, 2016; Moubarek, Almanee & Gharsallah, 2019).

(Mohra, 2004) presented the design of a six-port reflectometer structure using two microstrip three-section couplers. In this design, the six-port reflectometer was developed on a Teflon substrate at a center frequency of 3.5GHz using dimensions of a three-section coupler. The **S** parameters which were simulated and measured were found around -20 dB with 2.0 dB maximum deviation. Reflections at the input port were also found to be less than -25dB. Although this design reduces the size of the reflectometer, the reflection coefficient was better as it is difficult to achieve perfection.

3. MATERIALS AND METHODS

3.1. Scattering parameters

In low frequency circuits, dimensions of circuit elements are small relative to the wavelength. Thus, these circuits can be analyzed as interconnections of active and lumped passive elements with unique currents and voltages at any point in the circuit. In such cases, phase delay between circuit nodes is negligible. Furthermore, since fields in low frequency circuit are supported by two or more conductors, the fields are considered transverse electromagnetic (***TEM***). This leads to quasi-static solutions to Maxwell's equations and the popular circuit theory concepts like Kirchhoff's laws etc. Although these basic concepts can be used to understand microwave analysis, they are not directly applicable to microwave circuits in general. This is especially true for non-***TEM*** lines such as waveguides, which support an additional set of fields: transverse electric (***TE***) and transverse magnetic (***TM***), whose voltages and currents cannot be uniquely defined.

In microwave circuits, signals are described by wave variables which are linked to waves physically traveling along transmission lines. As illustrated in Figure 1, variable describing waves impinging on a device's ports are denoted ***a*** whiles that of reflected and/or transmitted waves flowing outward are denoted ***b***. The magnitude of a wave variable is related to the mean power carried by its corresponding wave. The phase, however, is equal to the physical wave phase at a given reference plane.

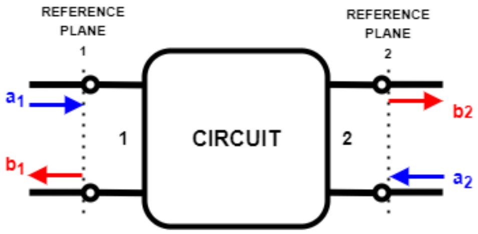

Fig. 1. A two port microwave circuit showing waves on its ports

Scattering (S) parameters provide an intuitive and complete description of a network at its ports. They unify the paradigm for direct measurement in ***TEM*** fields and the idea of incident, transmitted, and reflected waves. Consider an arbitrary ***n***-port microwave network with reference planes at each of its ports where the wave variables are defined. There are ***n*** impinging waves, $\boldsymbol{a_i}$ and ***n*** responses $\boldsymbol{b}_j$, where $i,j=1,\ldots n$. See Figure 2.

Here, the $\boldsymbol{n}^2$ transfer functions describing the response of port to stimuli are quantified by the ***S*** parameters $\boldsymbol{S_{ji}}$ given by Equation 1. The ***S*** parameters are classified into reflection coefficients $\Gamma_i = S_{ji}$ and transmission coefficients $S_{ii}, j \neq i$.

$$S_{ji} = \frac{b_j}{a_i},\ i,j = 1,\ldots n \tag{1}$$

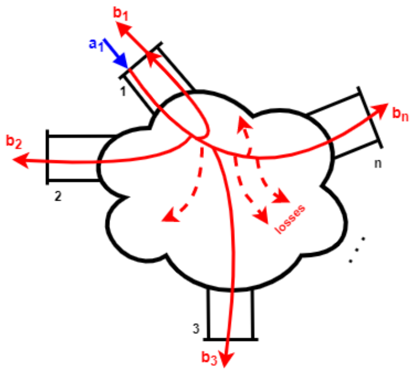

Fig. 2. Scattering of an impinging wave a_1 in an arbitrary n-port microwave network

3.2. Network Analyzer Technologies

The network analyzer is an instrument for measuring (complex) *S* parameters characterizing passive and active networks. There is different possible hardware configuration for the implementation of such an instrument. However, network analyzers can be categorized broadly based on the measurement principles employed: wave separation or interference.

3.3. Wave Separation Method

The wave separation method is conceptually straightforward, and the measurements are based directly on the ***S*** parameter definition (Equation 1). This method forms the working principle of almost all 'conventional' network analyzers available commercially. Here, an incident wave is injected into one network port and the responses at all ports are observed and compared to stimulus. To arrive at an ***S*** parameter, the phase difference, and amplitudes ratio of both the stimulus and the corresponding response must be determined. For reflection coefficient measurements, since the stimulus and back-propagating signal appear at the same port, the two waves must be separated. The functional overview of a conventional network analyzer is illustrated in Figure 3 with a 2-port device under test (DUT) connected and being measured.

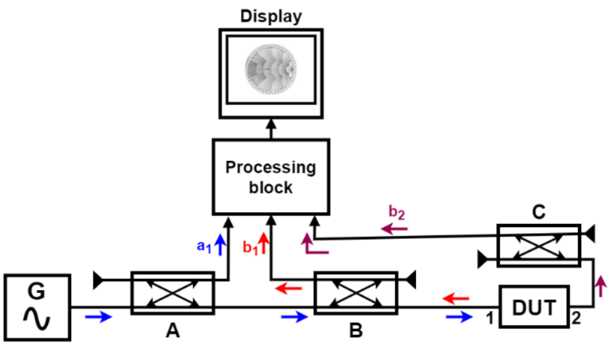

Fig. 3. Principal block diagram of a conventional network analyzer based on the wave separation method

The set-up uses three identical directional couplers or bridges, **A** for transmission and separation of stimuli and responses. The input signal supplied from the generator is delivered to the DUT through couplers **A** and **B** while a fraction of the stimulus is diverted to a processing unit. The reflected signal from the DUT and its output response are coupled to the processing unit through **B** and **C** respectively. In the processing unit, the wave amplitudes are extracted, and their respective ratios computed. The amplitude measurements are easily obtained using power detectors. On the other hand, estimation of the phase differences is achieved separately and can be quite complicated. To do this, most network analyzers employ heterodyne double-conversion receivers which are phase-locked to the incident wave.

3.4. Interference Method

Unlike the wave-separation method, the interference technique does not involve separating the port stimulus from the response. The method relies on the combination of the two waves to produce standing wave patterns along the transmission line. Several controlled linear combinations of the incident and reflected waves are setup in a measurement system and the resulting magnitudes are extracted. The creation and observation of the wave combinations can either be done simultaneously at various ports of the measurement system or achieved sequentially at a given port using multi-state hardware as is done in the slotted-line system (Miniature Linear Motion Series L12, 2019). With the observed scalar data, both magnitude and phase of the ***S*** parameters can be obtained.

3.5. The Six Port Reflectometer

The six-port reflectometer is a network analyzer based on the interference technique which measures the reflection coefficient of a connected device. The building block of the reflectometer is a linear six-port network. As illustrated in Figure 4, one port is connected to a signal source, another is terminated in a DUT, and the remaining four ports are connected to power detectors (D1–D4).

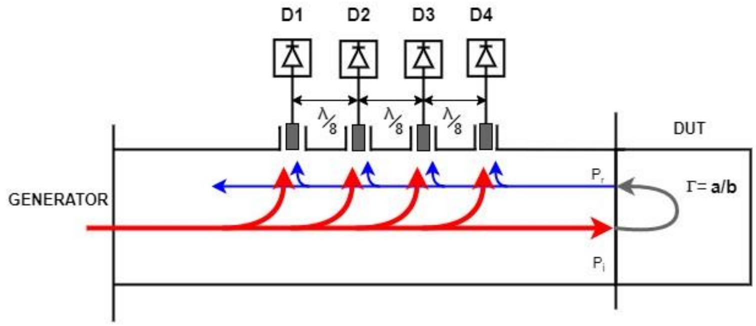

Fig. 4. Basic block diagram of the six-port reflectometer

The six-port device is described by a 6 × 6 scattering matrices relating its input and output power wave vectors, $\boldsymbol{a}$ and $\boldsymbol{b}$. Considering that the four ports 3–6 are connected to matched loads $\boldsymbol{a}_{3\text{-}6} = 0$, while Port 2 is connected to an unknown load characterized by a reflection coefficient Γ_L to be retrieved i.e $a_2 = \Gamma_L b_2$. With the reciprocity of the device and symmetry across the guide cross section $(123 \leftrightarrow 456)$

$$[\boldsymbol{b}] = [\boldsymbol{S}]\begin{bmatrix} a_1 \\ \Gamma_L b_2 \\ 0 \\ 0 \\ 0 \\ 0 \end{bmatrix} = \begin{bmatrix} S_{11} & S_{21} \\ S_{21} & S_{11} \\ S_{31} & S_{61} \\ S_{41} & S_{51} \\ S_{51} & S_{41} \\ S_{61} & S_{31} \end{bmatrix}\begin{bmatrix} a_1 \\ \Gamma_L b_2 \end{bmatrix} = \begin{bmatrix} S_{11} + \Gamma_L' S_{21} \\ \Gamma_L'/\Gamma_L \\ S_{31} + \Gamma_L' S_{61} \\ S_{41} + \Gamma_L' S_{51} \\ S_{51} + \Gamma_L' S_{41} \\ S_{61} + \Gamma_L' S_{31} \end{bmatrix} a_1 \tag{2}$$

with

$$\Gamma_L' = \frac{S_{21}\Gamma_L}{1 - S_{11}\Gamma_L} \tag{3}$$

The power measured at the 4 power ports are

$$\begin{bmatrix} |b_3|^2 \\ |b_4|^2 \\ |b_5|^2 \\ |b_6|^2 \end{bmatrix} = \begin{bmatrix} |s_{31} + \Gamma_L' s_{61}|^2 \\ |s_{41} + \Gamma_L' s_{51}|^2 \\ |s_{51} + \Gamma_L' s_{41}|^2 \\ |s_{61} + \Gamma_L' s_{31}|^2 \end{bmatrix} |a_1|^2 =$$

$$= \begin{bmatrix} |s_{31}|^2 + |s_{61}|^2|\Gamma_L'|^2 + 2|s_{31}||s_{61}||\Gamma_L'|\cos(\angle\Gamma_L' + \angle s_{61} - \angle s_{31}) \\ |s_{41}|^2 + |s_{51}|^2|\Gamma_L'|^2 + 2|s_{41}||s_{51}||\Gamma_L'|\cos(\angle\Gamma_L' + \angle s_{51} - \angle s_{41}) \\ |s_{51}|^2 + |s_{41}|^2|\Gamma_L'|^2 + 2|s_{51}||s_{41}||\Gamma_L'|\cos(\angle\Gamma_L' + \angle s_{41} - \angle s_{51}) \\ |s_{61}|^2 + |s_{31}|^2|\Gamma_L'|^2 + 2|s_{61}||s_{31}||\Gamma_L'|\cos(\angle\Gamma_L' + \angle s_{31} - \angle s_{61}) \end{bmatrix} |a_1|^2 \tag{4}$$

The phases of the four probes depend on their positions. If the four probes are spaced by $d = \lambda_g/8$ and are assumed to have the same coupling level $|s_{31}| = |s_{41}| = |s_{51}| = |s_{61}| = C$ then,

$$\begin{bmatrix} s_{31} \\ s_{41} \\ s_{51} \\ s_{61} \end{bmatrix} = \begin{bmatrix} Ce^{j\frac{3kd}{2}} \\ Ce^{j\frac{kd}{2}} \\ Ce^{-j\frac{kd}{2}} \\ Ce^{-j\frac{3kd}{2}} \end{bmatrix} = \begin{bmatrix} Ce^{j\frac{3\pi}{8}} \\ Ce^{j\frac{\pi}{8}} \\ Ce^{-j\frac{\pi}{8}} \\ Ce^{-j\frac{3\pi}{8}} \end{bmatrix} \tag{5}$$

and

$$\begin{bmatrix} |b_3|^2 \\ |b_4|^2 \\ |b_5|^2 \\ |b_6|^2 \end{bmatrix} = C^2 \begin{bmatrix} 1 + |\Gamma_L'|^2 + \sqrt{2}|\Gamma_L'|[-\cos(\angle\Gamma_L') + \sin(\angle\Gamma_L')] \\ 1 + |\Gamma_L'|^2 + \sqrt{2}|\Gamma_L'|[\cos(\angle\Gamma_L') + \sin(\angle\Gamma_L')] \\ 1 + |\Gamma_L'|^2 + \sqrt{2}|\Gamma_L'|[\cos(\angle\Gamma_L') - \sin(\angle\Gamma_L')] \\ 1 + |\Gamma_L'|^2 + \sqrt{2}|\Gamma_L'|[-\cos(\angle\Gamma_L') - \sin(\angle\Gamma_L')] \end{bmatrix} |a_1|^2 \tag{6}$$

where λ_g is the guide wavelength.

Combining the matrix row equations

$$-|b_3|^2 + |b_4|^2 = |b_5|^2 - |b_6|^2 = 2\sqrt{2}C^2\left|\Gamma_L'\right| cos\left(\angle\Gamma_L'\right)|a_1|^2 \tag{7}$$

$$|b_3|^2 - |b_6|^2 = |b_4|^2 - |b_5|^2 = 2\sqrt{2}C^2\left|\Gamma_L'\right| sin\left(\angle\Gamma_L'\right)|a_1|^2 \tag{8}$$

$$|b_3|^2 + |b_5|^2 = |b_4|^2 + |b_6|^2 = 2C^2\left(1 + \left|\Gamma_L'\right|^2\right)|a_1|^2 \tag{9}$$

From Equations 7 and

$$\sqrt{(-|b_3|^2 + |b_4|^2 + |b_5|^2 - |b_6|^2)^2 + (|b_3|^2 - |b_6|^2 + |b_4|^2 - |b_5|^2)^2} = \\ = 4\sqrt{2}C^2\left|\Gamma_L'\right||a_1|^2 \tag{10}$$

$$\sqrt{(-|b_3|^2 + |b_5|^2 + |b_4|^2 - |b_6|^2)^2 + (|b_3|^2 - |b_5|^2 + |b_4|^2 - |b_6|^2)^2} = \\ = 4\sqrt{2}C^2\left|\Gamma_L'\right||a_1|^2 \tag{11}$$

From Equations 9, 10, and 11

$$|b_3|^2 + |b_5|^2 + |b_4|^2 - |b_6|^2 = 4C^2\left(1 + \left|\Gamma_L'\right|^2\right)|a_1|^2 \tag{12}$$

$$\sqrt{(|b_3|^2 - |b_5|^2)^2 + (|b_4|^2 - |b_6|^2)^2} = 4C^2\left|\Gamma_L'\right||a_1|^2 \tag{13}$$

then

$$\left|\Gamma_L'\right|^2 - \frac{|b_3|^2+|b_4|^2+|b_5|^2+|b_6|^2}{\sqrt{(|b_3|^2-|b_5|^2)^2+(|b_4|^2-|b_6|^2)^2}}\left|\Gamma_L'\right| + 1 = 0 \tag{14}$$

or

$$X = \frac{|b_3|^2+|b_4|^2+|b_5|^2+|b_6|^2}{\sqrt{(|b_3|^2-|b_5|^2)^2+(|b_4|^2-|b_6|^2)^2}} = \frac{\left|\Gamma_L'\right|^2+1}{2\left|\Gamma_L'\right|} = \frac{e^{-ln\left|\Gamma_L'\right|}+e^{ln\left|\Gamma_L'\right|}}{2} = cos(\,ln\left|\Gamma_L'\right|)\,. \tag{15}$$

Therefore, from Equations 14 and 15, the modulus of $\Gamma_L'$is obtained as follows

$$\left|\Gamma_L'\right| = X + \sqrt{X^2 - 1} = e^{cosh^{-1}(X)} \tag{16}$$

The phase of Γ_L' is then obtained using Equations 2.7 and 2.8

$$\angle\Gamma' = atan2[(|b_3|^2 + |b_4|^2 - |b_5|^2 - |b_6|^2), (-|b_3|^2 + |b_4|^2 + |b_5|^2 - |b_6|^2)] \tag{17}$$

Finally, inverting Equation 2.3, the reflection coefficient characterizing the load is given by

$$\Gamma_L = \frac{\Gamma_{L_L}'}{S_{11}\Gamma_{L_L}'+S_{21}} \tag{18}$$

3.6. Reflectometer Model

The reflectometer block was modeled as a 100 mm WR340 guide section with four SMA probes inserted into its broadface, $\frac{\lambda_g}{8}$ apart and symmetrical across the block's vertical cross-section (Figure 5).

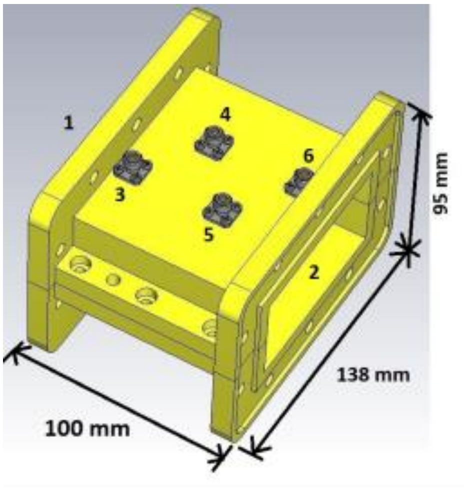

Fig. 5. Reflectometer block

To control the coupling level of the ports, each probe was trimmed such that their tip was 2.7 mm from the inner guide wall. The probes were then shifted 15 mm away from the longitudinal guide axis to further reduce the coupling. This was to ensure that only a small amount of power is coupled and that the probe did not heavily perturb the waves in the guide. From simulation in CST MWS, each probes registered a $\Gamma_L^{'} - 78.7$ dB coupling level across the S-band. The reflectometer block was also realized from aluminum. Measurement of the four ports with the Agilent E5071c VNA showed that each port experienced higher coupling levels with approximately -60 dB at 2.45 GHz (Figure 6).

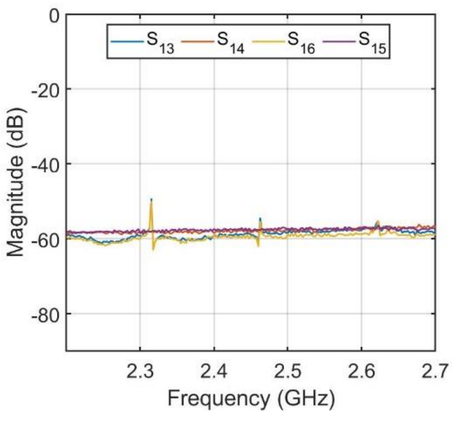

Fig. 6. Measured coupling coefficient magnitudes of the 4 probes

This was due to probe trimming error. This will be corrected in future work towards high power measurements. However, for low power measurements, the high port coupling levels are within safe levels for the device. The most important thing, which was satisfied, was that all four ports had approximately the same measured levels. This is an important premise for the reflectometer's operation (see Equations 5 and 6).

3.7. VNA Front-End

The flow of coupled power waves through the functional blocks of the VNA front-end is summarized in Figure 7.

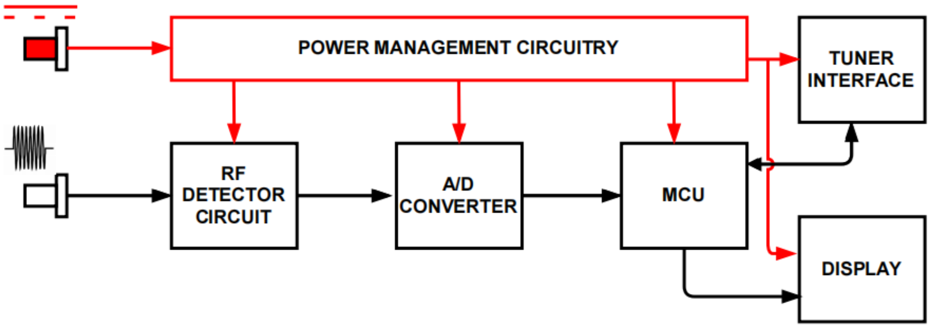

Fig. 7. Function block diagram of the VNA front end

Power coupled from the waveguide is measured by an RF detector circuit. The analog output of the detector circuit is fed to an analog-to-digital converter (ADC) which produces digital codes representing the measured power. The digitized measurements are processed by a microcontroller unit (MCU) to retrieve the data about reflection in the waveguide network. Reflection measurements are also shown on a display. The front end is powered by a DC supply. A power circuitry manages power quality and distributes appropriate portions to all the functional blocks.

3.8. RF Detector Circuit

The detector circuit measures RF power coupled from each reflectometer port. The circuit uses the Analog Devices' AD8318 demodulating logarithmic amplifier as its primary element. AD8318 converts RF input signals to corresponding low noise dB-scaled voltage outputs by employing a successive fast response compression technique over a chain of nine amplifier stages, each of which is equipped with a detector cell (Figure 8 a and b).

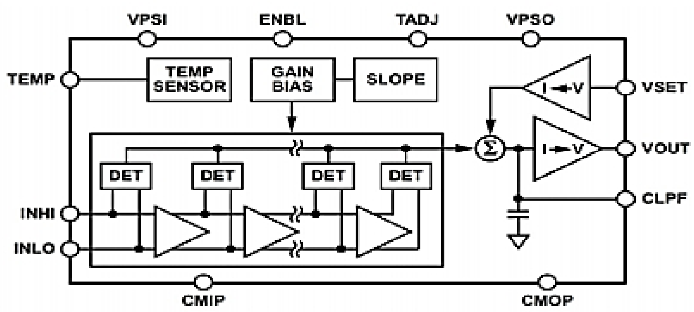

Fig. 8a. Functional Block Schematic

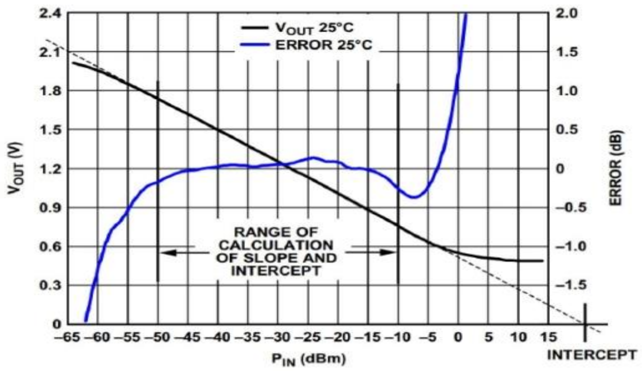

Fig. 8b. Typical response vs. input signal amplitude

The device has an impressive 60 dB usable input dynamic range with a high degree of log conformance over the range (error = ±1 dB). Typical device output voltage temperature stability is ±0.5 dB. Additional device information can be found in (Practical Design Techniques for Sensor Signal Conditioning, 2019). To configure the AD8318 for measurement, a portion α of the output voltage is feedback to the device's setpoint interface by connecting the $\boldsymbol{V_{OUT}}$ pin to the $\boldsymbol{V_{SET}}$ pin directly or through a ground referenced resistive feedback divider. This yields an output which is a decreasing linear-in-dB function of input RF signal power $\boldsymbol{P_{IN}}$. A direct $\boldsymbol{V_{OUT}}$-$\boldsymbol{V_{SET}}$ connection maintains the chip's nominal logarithmic slope (typically -24 mV/dB with $\boldsymbol{P_{INTERCEPT}}$ = 20 dBm intercept on the abscissa) whiles introducing divided feedback allows for shaping the chip's response function and output dynamics. ***Slope*** is scaled by the feedback factor α. The increase in ***Slope*** reduces dynamic range which is, of course, limited to the swing capability of AD8318's PNP output stage: $\boldsymbol{\alpha V_{OFFSET} < V_{OUT} < (V_{PS} - 0.4V)}$ where $\boldsymbol{V_{OFFSET}}$ = 0.5 V and $\boldsymbol{V_{PS}}$ ∈ [4.5 V–5.5 V] are the detector's output offset and appropriately decoupled positive supply respectively (Practical Design Techniques for Sensor Signal Conditioning, 2019). In this work, the direct output setpoint connection was employed as the corresponding $\boldsymbol{V_{OUT}}$ range matches the full-scale range of the analog-to-digital converter (ADC) in the next stage. Furthermore, this choice also eliminated possible output drifts due to temperature variations that may occur in the resistive feedback elements. To trim temperature drift of the AD8318 functionality, a ground referenced RTADJ resistor is used. For optimal temperature compensation in the S-band, RTADJ was set as 499Ω (1 MHz to 8 GHz, 70 dB Logarithmic Detector/Controller, 2019). The CMIP and CMOP I/O common pins were also connected to a low impedance ground plane for optimum electrical and thermal performance.

The single-ended RF input to the detector and input stage common (INLO) were ac-coupled with two 220 pF capacitors. The capacitor pair, together with an internal 10 pF capacitor, formed a high pass corner at ~ 16 MHz which cuts out unwanted lower frequency signals particularly the spurious digital noise from the front-end's clocking system. The impedance of the input interface was estimated as 27 – j75Ω at 2.45 GHz. While the input could have been reactively matched, it was not necessary. A 52.3Ω resistor was used to shunt the feed line. This terminating resistor combined with the relatively high input impedance of the chip provide a wideband 50Ω match. Each reflectometer probe couples -78.7 dB of the 6-kW output power launched by the microwave generator in the target application. This means approximately -11 dBm of power will be fed into the detector circuit. A fixed resistor RF attenuator was introduced at the circuit's input to put its operation in the middle of the AD8318's linear response and low error range. Furthermore, it would protect the AD8318 chip (12 dBm input power rating) in events of microwave power spikes which may result from magnetron malfunction, heavy network reflection, or arcing. The ***T*** structure, referenced to $\boldsymbol{Z_0} = 50\Omega$, produced a wideband 19.28 dB attenuation with an 87 dB return loss. The series and shunt resistances were related to the voltage ratio ***N*** by Equations 19 and 20 respectively.

$$R_5 = R_6 = Z_0\left(\frac{N-1}{N-1}\right) \tag{19}$$

$$R_7 = Z_0\left(\frac{2N}{N^2-1}\right) \tag{20}$$

Effects of the attenuator were compensated for during device calibration. Finally, a grounded 100 nF capacitor was connected the CLPF pin to reduce the output video bandwidth and hence smoothen the detector output while maintaining an adequate slew rate. The RF detector circuit with the resistor attenuator is shown in Figure 9.

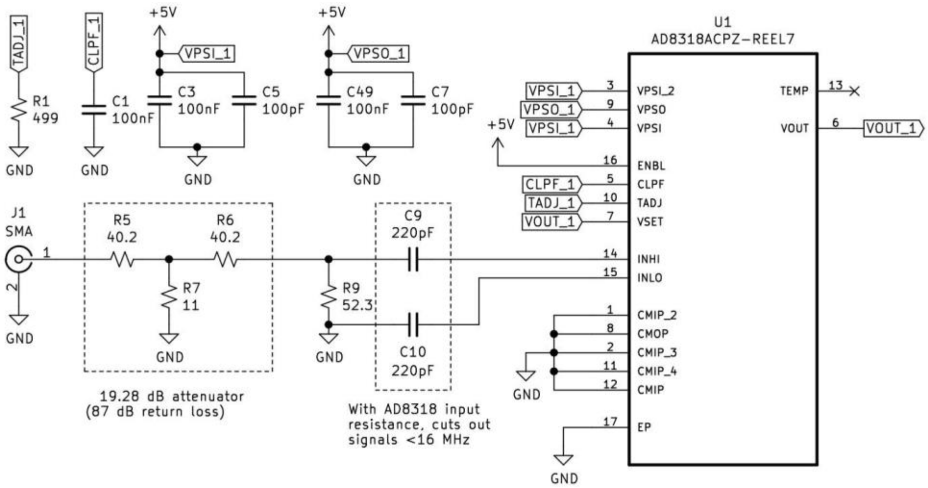

Fig. 9. RF detection circuit with signal attenuator for a reflectometer port

3.9. ADC and Logic Level Translators

The detector outputs of the four ports were interfaced with the Texas Instruments (TI) ADS7841 precision sampling ADC as shown in Figure 10.

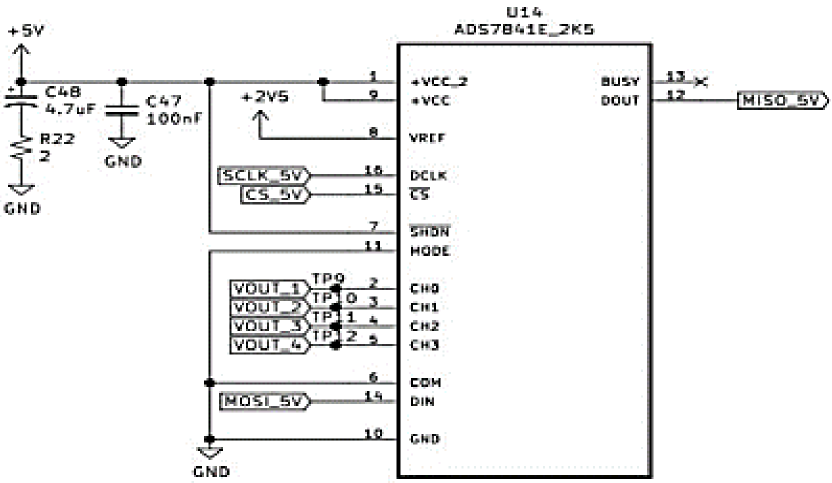

Fig. 10. ADS7841 based circuit for digitizing RF detector output voltages

The ADS7841 is a 4-channel successive-approximation register (SAR) ADC with a 200 kHz max throughput and a programmable resolution: 8 or 12 bits. The ADC was configured in 12-bit mode and its voltage reference V_{REF} was provided externally by an Analog Devices' ADR421 2.5 V ultra-precision reference (± 0.04% tolerance, 3-ppm/°C temperature coefficient) (Ultraprecision, Low Noise, 2.048 V/ 2.500 V/ 3.00 V/ 5.00 V XFET ® Voltage References, 2013). The four analog measurements on the single-ended channels were sequentially captured ADC by the ADC's input multiplexer in the hold mode. The configuration of the analog multiplexer was set by conversion control bytes provided via the DIN (MOSI) pin by the MCU through its 8-bit serial peripheral interface (SPI) bus. The ADS7842 requires an external clock to run the conversion process. A 125 kHz clock signal was supplied by the external processor via the DCLK (SCLK) pin. Data on the MOSI line was latched on the rising edge of DCLK. The communication between the converter and the MCU consists of eight clock cycles. Each complete conversion was accomplished with three serial communications (Figure 11).

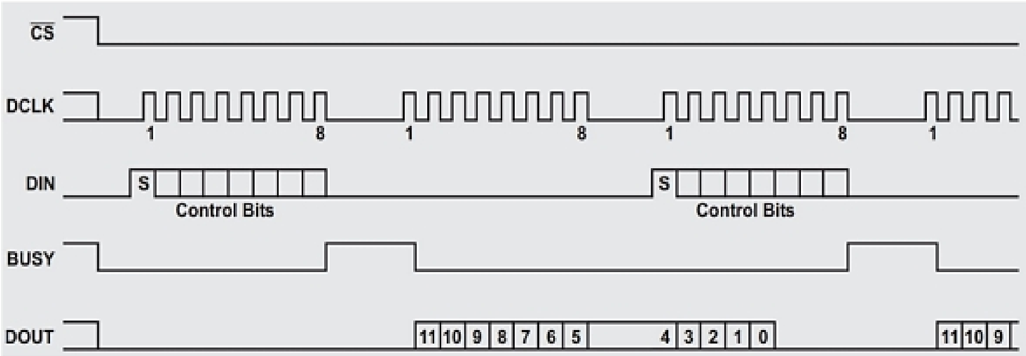

Fig. 11. Timing diagram of the ADS7841's 24-clock cycle per conversion, 8-bit SPI interface

The digital output is shifted out of the DOUT (MISO) pin on the falling edge of DCLK. The three conversion results are manipulated in the MCU to extract the 12-bit measurement word. The ADS7841 was powered by a +5 V rail whiles the interfacing MCU operated on +3.3 V. As such they have different I/O logic-level standards. To resolve the voltage incompatibilities between the two parts and ensure proper operation of the system, logic translators were used on the data bus. The MOSI and SCLK lines were run through the TI SN74LVC2T45 dual-bit bus transceiver whiles the MISO line was connected to the SN74LVC1T45 transceiver. The translators supported bidirectional logic-level shifting and hence required two separate power-supply rails: +3.3 V and +5 V. However, since the individual SPI lines were unidirectional, translation directions were 'locked' to one sense by tying the chips' DIR pins to ground as shown in Figure 12.

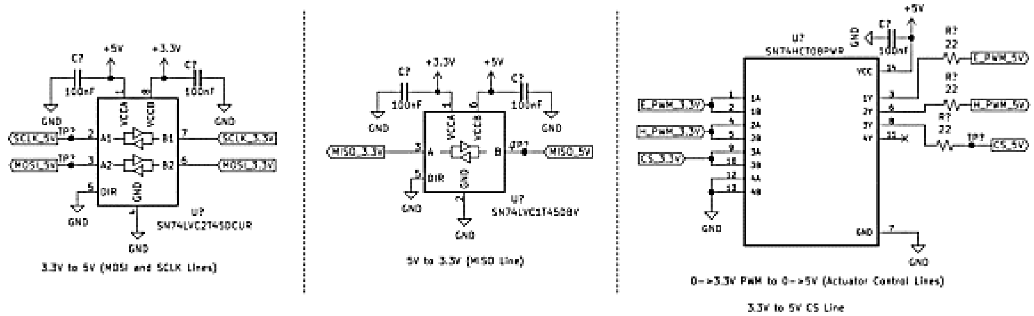

Fig. 12. Logic Level Translators

For the SPI chip select (CS) line, the unidirectional SN74HCT08 AND gate chip was used for level shifting. All transceivers had data rates upwards of 1 Mbps, which was more than enough for the ADS7871-MCU communication. Furthermore, the logic translators acted as buffer registers which acted as a Faraday shield between the converter's digital lines and the data bus thus to minimizing loading on the ADC's digital output (Practical Design Techniques for Sensor Signal Conditioning, 1999). This was very useful even though the ADS7841 has tri-state I/Os.

All power supplies to ADC, reference, and level-shifters were well bypassed with 100 nF capacitors to filter out noise originating from nearby digital logic and switching power supplies. Additional 4.7 μF and 2Ω series resistor was added to the ADC rail to improve the noise suppression. This was particularly important because the ADS7841's basic SAR architecture is very sensitive to glitches on the power supply, reference, and digital inputs latching onto the analog comparator. Furthermore, the ADC has no inherent noise rejection scheme on the V_{REF} input (12-Bit, 4-Channel Serial Output Sampling Analog-to-Digital Converter, 2001). The reference input to the ADC was bypassed using a 100nF capacitor. The decoupling also safeguarded the ADC performance under fast transient loading.

3.10. MCU and Peripheral Interfaces

The digitized measurement signals from the ADS7841 were processed by the STM32F334K8 mixed signal MCU running at 8 MHz. The MCU clock was sourced from a high-speed internal (HSI) RC oscillator, allowing for a simplified design with fairly accurate system and peripheral operation. The MCU also features an embedded floating-point unit (FPU) for supporting fast and reliable precision computations. Control and reading of the external ADC was achieved via the full-duplex 125 kbps SPI interface with the MCU set-up as master. The SPI communication was set up in MODE 0 (CPOL=0, CPHA=0) to support the digital interface of the ADS7841.

The waveguide network parameters were then computed from the four measured power magnitudes following Equations 16, 17 and 18. The parameters were displayed on a 16x2 character LCD, which was operated in 4-bit mode and controlled by the MCU via its standard 100 kHz inter-integrated circuit (I^2C) communication interface. The I^2C interface and the LCD's 16-pin parallel-port were connected via TI's PCF8574 8-bit I/O expander (Figure 13).

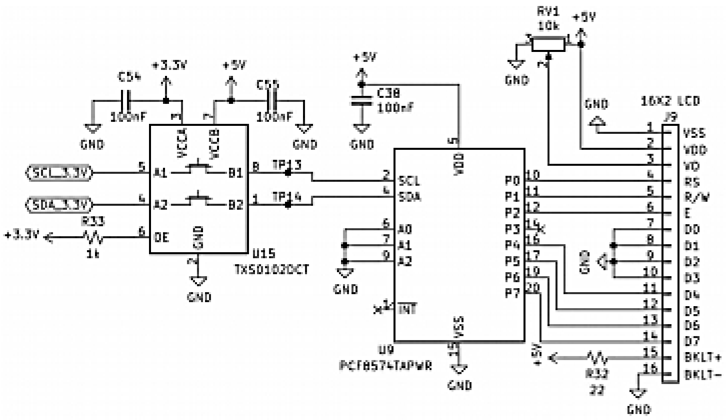

Fig. 13. The PCF8574 8-bit IO expander, TXS0102 translator and LCD interface

Like the SPI case, the serial clock (SCL) and serial data (SDA) I^2C lines were level shifted using the TI TXS0102 bidirectional auto direction-sensing translator. The dual-supply level translator, which employs a pass-gate architecture, has internal 10 kW pull-up resistors on its I/Os to adequately support the open drain drivers on the I/O pins of the MCU and PCF8574 (Remote 8-Bit I/O Expander for I2C Bus, 2015; Arm®Cortex®-M4 32b MCU+FPU, (STM32F334x4 STM32F334x6 STM32F334x8). Datasheet, 2020). Therefore, no external pull-up was required. TXS0102 also features an output one-shot edge-rate accelerator circuitry to handle fast rising signal in the I^2C communication and to improve the current drive capability of the I/O driver (2-Bit Bidirectional Voltage-Level Translator for Open-Drain and Push-Pull Applications, 2018). All address inputs A [0...2] of the PCF8574 were tied to ground, setting its address as 0×70. The +6 V powered actuator features an integrated self-configurable digital position controller composed of a factory-programmed Microchip PIC12F617 MCU and a ROHM BA6417F reversible motor driver. The actuator was controlled using a single 5V 1 kHz pulse-width modulation (PWM) signal whose duty cycle corresponded to the desired position expressed as a percentage of full stroke extension. The device also had built-in linear potentiometer which provided a feedback signal with a 0 - 3.3 V scaled amplitude proportional to the rod position with respect to the full stroke. Therefore, each of the two actuator interfaces had 4 pins: +6V, GND, PWM, and feedback. The PWM control signals were generated by STM32F334K8's high-resolution general-purpose timers and level-shifted to 0–5 V by the SN74HCT08 chip, to access the full stroke range of the actuator. 22 Ω resistors were placed on each PWM line post translation. This is very important to reduce dynamic switching currents. A typical CMOS gate (SN74HCT08) combined with PCB trace and (eventual) through-hole interface will create approximate 10 pF load (Practical Design Techniques for Sensor Signal Conditioning, 1999). In the absence of an isolation resistor, the SN74HCT08's 0.1 V/ns logic output slew rate produces about 100 μA dynamic current. Furthermore, all unused input pins are grounded as floating inputs could lead to slower input edge rates, which when coupled with noise generated on the power rails when the output switches, can cause excessive ringing and output errors (Implications of Slow or Floating CMOS Inputs, 2016). The actuator feedback signals were digitized by the MCU's built-in 12-bit ADC running at 2 MHz. The ADC has only one output data register serving all channels and it can digitize only one analog input at a time. The two signals could be digitized with single conversions interleaved with output register reading and ADC re-initialization (with a different analog channel). However, this wastes CPU resources and makes the tuner control error prone due to delays. An efficient solution was to scan the two channels. Here, a sequencer is employed at the ADC input to schedule the conversions and then link the output data register to the MCU's random access memory (RAM) using the direct access memory (DMA) controller.

The MCU was powered by a +3.3 V supply with 100 nF decoupling capacitor per VDD pin plus a 4.7 μF bulk capacitor. The analog reference (VDDA) of the MCU was also supplied separately with a +3.3 V rail but with additional filtering to eliminate high frequency crosstalk between the MCU's analog and digital domains. This is particularly important in this case because the MCU's HSI oscillator serves as the clock source for the whole front-end. For instance, phase noise on SCLK signal raises the distortion and noise floor thus degrading the ADS7841's signal-to-noise ratio. To prevent this, it is essential to keep the clock jitter comparable to the ADC's aperture jitter. The analog supply filter was formed from a series ferrite bead and the high Q 100 nF bypass capacitor (Figure 14).

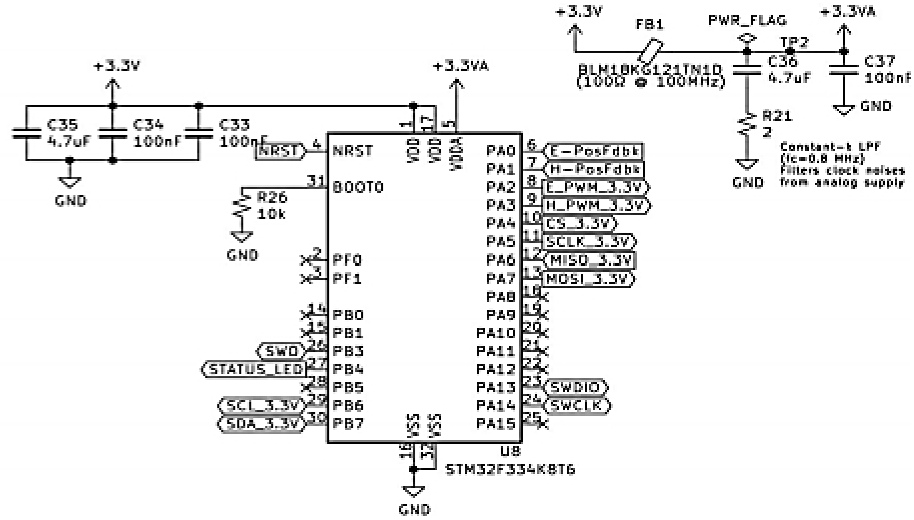

Fig. 14. The STM3232F334K8 MCU

The low-pass filter network was damped with a 2Ω resistor and 4.7μF series bulk capacitor to reduce possible resonance peaking without degrading the effectiveness of the bypass. Resonance peaking may occur since the resonant frequency of the undamped network is below the crossover frequency of the bead (~80 MHz) (BLM18KG121TN1D: Chip Ferrite Bead, 2020).

The MCU was then fitted with a 6-pin serial wire debug (SWD) interface for in-circuit programming and debugging via the ST-LINK probe. To prevent parasitic MCU resets, the NRST pin of the SWD interface was loaded with a 100nF debouncing capacitor. The BOOT0 pin was grounded through a 10 kΩ to allow activation of the bootloader during programming. A status light emitting diode (LED) was added for signaling.

3.11. Power Supply

The front-end was a mixed-voltage system that required +3.3 V, +5 V, and +6 V for the various on-board supplies as shown in Figure 15.

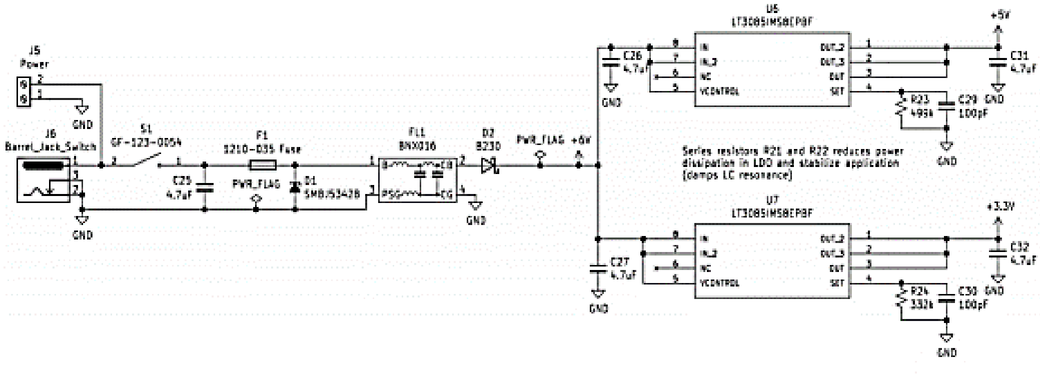

Fig. 15. Power Management Circuitry

Power was sourced from a +6V DC supply barrel jack or screw terminal and a SPST switch. The supply voltage is smoothed with a 4.7 μF capacitor to remove supply ripples. A resettable PPTC fuse (+6 V, hold = 0.3 A, trip = 0.7 A) and Zener diode (+6.8 V, 5W) were introduced for overcurrent and overvoltage protection respectively. The fuse rating allowed for the DC power circuit to support the actuators even under stalling conditions (maximum 0.46 mA stall current). For reliable attenuation of power line noises due to EM interference, a BNX016 EMI suppression filter was installed. A series Schottky barrier diode was then fitted for reverse polarity protection. Two Analog Devices' LT3085 adjustable 500 mA low dropout (LDO) linear regulators were employed to derive +5 V and +3.3 V supplies from the +6 V main line using single 499kΩ and 322kΩ voltage setting resistors, $\boldsymbol{R_{SET}}$ respectively. Ground-referenced 100pF capacitors were connected across $\boldsymbol{R_{SET}}$ to bypass the $\boldsymbol{R_{SET}}$'s shot noise and the LDO's reference current noise. 4.7μF low ESR capacitors were connected at the LT3085 inputs and outputs for decoupling and regulation stability.

4. RESULTS AND DISCUSSIONS

4.1. Prototype 1

A first working prototype of the network analyzer was built using off-the-shelf components for reflectometer's read-out circuit. The prototype, shown in Figure 16, had AD8318-based detector breakout circuit boards connected to the reflectometer's ports.

Fig. 16. First working prototype of the vector network analyzer

The analog DC outputs of each detector was fed to ADC inputs of STM32F429 evaluation board (based on the STM32F429ZIT6 MCU running at 180 MHz) and converted with the assistance of the DMA controller. The computed reflection coefficient was displayed graphically on the board's QVGA TFT LCD display. The analyzer prototype was calibrated based on the method in above and was tested. Although, it produces fairly accurate measurements, it was plagued with spurious errors which were attributed to the parasitic noise in the setup's poor cabling.

4.2. Prototype 2

Based on the fair results obtained from the first VNA prototype, a second was built for more accurate and stable measurements. The detector readout circuit as well as a closed-loop tuner control interface was designed and assembled on a printed circuit board (PCB).

4.3. PCB Design

The schematic of the front-end was captured and laid out using the KiCad EDA software. The PCB was designed with a 4-layer stack-up having separate planes dedicated to power, ground, and signals. The stack-up from top to bottom was: signal, ground, power, and signal. The stack-up was very important to proper performance of critical circuitry of the mixed-signal front-end. Placing the internal power and ground planes adjacent to each other provided additional inter-plane capacitance which improved high frequency decoupling of the power supply. The power plane is split to accommodate the three supply voltages whereas the ground plane is left uninterrupted. The large internal ground plane provided a low impedance return path for decoupling high frequency currents caused by fast digital logic but also minimizes EMI emissions. The ground plane also acted as a shield where sensitive signals cross. The board was sectioned into power, RF, analog, and digital areas with proper isolation practices to prevent the different signals from interfering with each other. Additionally, the RF frontend are adequately sectioned off vertically across all layers except the ground layer. Ground pours were made on top and bottom layers and connected to internal ground plane using multiple vias for improved thermal and electrical performances of the board. The power management circuitry was laid-out near the edges of the board to improve thermal performance of the LDOs. All power and ground pins of integrated circuits (ICs) were connected directly to the respective internal planes through vias and with short traces to avoid excessive loading. Decoupling capacitors were laid very close to the corresponding IC power pins and terminated through vias to the internal ground plane to preserve bypass effectiveness. 50Ω controlled impedance traces were used at the RF detector inputs to connect corresponding SMA connectors for good matching. Other essential signal routing, decoupling, and grounding techniques were observed to optimize PCB layout and maintain signal integrity. Test points have been placed on the signal and power lines for debugging and troubleshooting purposes. 3D renders of the designed board are shown in Figure 17.

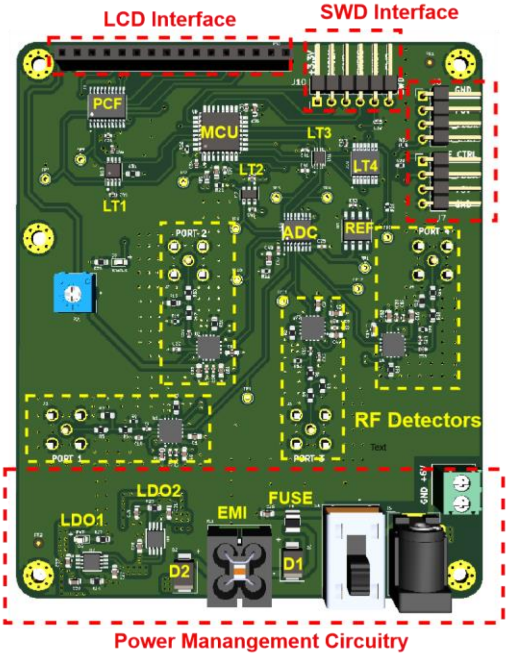

Fig. 17. VNA front-end

4.4. Calibration of proposed VNA

A simple two-point board-level calibration process was performed on each port to accurately obtain the transfer characteristics of the corresponding RF detector circuit at 2.45 GHz. This is because the slope and intercept $\boldsymbol{P_{INTERCEPT}}$ vary from one AD8318 device to another. Furthermore, since the exact attenuation produced by the realized fixed resistor pad is not easy to quantify, each attenuator and its associated AD8318 chip was calibrated together as a unit. The output voltage of the RF detector circuit in response to a power input $\boldsymbol{P_{IN}}$ can be expressed as

$$V_{OUT} = Slope \times (P_{IN} - P_{INTERCEPT}) \tag{21}$$

The calibration involved applying two known signal levels $\boldsymbol{P_{IN1}}$ and $\boldsymbol{P_{IN2}}$ to the detector circuit and measuring the corresponding output voltages $\boldsymbol{V_{OUT1}}$ and $\boldsymbol{V_{OUT2}}$. $\boldsymbol{P_{IN1}}$ and $\boldsymbol{P_{IN2}}$ were chosen from the linear-in-dB operating range of the AD8318 chip. The slope and intercept of the circuit transfer function were obtained from Equations ii and iii. ***Slope*** and $\boldsymbol{P_{INTERCEPT}}$ were stored in the device memory and are used in Equation iv to obtain the value of an unknown $\boldsymbol{P_{IN}}$ based on the measured $\boldsymbol{V_{OUT}}$.

$$Slope = \frac{V_{OUT1} - V_{OUT2}}{P_{IN1} - V_{IN2}} \tag{22}$$

$$P_{INTERCEPT} = P_{IN1} - \frac{V_{OUT1}}{Slope} \tag{23}$$

$$P_{IN(UNKNOWN)} = \frac{V_{OUT(MEASURED)}}{Slope} + P_{INTERCEPT} \tag{24}$$

RF signals with power levels -5 dBm and 5 dBm from an AtlanTecRF low power signal generator were used for the calibration process. The obtained transfer function parameters are shown in Table 1.

Tab. 1. Calibration results

	Port 1	**Port 2**	**Port 3**	**Port 4**
$Slope$	-25.77	-25.52	-26.08	-25.59
$P_{INTERCEPT}$ [dBm]	31.40	31.67	32.47	30.82

As indicated in Equation 18, the S parameters of the proposed VNA itself is required to accurately measure the reflection coefficient of a load it is connected to. The S parameters were measured using the Agilent E5071c VNA with the C2W transitions in a setup like what is seen in Figure 18.

Fig. 18. Test set up for measuring coupling level for ports

Here, the Thru-Reflect-Line (TRL) calibration method was used to shift the Agilent VNA's measurement reference plane from the (coax) feed points to the two waveguide ports of the reflectometer. This essentially eliminated the effect of the C2W transitions and ensured proper characterization of the device-under-test (proposed VNA), which is key to its performance, particularly $\angle\Gamma_L$ measurements. The measured device parameters at 2.45 GHz were $S_{11} = -0.05666 - j0.01006$ and$S_{21} = -0.6875 - j0.5152$. These values were also store in the device's memory.

4.5. Power Handling Capability

The proposed VNA was designed to be used for high power applications. The device is expected to be used in a network fed by a 6-kW generator. Inspection of simulated E-field patterns showed that the maximum field strength, Emax in the VNA is approximately

61 kV/m for 6 kW (Figure 19). For an empty WR340 waveguide section sourced with 6 kW, Emax= 70 kV/m, giving a reference power handling capacity of 4 MW, at which arcing occurs. Thus, with an Emax of 61 kW, the VNA can operate safely at high power without the risk of arcing.

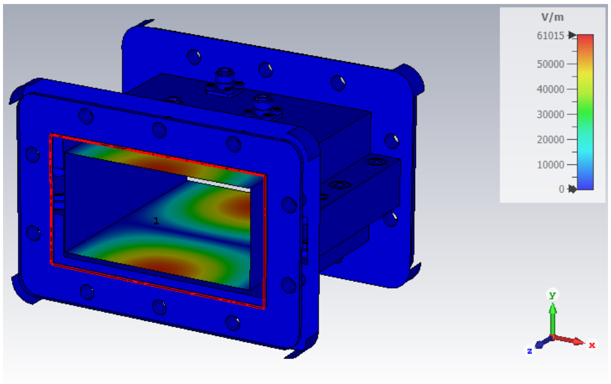

Fig. 19. Simulated E-field in the VNA when connected to a 6-kW generator running at 2.45 GHz

4.6. Evaluation

The performance of the proposed VNA was evaluated using the device to measure the reflection due to two different loads: a matched load and a terminated slide stub tuner. The experimental set-up comprised of the proposed VNA fed by a 13 dBm RF signal at 2.45 GHz with the loads connected on port 2. The experimental set-ups for measuring Γ_L of the matched and arbitrary loads using the developed VNA are shown in Figures 20 and 21 respectively. The reflection due to each of the two loads were also measured with the Agilent E5071c VNA and used as reference for comparison. The matched C2W transition presented a reflection coefficient with magnitude $|\Gamma_L|$=-23 dB and phase $\angle\Gamma_L$=145.3° when measured by the Agilent VNA (Figure 22) whereas the stub tuner load was configured such that it presented a $|\Gamma_L|$=-9.13 dB and $\angle\Gamma_L$=59.12° (Figure 23). Measurements using the proposed VNA produced $|\Gamma_L|$=-23.3 dB and $\angle\Gamma_L$=145.1° for the matched load whereas the recorded reflection due to the stub tuner load was $|\Gamma_L|$=-9.25 dB and $\angle\Gamma_L$=59.03°.

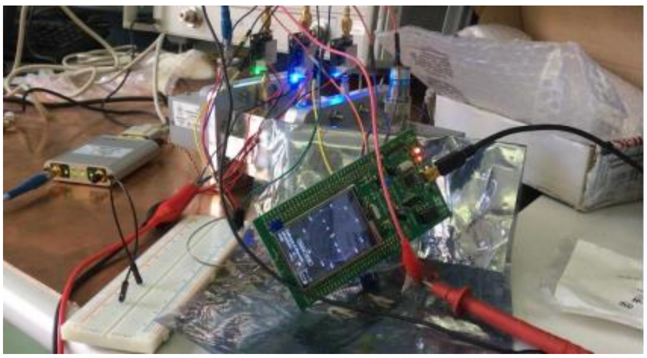

Fig. 20. VNA Evaluation Setup 1: Matched Load

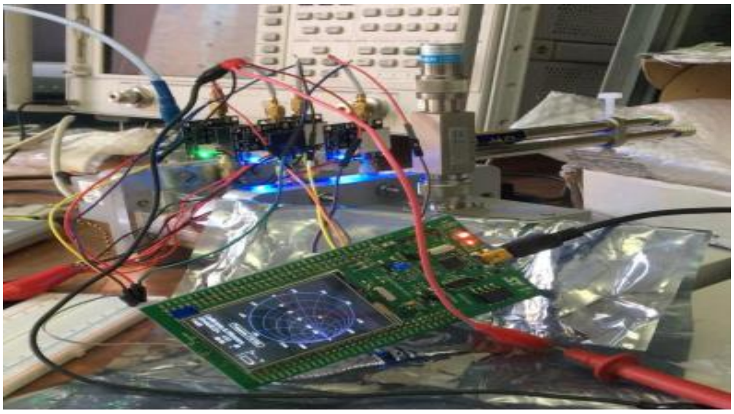

Fig. 21. VNA Evaluation Setup 2: Arbitrary Load

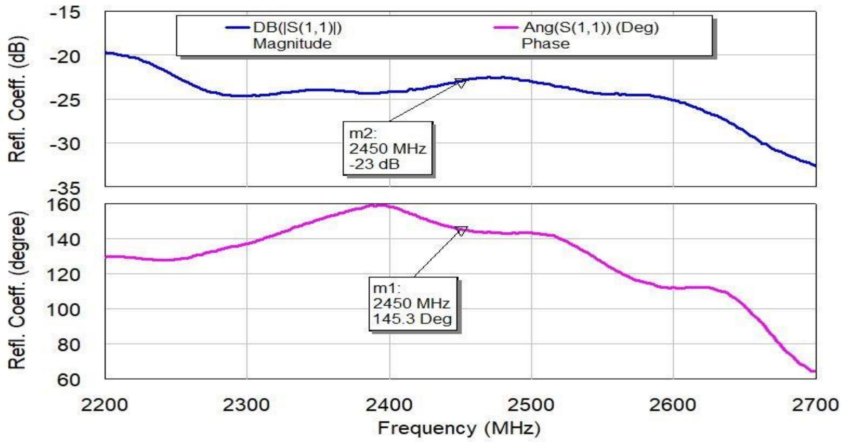

Fig. 22. Γ_L of the matched load measured the Agilent E5071c VNA

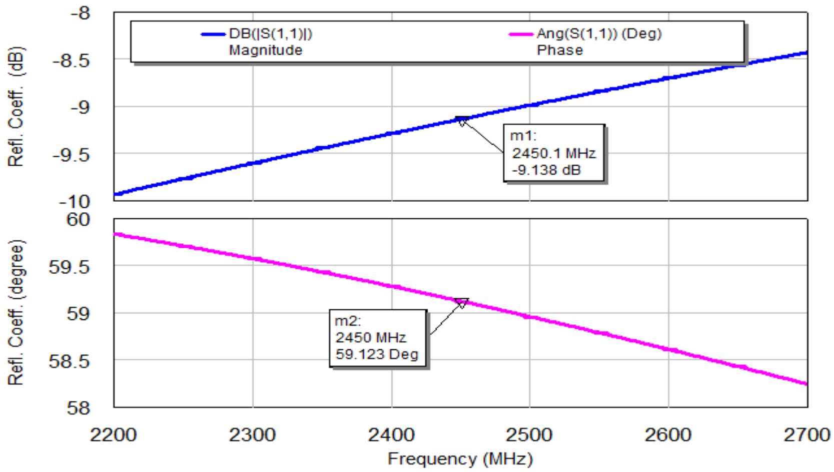

Fig. 23. Γ_L of the sliding tuner load measured the Agilent E5071c VNA

5. CONCLUSIONS

In this work, a compact vector network analyzer for high power microwave networks has been developed. The device was based on the six-port measurement technique where sampled powers from the network are used to derive the reflection coefficient at 2.45 GHz. The proposed analyzer is very useful in applications, which require online and inline parameter monitoring at multiple nodes in a microwave network, where employing commercial VNAs are not feasible in terms of cost, weight, safety, and complexity. Experimental results show a good and stable performance when compared to a commercial VNA, recording an average error of 0.21 dB and 0.15° error in complex reflection coefficient measurement.

Author Contributions

BK *– Idea, proposed design, and specifications and test and evaluation, read and approved final manuscript*

EOA *– Simulations and verification, read and approved final manuscript*

ETT *– Experimental set ups, tests, read and approved final manuscript*

ET – *Introduction, experimental strategies, read and approved final manuscript*

HNM *– Conclusion, experimental set ups, read and approved final manuscript*

BYA *– Related works, drawings, read and approved final manuscript*

Conflicts of Interest

The authors declare no conflict of interest.

REFERENCES

1 MHz to 8 GHz, 70 dB Logarithmic Detector/Controller. AD8318. (2019). *Analog Devices Inc.* http://static6.arrow.com/aropdfconversion/c131abb3e072c9996e733ced0e5cd0a20107716d/ad8318-ep.pdf

12-Bit, 4-Channel Serial Output Sampling Analog-to-Digital Converter. AD8318. (2001). *Texas Instruments Inc.* https://www.ti.com/lit/ds/sbas469c/sbas469c.pdf?ts=1663959751768&ref_url=https%253A%252F%252Fwww.google.com%252F

2-Bit Bidirectional Voltage-Level Translator for Open-Drain and Push-Pull Applications. TXS0102. (2018). *Texas Instruments Inc.* https://www.ti.com/lit/ds/symlink/txs0102-q1.pdf?ts=1663942071269&ref_url=https%253A%252F%252Fwww.google.it%252F

Amornraksa, S., & Sritangthung, T. (2020). Microwave-Assisted Pyrolysis of Fuel Oil for Hydrocarbons Upgrading. *E3S Web of Conferences*, *141*, 01013. https://doi.org/10.1051/e3sconf/202014101013

Arm®Cortex®-M4 32b MCU+FPU, (STM32F334x4 STM32F334x6 STM32F334x8). Datasheet. (2020). *STMicroelectronics.* https://datasheetspdf.com/datasheet/STM32F334R6.html

BLM18KG121TN1D: Chip Ferrite Bead. (2020). *Murata Electronics.* https://www.murata.com/englobal/api/pdfdownloadapi?cate=&partno=BLM18KG121TN1%23

Caiazzo, F., & Alfieri, V. (2018). Simulation of Laser Heating of Aluminium and Model Validation via Two-Color Pyrometer and Shape Assessment. *Materials, 11*(9), 1506. https://doi.org/10.3390/ma11091506

De-chao, H. (2015). The Application Advantages of Microwave Fixation in Cotton Fabric Dyeing. *International Conference on Education Technology, Management and Humanities Sciences* (pp. 535–539). Atlantis Press.

Elshemy, N. S. & Haggag, K. (2019). New Trend in Textile Coloration Using Microwave Irradiation. *J. Text. Color. Polym. Sci., 16*(1), 33–48.

Engen, G. F. (1977). The Six-Port Reflectometer: An Alternative Network Analyzer. *IEEE Transactions on Microwave Theory and Techniques*, *25*(12), 1075–1080. https://doi.org/10.1109/TMTT.1977.1129277

Gartshore, A., Kidd, M. & Joshi, L. T. (2021). Applications of Microwave Energy in Medicine. *Biosensors*, *11*(4), 96. https://doi.org/10.3390/bios11040096

Implications of Slow or Floating CMOS Inputs. SCBA004D. (2016). *Texas Instruments Inc.* https://www.ti.com/lit/an/scba004e/scba004e.pdf?ts=1663946172219&ref_url=https%253A%252F%252Fwww.google.com%252F

MacDonald, B., & Miadonye, A. (2018). Microwave Application in Petroleum Processing. *Ecology, Pollution And Environmental Science: Open Access (Eeo)*, *1*(1), 10–12.

Miniature Linear Motion Series L12. (2019). *Actuator Motion Devices Inc.* https://s3.amazonaws.com/actuonix/Actuonix+L12+Datasheet.pdf

Mohra, A. S. (2004). Six-Port Reflectometer Structure Using Two Microstrip Three-Section Couplers. *Scientific Bulletin, Ain Shams University, Faculty of Engineering*, *19*(1).

Moubarek, T., & Gharsallah, A. (2016). A Six-Port Reflectometer Calibration Using Wilkinson Power Divider. *American Journal of Engineering and Applied Sciences*, *9*(2), 274–280. https://doi.org/10.3844/ajeassp.2016.274.280

Moubarek, T., Almanee, M., & Gharsallah, A. (2019). A Calibrating Six-Port Compact Circuit using a New Technique Program. *International Journal of Advanced Computer Science and Applications*, *10*(5), 491–497.

Murzin, S. P., Kazanskiy, N. L., & Stiglbrunner, C. (2021). Analysis of the Advantages of Laser Processing of Aerospace Materials Using Diffractive Optics. *Metal*, *11*(6), 963. https://doi.org/10.3390/met11060963

Practical Design Techniques for Sensor Signal Conditioning. 1st Edition. (1999). *Analog Devices Inc.* https://www.analog.com/media/en/training-seminars/design-handbooks/Practical-Design-Techniques-Sensor-Signal/Outline.PDF

Remote 8-Bit I/O Expander for I^2C Bus. PCF8574. (2015). *Texas Instruments Inc.* https://www.ti.com/lit/ds/symlink/pcf8574.pdf

Shah, S. R. M. (2019). *Prospective Applications of Microwaves in Medicine*. M.S. thesis, Uppsala University, Uppsala, Sweden.

Sorică, E., Sorică, C. M., Cristea, M., & Grigore, I. A. (2021). Technologies used for food preservation using microwave. *E3S Web of Conferences*, *286*, 04008. https://doi.org/10.1051/e3sconf/202128604008

Ultraprecision, Low Noise, 2.048 V/ 2.500 V/ 3.00 V/ 5.00 V XFET ® Voltage References. ADR420/ ADR421/ ADR423/ ADR425. (2013). *Analog Devices Inc.* https://www.farnell.com/datasheets/101790.pdf

Vishnuram, P., Ramachandiran, G., Sudhakar, B. T., & Nastasi, B. (2021). Induction Heating in Domestic Cooking and Industrial Melting Applications: A Systematic Review on Modelling, Converter Topologies and Control Schemes. *Energies*, *14*(20), 6634. https://doi.org/10.3390/en14206634